Metal Nanodendrites and Their Applications as 3D Surface Enhanced Scattering (SERS) Substrates

By

Aseem Athavale

DISSERTATION

Submitted in Partial Fulfillment of the Materials Science and Engineering for the Degree of Doctor of Philosophy at The University of Texas at Arlington.

May 2021

Arlington, Texas

Supervising Committee

Dr. Yaowu Hao, Supervising Professor

Dr. Efsthathios 'Staths'I Meletis

Dr. Choong-Un Kim

Dr. Ye Cao

Dr. Weidong Zhou

Dr. Digant Dave

UNIVERSITY OF
TEXAS
ARLINGTON

Acknowledgements

The number of people and the amount of support I have received from them is way beyond the confines of a small page worth of acknowledgements. I want to thank each and every one of them for the constant and unconditional support.

Firstly, I'd like to thank my supervising professor Dr. Yaowu Hao whose guidance and expertise guided me all the way and made this possible for me. I would also like to thank the committee Dr. Kim, Dr. Meletis, Dr. Zhou, Dr. Cao, and Dr. Dave for their guidance and insights.

Special thanks to my group members Yu-Jen Chiu (Aaron), Shahab Ranjbhadori and Christopher Pickering whose constant support and witty conversations over lunch and unlimited numbers of coffee breaks kept me going and helped me get through all of it with a smile. Their insights and knowledge helped me at a lot of technical crossroads regrading my research and education. Thanks for being friends and group members at the same time.

The constant support and encouragement of every possible kind is what kept me sane and I'd like to thank the people who believed in me and stood by me in the best and most importantly the worst of the times. Thank you, Apra Chikara, Pranav Masariya, Ameya Dixit, Karan Chaudhary, Anadi Jere, Amogh taraikar, you guys are the best.

The special *thank you* is to her who stood there by my side, emotionally uplifting me and whose unconditional love and support encouraged me to keep going, my girlfriend and soon to-be wife Priya Teredesai.

Most importantly, my most sincere gratitude towards the people without whom I wouldn't exist-*literally*, my parents and my sister. Thank you and am forever grateful for the unlimited support and love and care. This is for you 'Aai' 'Baba' and Ananya.

Abstract

Metal Nanodendrites and Their Applications as 3D Surface Enhanced Scattering (SERS) Substrates

Aseem Athavale

The University of Texas at Arlington

Supervising Professor: Dr. Yaowu Hao

Ultrasensitive detection of chemicals and biological analytes has been a focus of a lot of studies in the recent years. In this search for the versatile detection technique, Surface Enhanced Raman Spectroscopy (SERS) has proved to be one powerful method. SERS is a powerful vibrational spectroscopy technique that allows for label free ultrasensitive detection. This method utilizes the Localized Surface Plasmon resonance (LSPR) effect of nanoparticles. LSPR effect is profound in noble metals such as silver (Ag) and gold (Au). We have developed a novel SERS substrate using Ag dendrites that can be applied as a ready-to-use device in a variety of applications.

The substrate was fabricated via self-deposition of silver nanodendrites on copper wires of 80 microns inside different channels of glass or silver coated PDMS. The deposition was done by the galvanic replacement reaction between silver nitrate and copper. This reaction was previously thought as the simple high-school chemistry reaction, i.e. formation of Ag dendrites can be explained by a simple reaction mechanism as follows :. a reduction reaction, $Ag^+ + e^- \rightarrow Ag$, takes place only on a metal surface, first on Cu and then on newly formed Ag. The electron comes from the oxidation reaction $Cu \rightarrow Cu^{2+} + 2e^-$, which takes place at Cu surface, where Cu^{2+} is released into the solution, and electron transport inside the metal-to-metal surface to reduce Ag^+. The reduction rate is higher on the Ag (1 1 1) surface, leading to preferential growth in the [1 1 1] direction. However, a series of experiments revealed that this reaction mechanism is much more complex than a simple two step galvanic replacement reaction: metal Ag could

form through reduction of Ag^+ by intermediate nitrite (NO_2^-) ions inside the solution on a surface away from Cu. It was also found that Ag dendrites developed through a particle-mediated growth process. This new reaction mechanism can be utilized to generate completely freestanding, pure, and clean single-crystal Ag dendrites at room temperature within a few minutes.

After a series of studies on morphology and reaction conditions, we developed a robust 3-D SERS substrate using Ag dendrites, which has extremely high sensitivity and excellent reproducibility. More importantly, such device can detect molecules in-liquid without sampling and drying. The sensitivity of the substrate was verified with rhodamine 6G (R6G) with the lowest concentration of about 1×10^{-14} M. We also experimented with other common SERS molecules like Methylene Blue and 4-Methoxybenzoic Acid and were able to detect them as well at very low concentration.

For better understanding of the mechanism behind such high sensitivity, we conducted FDTD simulations on representative 2D/3D models of dendrites according to the SEM images. These simulations revealed a high electric field enhancement of $10^6 – 10^7$ from narrow gaps between branches in the dendrite structure.

Aiming for practical application of the device, we developed a method of calibrating these devices using low concentrations of R6G. After calibration, we were able to reliably detect low concentrations of around 0.5 ppm of Thiabendazole(TBZ), which is a commonly used pesticide has been labelled as a potential carcinogen. These 3-D SERS substrates were proved as a precise and fast in-situ Raman detection method for flowing liquid media.

1 Table of Contents

2 Introduction

Recently, molecular detection has attracted great interest in the biological, clinical, chemical, and environment fields [1, 2]. Raman spectroscopy is one of the most applicable analytical tools for identification and characterization of molecules, but in the case of a dilute solutions, the Raman signal is very weak, which limits its applications [3, 4]. It has been found that Raman signal can be greatly enhanced when analyte molecules reside on a nanostructured metal surface. This phenomenon is termed as Surface Enhanced Raman Scattering (SERS). SERS is a powerful technique which can detect Raman signals from very diluted solution. [5]. Two mechanisms have been proposed to explain SERS (1) chemical enhancement which relies on charge transfer processes between analyte molecules and nanostructured metal surface and (2) amplification of electromagnetic field near the analyte molecules due to the excitation of localized surface plasmons (LSPs) of nanostructured metals [6-9]. The detailed information about Raman scattering and SERS is described in Chapter 2.

To obtain high-performing SERS substrates, various metallic nanostructures have been explored. It has been verified that SERS enhancement is highly related to the morphology of the substrate since the microstructure variation can change the electromagnetic field [14]. It has been found that the gaps and slits (called hot spots) in these nanostructures can greatly enhance the local electromagnetic field. Also, their large surface area allows improved adsorption of analyte molecules [10-12]. Compared to other metals, silver nanostructures with super-hydrophobic surface and narrow plasmon resonance have been widely investigated for SERS applications [13]. Lots of experiments have been done to fabricate Ag nanoparticles with different morphologies such as wires [15, 16], rods [17, 18], triangular plates [19], cubes [20-22], polyhedrons [23], dendrites [24, 25]. Among them, Ag dendrites contain many multi-level branching nanostructures, and consequently, create a large specific surface area which is more appropriate for absorption of analyte molecules [26, 27]. Also, the resultant nanostructure includes a large number of hot spots which would exist in the spaces at the end of branches or among adjacent branches. Therefore, Ag dendritic nanostructure has been considered as an exceptional SERS substrate [28-30]. To date, various techniques have been employed to fabricate Ag dendrites, including electrochemical deposition [31-34], template synthesis[35-37], ultraviolet irradiation photoreduction [38], ultrasonic-assisted reduction [39], solvothermal or hydrothermal synthesis[40], γ-irradiation route [41], pulsed sono-electrochemical [42], and galvanic replacement reaction (GRR) [43, 44]. Of these synthetic routes, GRR is one of the most attractive approaches to fabricate the fractal structure due to its simplicity and versatility. Through GRR, metal ions in the solution are reduced by the oxidation of a more reactive (sacrificial) metal . The driving force for GRR is the electrochemical potential difference between two metals [45]. That is, one metal (known as a sacrificial metal) is oxidized and would go through oxidization, while the ions of another metal are reduced and stick to sacrificial metal. Several metals like Sn [46], Fe [47], Zn [48, 49], Al [50, 51], Ni [52, 53], and Mg [54], were used as the sacrificial one to produce Ag dendrite structures. However, Cu has been used more than the other due to the higher standard reduction potential, making the process faster and without producing solid oxide [13]. Also, Cu is considered a good plasmonic material and has LSPR wavelengths similar to Au and Ag which lie in the near-infra red and visible region, where the most Raman measurements occur. According to previous experiments [55-65], creation of Ag dendrites on the copper surface is done through a simple conventional reaction,

$$Cu_{(s)} + 2Ag^{+}_{(aq)} \rightarrow 2Ag_{(s)} + Cu^{2+}_{(aq)} \qquad \text{Eq. (1)}$$

but the detail study of this process by us has had intriguing results and the reaction mechanism might not be as simple as previously thought [66]. It was observed that when a barrier is introduced between silver nitrate and copper, the dendrites can form on the other side of the barrier without any direct metallic contact between Cu and Ag dendrites, suggesting that there was a presence of some intermediate ionic species that facilitated the reduction reaction. The ionic species that are possible in this solution are Ag^+, NO_3^- (nitrate), Cu^{2+} (cupric), NO_2^- (nitrite), and Cu^+(cuprous). Among them, $NO_2^-$and Cu^+ are the only possible intermediate ions. The concentration of Cu^+ ions would be extremely low, since Cu^+ is not stable in aqueous solution. Therefore, the intermediate ion that assists to reduce Ag^+ into metal Ag must be NO_2^-. It is known that Cu can reduce $NO_3^-$to NO_2^- through the reaction shown in Eq. (2) Ag^+ ions could

$$Cu_{(s)} + NO_{3\,(aq)}^- + 2\,H_{(aq)}^+ \rightarrow Cu_{(aq)}^{2+}\; NO_{2\,(aq)}^- +\; H_2O_{(l)} \qquad \text{Eq. (2)}$$

$$Ag_{(aq)}^+ +\; 2\,NO_{2\,(aq)}^- +\; 2\,H_2O \;\rightarrow\; Ag_{(s)} +\; 2\,NO_{3\,(aq)}^- +\; 4\,H^+ \qquad \text{Eq. (3)}$$

subsequently be reduced by the resultant nitrite ions via the reaction in Eq. (3) which results in Ag dendrite formation and growth. The detailed experimental procedure and findings on this new reaction mechanism are described in Chapter 4.

Aiming to develop a SERS device for in liquid detection of analyte in flowing media, we synthesized Ag dendrite substrates inside transparent glass capillaries of square cross-section with small ID of 0.5 mm. The synthesized nano-dendrites inside the capillaries had the average dimensions of 3-5 microns main branches with secondary branches of 500 nm – 1 µm length. The average diameters of the branches were close to 100 nm and the gaps between these branches varied from 10 - 25 nm. The device was first tested with Rhodamine 6G (R6G). The detection of extremely low concentration of 10^{-14} M has been achieved. Other organic molecules including Methylene Blue and 4 Methoxy benzoic acid were also be used to test the device. To demonstrate a practical application of such device, we measured and analyzed low concentrations of 0.001 g/L of Acetaminophen, a commonly used drug, in flowing liquid media.

For better understanding of the enhancements of SERS signals generated with these substrates Finite Difference Time Domain (FDTD) simulations were studied, which showed excellent enhancement factors in the range of 6-7 orders of magnitude, depending on the different structures that were observed from

SEM micrographs and reconstructed as 2D/3D models in CAD for simulation. A detailed account of all the studies, fabrication, SERS results and FDTD simulation observations are presented in detail in Chapter 5.

Main focus of this study was to develop a practical SERS analyzer for real-world applications, lots of research has been dedicated to this for more than a decade now. Here, we were able to transfer the advances in our four walled glass capillary substrates to a powerful device with PDMS channels of the same dimensions. The main drawback of the glass capillary substrate is that only destructive imaging is possible which limits the possibility of evaluating the substrate properties before the measurement. A device using Ag coated three-walled PDMS channels covered with a removable glass coverslip was fabricated. The dendrites synthesized inside the channels can be observed under SEM after removing the coverslip. The SERS performance of the device was tested and was at par with our glass capillary substrates. We also explored the calibration of these devices using low concentration of R6G as the calibrating molecules, this aids in locating hot spots as well as can be used as a final quality check for the device before practical application. The details of this device and excellent practical applicability of the device has be presented in chapter 6.

To demonstrate a practical application, we applied these devices for detection of Thiabendazole(TBZ), which is a systemic fungicide that belongs to the benzimidazole compounds. Although TBZ is classified as low toxicity to humans, it is very toxic to aquatic environment. According to the United States Environmental Protection Agency (USEPA) [230], TBZ is the most found pesticide in apple in United States and the Maximum Residue Level (MRL) tolerated is 5 ppm[231]. We were able to detect TBZ inside R6G-calibrated devices and achieve a detection limit of 0.5 ppm which is one order of magnitude lower than the tolerated MRL. These results are also included in the Chapter 6.

3 Background Information

3.1 Raman Scattering

When an EM radiation is incident on a material, the incident photons excite the sample, this causes polarization of electrons. This excitation of electrons (or electron cloud) creates an induced dipole moment (P). Such integration puts the molecule in a virtual energy state for a short time before the photon is emitted, major portion of this scattered light has the exact frequency as incident light frequency (ν_0), which is known as elastic scattering or Rayleigh scattering. However, very small portion of scattered light having different frequency than incident light is referred as inelastic scattering or Raman scattering. After the scattering event, the sample is in a different rotational or vibrational state (rovibronic state). Raman scattering is mainly dependent on the vibrational modes of molecules and should not be confused with emission. Therefore, the Raman spectrum (scattering intensity as a function of the frequency shifts) depends on the rovibronic states of the molecule.

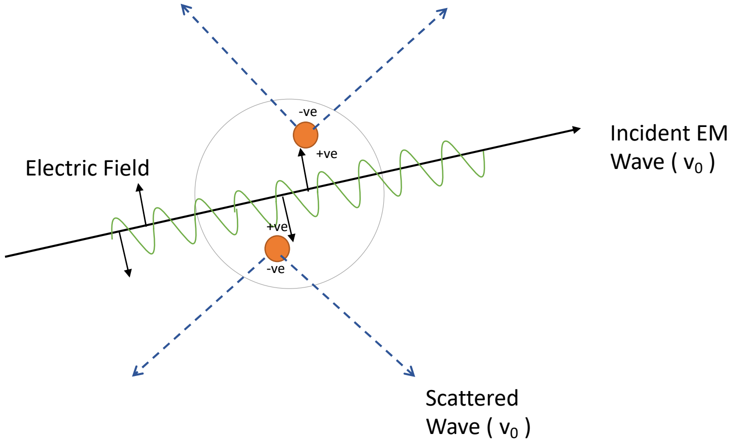

Figure 1 : Theoretical representation of Raman Phenomenon

Strength of induced dipole moment (P) is proportional to electric field, and the proportionality is called polarizability, as given by

$P = \alpha E$ Eq. (4)

where α is the polarizability and E is the strength of electric field of the incident EM wave. Molecular structure and nature of bonds determine the polarizability of a material. Time dependent electric field of the incident EM wave, may be expressed as

$E = E_0 \cos (2\pi v_0 \, t)$ Eq. (5)

where v_0 is the frequency (Hz) of the incident EM ($v = \frac{c}{\lambda}$). Substituting Eqn. (5) into (4) yields the time-dependent induced dipole moment,

$P = \alpha E_0 \cos(2\pi v_0 t)$ Eq. (6)

As the ability to perturb electron cloud is dependent on the position of atoms, polarizability becomes function of the position. Vibrational energies are quantized in the similar manner as electronic energies. The vibrational energy of any particular mode can be represented by,

$E_0 = (j + \frac{1}{2}) \, \mathrm{h} v_{vib}$ Eq. (7)

where j is the vibrational quantum number (j = 0,1,2 ...), v_{vib} is the frequency of the vibrational mode, and h is the Planck constant. The particular vibrational mode displacement dQ of the atoms about their equilibrium position can be expressed as

$dQ = Q_0 \cos(2\pi v_{vib} t)$ Eq. (8)

where Q_0 is the maximum displacement about the equilibrium position. Taylor series expansion can be considered for smaller displacements, and its second and more order differentiation term can be ignored.

$\alpha = \alpha_0 + \frac{\partial \alpha}{\partial Q} dQ$ Eq. (9)

where α_0 is the polarizability of the molecular mode at equilibrium position. Substituting Eq. 8 in Eq. 9 yields following Eq. 10.

$$\alpha = \alpha 0 + \frac{\partial \alpha}{\partial Q} Q_0 \cos(2\pi v_{vib} t) \qquad \text{Eq. (10)}$$

Finally, Eq. (7) may be substituted into Eq. (3), which yields

$$P = \alpha_0 E_0 \cos(2\pi v_0 t) + \frac{\partial \alpha}{\partial Q} Q_0 E_0 \cos(2\pi v_0 t) \cos(2\pi v_{vib} t) \qquad \text{Eq. (11)}$$

By using a trigonometric identity, above equation can be rewritten as,

$$P = \alpha_0 E_0 \cos(2\pi v_0 t) + \frac{\partial \alpha}{\partial Q} \frac{Q_0 E_0}{2} \{ \cos(2\pi(v_0 - v_{vib})t) + \cos(2\pi(v_0 + v_{vib})t) \} \qquad \text{Eq. (12)}$$

The above equation suggests that induced dipole moments are created at three different frequencies, namely v_0, $(v_0 - v_{vib})$, and $(v_0 + v_{vib})$, which in produces scattered radiation at these same three frequencies. The first scattered frequency represents elastic scattering as it has same frequency as incident light. However, the latter two frequencies are considered to be inelastic because of their shifts. These latter two cases are considered as Raman scattering, with the down-shifted frequency known as Stokes scattering, and the up-shifted frequency known as anti-Stokes scattering.

It should be noted from the final equation that the necessary condition for Raman scattering, the term $\frac{\partial \alpha}{\partial Q}$ must be non-zero. Physical interpretation of this term suggests that the vibrational displacement of atoms corresponding to a vibrational mode causes change in the polarizability. Let's consider a diatomic molecule A-B, with maximum vibrational displacement Q_0, as shown below

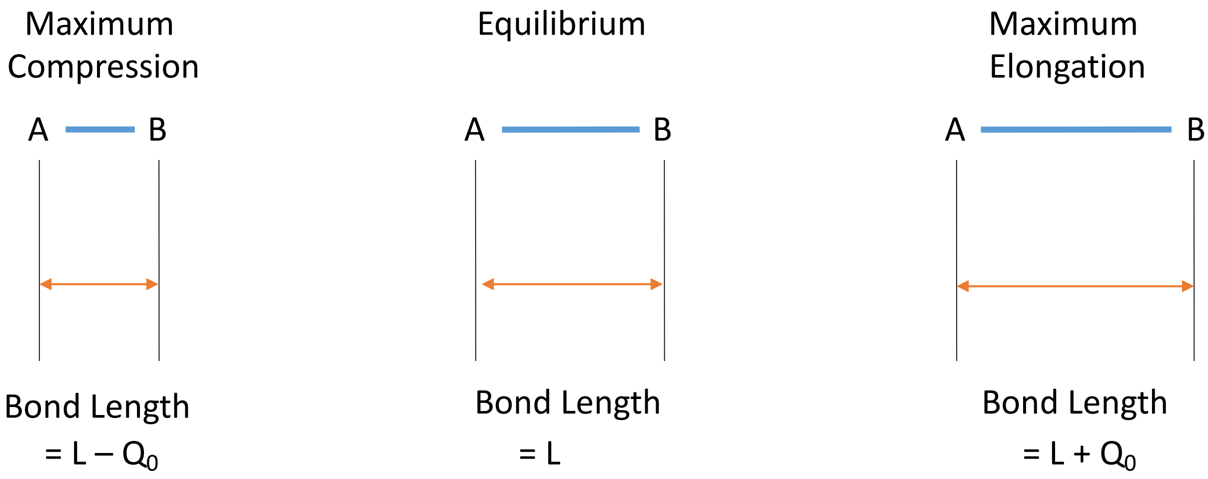

Figure 2 : Vibrational displacement of A-B about the equilibrium position

From Fig. 2, it can be considered that when A-B are in maximum compression, their electrons will have attraction from nucleus of other atom and hence it will be very difficult to perturb electrons in this situation. Here polarizability will be minimum. On the contrary when atoms A-B are at maximum distance apart, electrons can be easily perturbed in this situation. Hence polarizability will be highest in this situation. However, one should note here that polarizability is continuously changing with respect to displacement, and we can draw a plot for it which looks as below.

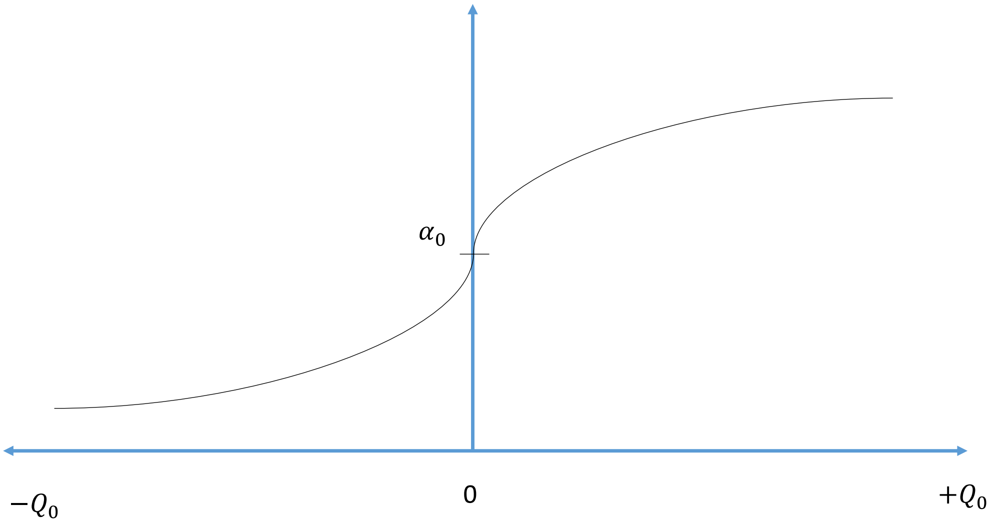

Figure 3 : Polarizability of A-B as a function of vibrational displacement about equilibrium

In above plot $\frac{\partial\alpha}{\partial Q}$ is non-zero though out the range and full-fill the Raman condition. Hence it should produce Raman scattering at the two frequencies $(v_0 - v_{vib})$ and $(v_0 + v_{vib})$.

3.2 Surface Enhanced Raman Scattering (SERS)

3.2.1 Introduction

It's been almost 40 years since the discovery of the SERS effect and with studies developed and attention to detail to the effects and applicability of SERS, it has been established that SERS can be employed to achieve enhancements of up to 14 orders of magnitude under favorable circumstances. There has been a surge in focus directed towards understanding the mechanisms and widening of the benefits of this method to tackle ultrasensitive detection of chemicals as well as biological species with precision.

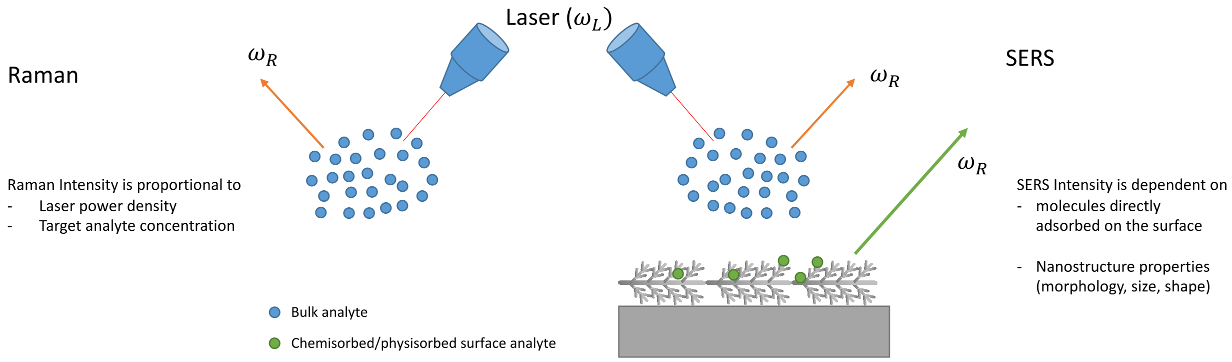

Figure 4 : Schematic Comparison between Raman and SERS

The observation and discovery of SERS can be credited to *Fleischman* et al. [67] in 1947, *Jeanmarie* and *Van Duyne* [68] and *Albrecht* and *Creighton* [69] in 1977. It was proposed that the huge increase in Raman cross-section was a result of surface plasmons [70], which led to a number of predictions such as the expectation that SERS should be observable in metal colloids and the hierarchy of intensification that should be observed, all else being the same, with silver and the alkali metals providing the most intense SERS signal followed by gold and copper in that order, then the other good conductors and finally the transition metals and other poorly conducting metals [70].

Enhanced Raman intensities achieved through SERS have been used to study and detect very low concentrations of molecules on nano-rough surfaces and nanoparticles. With developments in nano-fabrication techniques and nanoparticle synthesis, these enigmatic effects of SERS have been employed towards single molecule detection as well. *Kneipp* and coworkers [71,72,73,74,74,76] and *Nie* and coworkers [77,78,79,80] who's independent work reported that high enough SERS intensities can be, under favorable circumstances, recorded that could detect single molecules.

The mechanisms leading to SERS have been studied by a lot of groups in detail and mainly two models have been attributed to causing these effects, namely, Electromagnetic mechanism and Chemical mechanism.

3.2.2 Electromagnetic mechanisms of SERS

Scaling of Raman intensities can be explained by the electromagnetic mechanism, as it involves enhancement in the field intensity as a result of plasmon resonance excitation. The well-known electromagnetic enhancement mechanism can be applied to study this where the enhancement factor E at each molecule is approximately given by

$$E = |\mathrm{E}(\omega)|^2\, |\mathrm{E}(\omega')|^2 \qquad \text{Eq. (13)}$$

Where $\mathrm{E}(\omega)$ is the local electric-field enhancement factor at the incident frequency ω and $\mathrm{E}(\omega')$ is the corresponding factor at the stokes-shifted frequency ω'. E is often approximated by assuming $\mathrm{E}(\omega)$ and $\mathrm{E}(\omega')$ are the same, and hence $E = |\mathrm{E}(\omega)|^4$

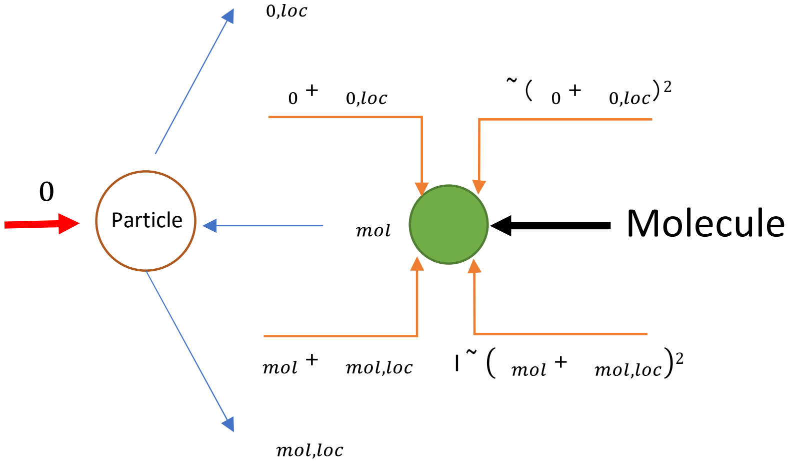

Figure 5 : Electromagnetic Mechanism of SERS

A number of theoretical estimates of SERS enhancement factors have been made in the last decade for non-resonant molecules on nanoparticle surfaces using computational electrodynamics methods such as discrete dipole approximation (DDA) [81] and the finite difference time-domain (FDTD) [82] to solve Maxwell's equations to determine the local fields $\mathrm{E}\ (\omega)$. We used the FDTD method for calculating the enhancement factor for our substrate which is discussed later.

3.2.2.1 Contributions to Electromagnetic Enhancement

Let us suppose a particle that is placed on a metallic substrate that supports the excitation of surface plasmons when illuminated with laser light, in this case the electromagnetic enhancement can be attributed to two distinct contributions.

The Local field (Near Field Enhancement) Enhancement: The strong spatial localization and as a result the amplification of the laser light in small spatial regions induced by the excitation of the surface plasmons, generally termed as hot spots, makes the electromagnetic field

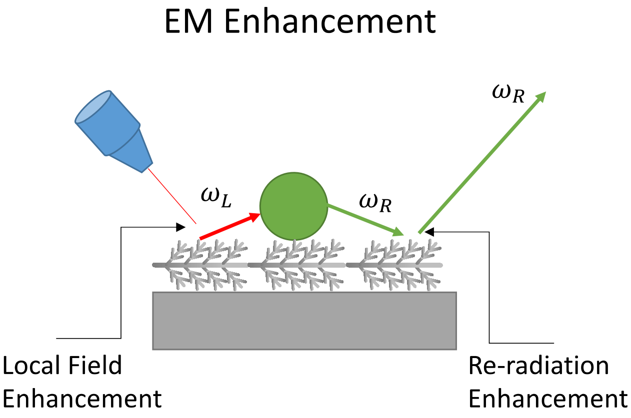

Figure 6 : Contributions to EM enhancement

experienced by the molecules in the close vicinity of the hot spots very strong. And from the classical understanding of Raman, the radiated power P_{raman} is proportional to the square modulus of the dipole [83] given by the following equation,

$$P_{raman} = \frac{\omega_R^4}{12\pi\varepsilon_0 c^2} |p(\omega_R)|^2 = \frac{\omega_R^4}{12\pi\varepsilon_0 c^2} |\hat{\alpha}_R(\omega_R, \omega_L)\, E(\omega_L)|^2 \qquad \text{Eq. (14)}$$

From the equation $p(\omega_R) = \hat{\alpha}_R(\omega_R, \omega_L)\, E(\omega_L)$, the Raman polarizability tensor of the molecule. [84] ε_0 is the dielectric constant in vacuum and c is the speed of light in vacuum. In this case, P_{Raman} is derived from the classical physics and is expressed in [W] rather than in [photons/s] (the two quantities are related by the expression P_{Raman} *[W] = ħω* P_{Raman} *[photons/s]);* the angular frequency ω is expressed in [radians/s] and is related to the wavenumber, normally used in vibrational spectroscopy, by the relation: *ω = 2πcev*. The presence of a metallic substrate nearby the molecule can be accounted for by considering that the molecule experiences a local electric field *($E_{Loc}(\omega_L)$)which is* stronger than the input one; Equation clearly suggests that the higher the electric field, the higher the radiated power.

The Re-radiation Enhancement : The presence of the metallic structure nearby the molecule modifies also the efficiency with which the molecule radiates Raman power; this occurs because the power radiated by a dipole (i.e., the molecule oscillating at the Raman frequency) depends on the environment in which it is embedded. The radiation characteristics of an oscillating dipole are significantly affected by the dielectric properties of its surroundings and their consequential optical resonances processes. Similarly, the Raman-scattered fields are themselves enhanced in a subsequent process of radiation enhancement, such that the over- all SERS enhancement is approximately the product of the incident and Raman enhancement processes.

Hot-Spots : Regions of intense local field enhancement caused by Local Surface Plasmon resonance (LSPR) effect, are termed as Hotspots. The highly localized regions are most evidently observed in interstitial crevices present between nanostructures, or between two separate nanostructures, provide extraordinary enhancements of up to 10^{14} order of magnitude to the surface enhanced Raman Scattering (SERS) signal. This is proportional to the $|E|^4$ in areas of sub wavelength localization. Molecules resident in SERS hotspots (1–5 nm) often dominate the measured SERS spectrum

3.2.3 Chemical Enhancement

This second multiplicative contribution to the SERS enhancement relies on the modification of the Raman polarizability tensor of those molecules chemically adsorbed onto the nanostructure as a consequence of the formation of new analyte–metal surface complexes. The resulting alteration of the electronic properties of the adsorbed analyte may allow new electronic transitions within the surface complex analogous to those observed for Resonant Raman scattering which, in a similar manner, determine an increase of the Raman cross-section (in particular for those vibrations involved in the electronic transitions). Therefore, the CE is not related to the SERS process itself but to the modification of the adsorbate polarizability [84]. However, CE, when present, usually contributes to the overall

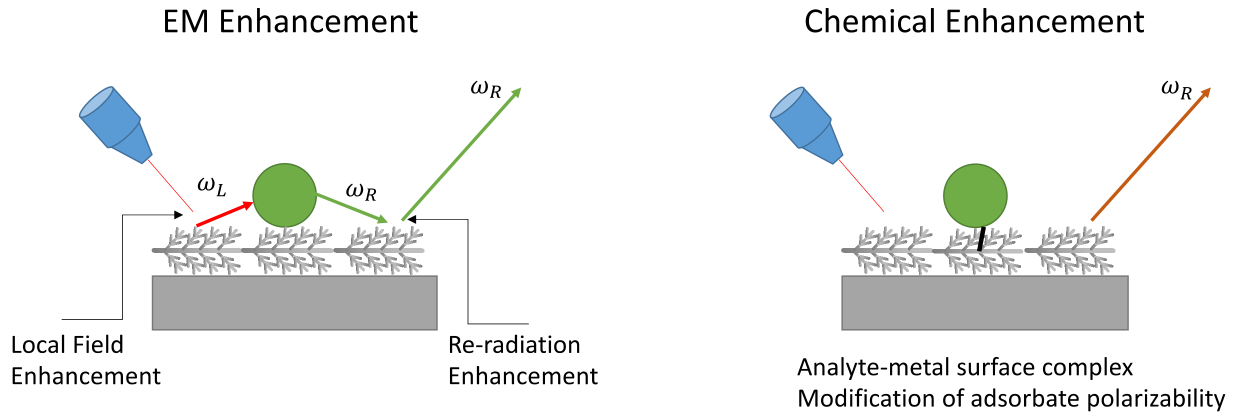

Figure 7 : Schematic representation of EM enhancement and Chemical Enhancement

enhancement to a much lesser extent (usually by 1–2 orders of magnitude) and, contrary to EM, is analyte-dependent [85].

3.3 Finite Difference Time Domain (FDTD)

3.3.1 Introduction

As discussed above it has been observed that the main mechanisms responsible for the SERS effect are EM and Chemical. Though there is still debate in the literature about the mechanism of SERS, it has been established that the chemical mechanism requires a chemical and/or EM interaction from some probes with different intrinsic properties, however the EM enhancement would be possible even in the absence of such probe. Thus, the EM enhancement plays a bigger role, if all the other parameters are maintained the same. In order to study and determine the EM fields in enhanced spectroscopy and understand more quantitatively and qualitatively the link between EM enhancement and the underlying localized surface plasmon resonance, analytical and numerical tools have been applied to solve EM problems. With recent advances in computing techniques and exponential increase in processing power many methods and numerical techniques have been proposed and explored for such calculations, such as Finite Element Method (FEM) [86], Finite Difference Time Domain (FDTD) [87], Discrete Dipole Approximation (DDA) [88]etc.

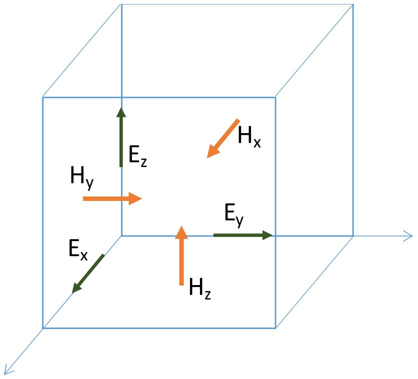

Figure 8 : Yee Cell

From these techniques FDTD is most commonly used. The FDTD method has been widely used to solve Maxwell's equations in complex geometries in the fields of EM and photonics, and it contributes to the simulation of light scattering from metal particles. Another important factor contributing towards the usage of FDTD as the technique for SERS simulations is that it solves the equations in time domain, this means that the calculation of the electromagnetic field values progresses at discrete steps in time. In the FDTD approach, both space and time are divided into discrete segments. Space is segmented into box-shaped cells, which are small compared to the wavelength. The electric fields are located on the edges of the box and the magnetic fields are positioned on the faces as shown in Fig. 8. This orientation of the fields is known as the Yee cell [89] and is the basis for FDTD. Time is quantized into small steps where each step represents the time required for the field to travel from one cell to the next.

Many such FDTD cells are combined together and the FDTD grid or mesh is constructed. The dimensions of these cells are very important in FDTD simulations. The edges and faces of each cell overlap with its neighbors and as a result each cell will have three electric fields that begin at a common node and three magnetic fields originating on the faces adjacent to the node.

3.3.2 Simulation Steps

The important steps in FDTD simulation and parameters that need to be considered are as follows:

- Defining Physical Structures: It is known that the LSPR effect depends predominantly on the morphology and dimensions of the metallic substrate, the SERS EM enhancement will also depend on it; thus, it is very important to define the correct physical nanostructure for FDTD simulation.
- Defining simulation region and boundary condition: As discussed above, the cell dimensions are very important for a reasonable simulation result, meaning that the mesh size should be reasonable and optimal, depending on the precision required and limitation of computing memory. A very fine mesh would result in very high usage of memory and would take long time to compute.
- Define a source of light: the incident light, a plane wave, usually propagated along the z direction with polarization in the x-direction.

- Defining the correct monitors: The correct field monitors should be applied in the correct direction and cross section depending on the area of interest, also the visual monitors should be applied correctly.
- Calculation Scripts: Scripts are required to calculate Enhancement Factors, some open-source scripts are available, for a specific application a special script might be required.

3.4 Synthesis of Metallic nanostructures for SERS application

3.4.1 Introduction

Recently metal nanostructures have received an ever-increasing interest owing to their remarkable properties and tunability to specific requirements, these areas include everything from catalysis, sensing, imaging to biomedicine. Our group has also been working on multiple usages of these nanostructures including sensing and biomedicine mainly focused on Cancer detection and therapy [90]. A myriad of metal nanostructures have been synthesized.

Using metal nanostructures for SERS is a successful example in this research field. It has been established that the EM enhancement is optimized by metallic nanostructures and due to the novel LSPR properties of Ag and Au they have been the biggest contenders as the optimal SERS substrate elements. While Au-based substrates are more stable, Ag based substrates have shown optimal performance. Multiple nanostructures have been synthesized and studied for this application, namely, nanowires, nanovoids, nanoflowers, nanocages, nanorods, nano-prisms. Among these nano dendrites have a special advantage as they are a highly fractal structures and with multiple hierarchal branches, provide a large specific area and a high density of hot spots. A variety of methods to fabricate Ag hierarchical nanostructures with diverse structural features have been employed which include electrochemical deposition [90-106], electroless redox reaction [107-123], wet chemical route using reducing agents in aqueous solution [124-

137], photocatalytic reduction [138, 139], decomposition by visible light irradiation [140], ultraviolet irradiation of surfactant micelles [141], ultrasonically assisted templated synthesis, iodination treatment to the evaporated Ag foil surface [142], sono-electrochemical deposition [143-147], and photoreduction by ultraviolet irradiation [148]. However, each of this method have some deficiencies, such as requiring special. equipment, time consuming (up to 30 days), impurity, using highly hazardous materials (e.g., HF), introduction of seed particles and templates, multiple capping agents, multiple synthetic steps, difficulties to remove the templates or surfactants from the surface of the products, high-cost or low- yield restrictions, and poor reproducibility.

3.4.2 Galvanic Replacement Reaction

The advantage of working with metallic nanostructures is that the properties can be tailored by adjusting the set of parameters such as composition, shape, size and internal structures. Control of these properties can lead to optimization of the nanostructure for a specific application. Many synthesis methods have been able to achieve this, but galvanic replacement offers an effective and versatile approach due to the ease of synthesis and ability to control all the required parameters and achieve desired results.

Galvanic replacement reaction is thermodynamically driven by a favorable difference between reduction potentials of the deposited metal and the sacrificial material. It is an electrochemical process that involves the oxidation of a metal (which is referred as sacrificial templates) by the ions of another metal having higher reduction potential. The Galvanic replacement method a is very effective way to make metal nanoparticles (MNPs) due to its ability to tune the size and shape, and to change the composition, morphology of the resultant nanostructures. Accordingly, even Ag nanoparticles ($Ag+/Ag$ E = 0.8 V vs. SHE) could serve as seeds and reducing agents for synthesis of more noble metal nanostructures such as gold ($Au3+/Au$ E = 1.5 V vs. SHE). Although the main governing principle of galvanic replacement is very straightforward, controlling the morphology and structure of produced nanostructures have not been that easy in all cases, as they are very sensitive to the synthesis condition. The synthesis parameters comprise of ion concentrations, temperature, and the initial state of the sacrificial material.

Table 1 : Reduction Potentials

Metal	Reaction	Electrode Potential (V)
Gold	$Au^{+} + e^{-} = Au$	+ 1.692
Silver	$Ag^{+} + e^{-} = Ag$	+0.7996
Copper	$Cu^{2+} + 2e^{-} = Cu$	+0.342
Iron	$Fe^{3+} + 3e^{-} = Fe$	-0.037
Lead	$Pb^{2+} + 2e^{-} = Pb$	-0.126
Nickel	$Ni^{2+} + 2e^{-} = Ni$	-0.257
Cadmium	$Cd^{2+} + 2e^{-} = Cd$	-0.403
Iron	$Fe^{2+} + 2e^{-} = Fe$	-0.447
Zinc	$Zn^{2+} + 2e^{-} = Zn$	-0.762
Aluminum	$Al^{3+} + 3e^{-} = Al$	-1.662

We have been studying Galvanic Replacement reactions and their potential application as synthesis techniques for variety of nanostructures and nanoparticles. The elements we have mainly explored are reduction of Ag on Zn and Cu, and reduction of Au and Pt on Ag. We achieved making ultra-small Au nanoparticles and bimetallic Ag-Au and Ag-Pt and Ag-Pt-Au nanoparticles using this synthesis method. These experiments and further potential tunability of these multi-elemental nanostructures were explored into making versatile and highly sensitive SERS substrate.

As one of the simplest galvanic reactions, the reaction of $AgNO_3$ with Cu has indeed been used in high school chemistry class to demonstrate the galvanic reaction and crystal growth. The formation of Ag dendrites can be explained by a simple reaction mechanism as follows.

Reduction reaction first takes place on Cu, and then on newly formed Ag.

$\mathbf{Ag^{+} + e^{-} \rightarrow Ag}$,

The electron comes from the oxidation reaction, which takes place at Cu surface where Cu^{2+} is released into the solution, and electron transport inside metal to Ag surface to reduce Ag^{+}.

$\mathbf{Cu \rightarrow Cu^{2+} + 2e^{-}}$,

The reduction reaction rate is higher on Ag (111) surface, leading to preferred growth along [111] direction which results in the formation of Ag dendrites.

4 New insight into Single-Crystal Silver dendrites formation and Growth Mechanisms

4.1 Introduction

Silver dendrites usually form on the surface of the substrate. As one of the simplest galvanic reactions, the reaction of $AgNO_3$ with Cu has indeed been used in high-school chemistry classes to demonstrate the galvanic reaction and crystal growth. However, our experimental observations, reported here, contradict this formation mechanism, revealing a much more complicated scenario for this simple galvanic reaction. Interestingly, when we tried to use this simple reaction to form Ag dendrites inside the channels (~300 nm) of anodic aluminum oxide (AAO) membranes by depositing Cu at one end to cover the channels and adding $AgNO_3$ solution into the membranes, a large amount of well-defined Ag dendrites was observed on the top surface of the AAO membrane without any direct connection to the Cu layer at the bottom. We conducted a series of experiments to explain this surprising result and proposed new reaction and Ag dendrite formation mechanisms. This study is not only scientifically intriguing but also technologically important. The galvanic replacement reaction has widely been employed to synthesize Ag dendrites, but there is very little control over the size and shape of such nanostructures. To better utilize Ag dendrites for various applications, controlled dendrite growth is highly desirable, which requires the full understanding of the reaction and formation mechanisms.

4.2 Experimental part

Chemicals and Reagents. $AgNO_3$ was purchased from Alfa Aesar. AAO membranes (Whatman Anodisc Inorganic Filter Membrane, 0.2 µm pore size, 47 mm diameter, supported) were obtained from Sigma-Aldrich. They were used as received. The water used throughout all these experiments was purified with a Millipore system. Synthesis of Silver Dendrites.

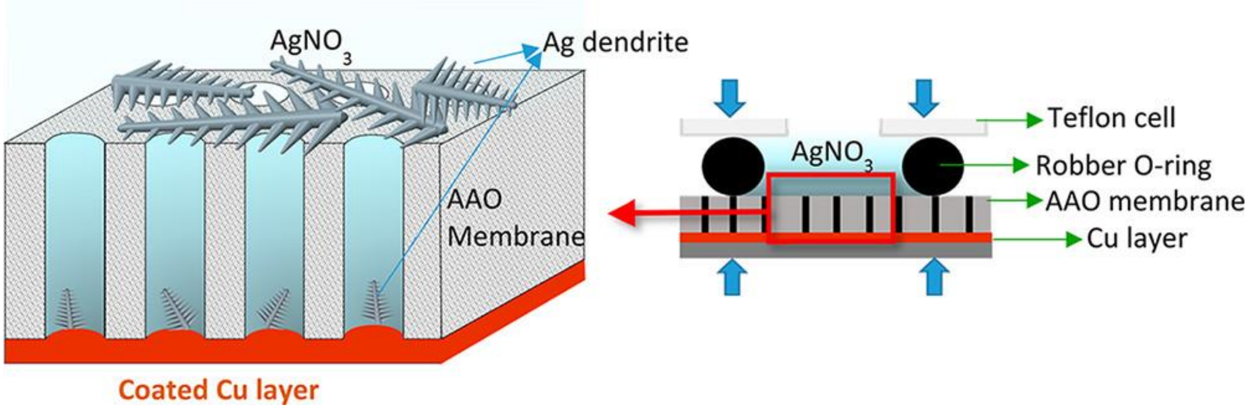

Figure 9 : Schematic illustration of silver dendrite formation will AAO membrane barrier

The schematic illustration of the whole experimental setup is depicted in Fig. 9, in which an AAO membrane was put on a flat surface (silicon wafer), and a sealed Teflon cell with a diameter of ~1 cm was placed on the top of the AAO membrane. The bottom side of the AAO was deposited with a 500 nm Cu layer by a thermal evaporator. The deposition rate was set to 4 ± 1 Å/s. $AgNO_3$ solution (1 ml unless otherwise stated) at different concentrations (0.01 to 1 M) was poured into the cell for different reaction times (10 to 11 s; the reaction was stopped by pouring out the $AgNO_3$ solution. The $AgNO_3$ solution could reach the Cu surface only through the channels of the AAO membrane. Interestingly, and to our surprise, highly branched and symmetrical Ag dendrites were obtained on the top surface of the AAO membrane without any direct connection to the Cu layer at the bottom (the initial incentive of this experiment was to form silver dendrites inside the channels of the AAO membrane). The formed Ag dendrites on the top side of the membrane were collected and washed with DI water through several cycles of centrifugation at 8000 rpm for 5 min for scanning electron microscopy (SEM) and transmission electron microscopy

(TEM) analyses. Characterization. The morphology of the AAO membrane before copper coating, after copper coating, and its cross-section after silver dendrite formation was examined by field-emission scanning electron microscopy (FE-SEM, Zeiss Supra 55 VP) at 10 kV. The crystalline structure was characterized by X-ray powder diffraction with a Cu Kα source (Siemens D800) scanning from 20° to 90° at the rate of 2° per minute. The single-crystal structure analysis was characterized by high-resolution transmission electron microscopy (HRTEM, Hitachi H-9500 high-resolution).

4.3 Results and Discussion

The SEM micrographs of the AAO membrane surface before and after the copper coating are shown in Fig. 10 a, b, respectively.

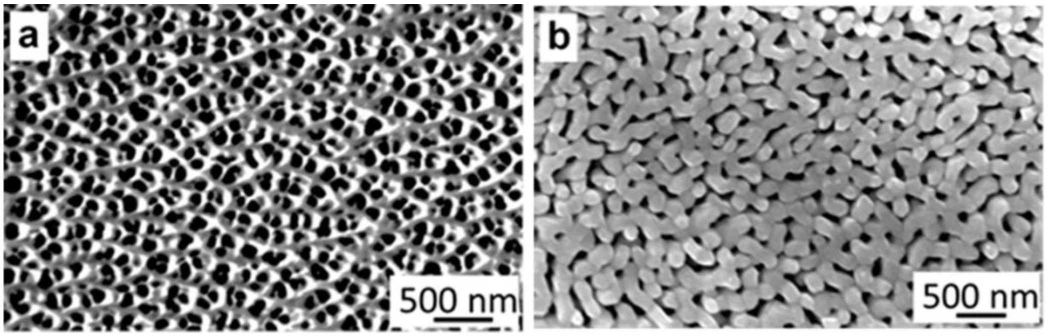

Figure 10 : SEM micrographs of (a) AAO membrane (b) Cu coated AAO membrane

As can be seen, the Cu coating did not become a uniform thin film, but rather formed a wormlike structure covering the holes due to the porous structure of the AAO membrane surface. The galvanic replacement reaction normally operates through a direct redox reaction between the sacrificial and the deposited metals. The SEM micrographs (Fig. 11) of the cross sections of the AAO membrane clearly show the formation of Ag dendrites inside these 300 nm channels.

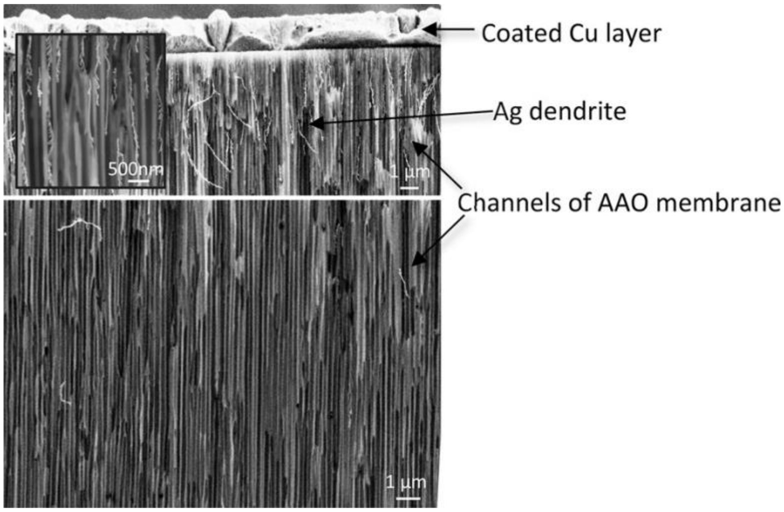

Figure 11 : SEM micrograph of cross-section on AAO membrane after the dendrite formation

The maximum length of these dendrite structures is ∼20 µm, which is approximately one-third of the entire channel length. However, a large amount of the Ag dendrite structures appears on the top surface of the AAO membrane, as shown in Fig. 12.

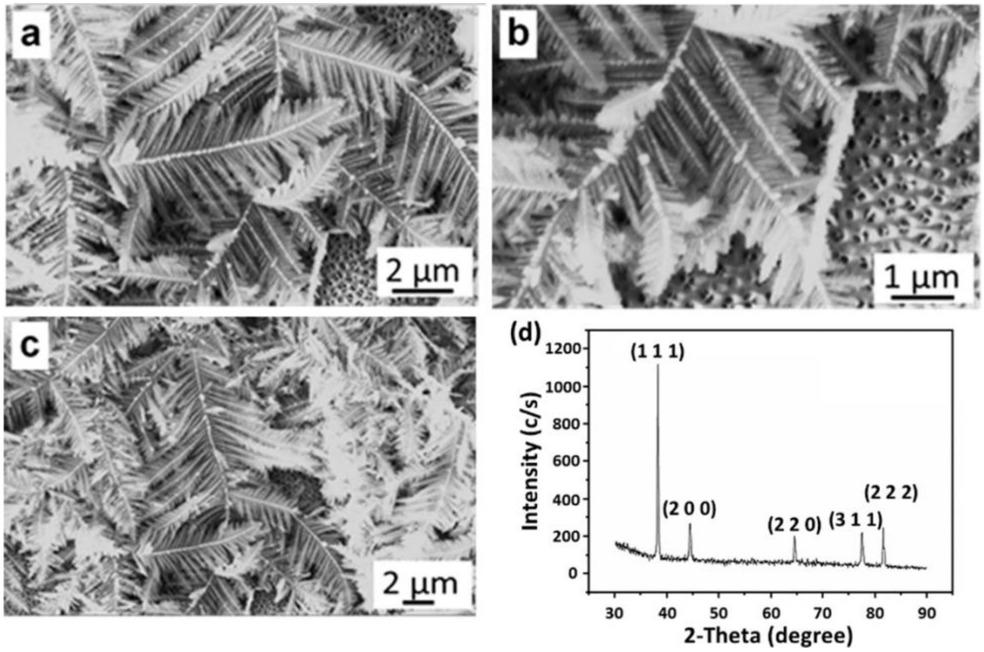

Figure 12 : SEM Micrographs of dendrites formed on top of the AAO membrane and (d) EDAX for the dendrites

Obviously, no connection exists between the Cu layer (sacrificial material) and the produced Ag dendrites (deposited metal) on the top surface of the AAO membrane. Thus, the question is how the Ag dendrites can form far away from the Cu surface. To confirm this observation that an Ag dendrite can form without connection with Cu, we replaced the AAO membranes with dialysis membranes that have a molecular weight cutoff (MWCO) of 2000 kDa. A dialysis membrane is an artificial semipermeable membrane. The pore size for dialysis membranes with MWCO of 2000 is less than 1 nm. Such a membrane only allows small molecules to pass through. It is impossible for metal Ag to form a continuous line passing through the membrane. Again, Ag dendrites were observed (see Fig. 13) on the top surface of the membrane. This undoubtedly confirms that Ag dendrites can form without connection to Cu, which cannot be explained by the simple galvanic replacement reaction of Ag and Cu. This clearly indicates that the reduction of Ag^+ with Cu can also take place.

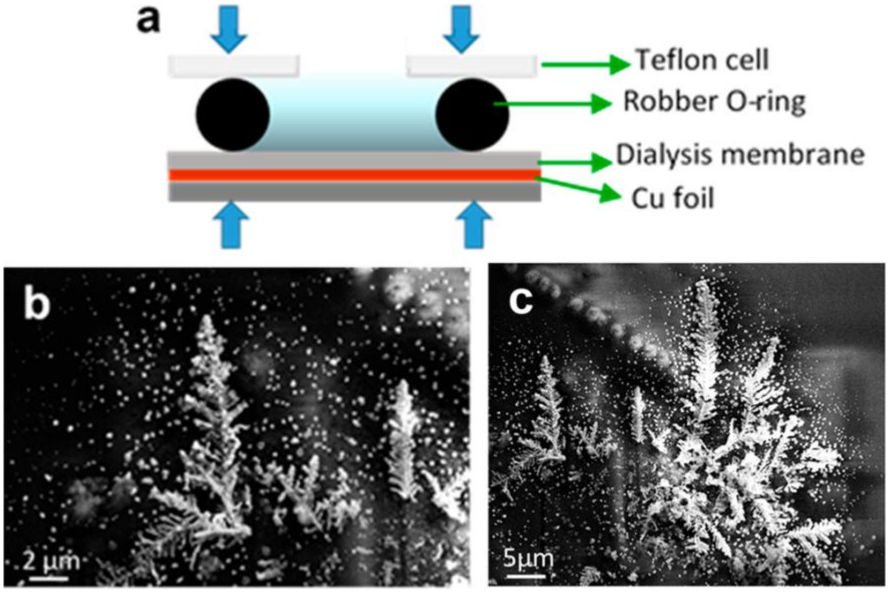

Figure 13 : (a) Schematic of the experimental setup for silver dendrite formation with dialysis membrane as a barrier (b, c) SEM Micrographs : top of the dialysis membrane

4.3.1 Proposed Reaction Mechanism

All possible ion species inside the solution include Ag^+, NO_3^- (nitrate), Cu^{2+} (cupric), NO_2^- (nitrite), and Cu^+(cuprous). Among them, NO_2^- and Cu^+ are the only possible intermediate ions. The concentration of Cu^+ ions would be extremely low, since Cu^+ is not stable in aqueous solution. Therefore, the intermediate ion that assists to reduce Ag^+ into metal Ag must be NO_2^-. It is known that Cu can reduce NO_3^- to NO_2^- through the following reaction.

$$Cu_{(s)} + NO_{3\,(aq)}^{-} + 2\,H_{(aq)}^{+} \rightarrow Cu_{(aq)}^{2+}\; NO_{2\,(aq)}^{-} +\; H_2O_{(l)}$$

Ag^+ ions could subsequently be reduced by the resultant nitrite ions via the reaction

$$Ag_{(aq)}^{+} +\; 2\,NO_{2\,(aq)}^{-} +\; 2\,H_2O \;\rightarrow\; Ag_{(s)} +\; 2\,NO_{3\,(aq)}^{-} +\; 4\,H^{+}$$

which results in Ag dendrite formation and growth.

4.3.2 Griess Reagent Test

We confirmed the existence of nitrite ions in the solution using the Griess test, which is a standard analytical chemistry technique detecting the presence of nitrite ion in solution. This method is considered as a spectrophotometric assay, which is based on the formation of an azo dye by the reaction of NO_2^- ions with the Griess reagent, which typically contains 0.2% naphthyl ethylenediamine dihydrochloride and 2% sulfanilamide in 5% phosphoric acid. Specifically, NO_2^- reacts straightforwardly with sulfanilamide under acidic conditions and is then revealed after diazotization with N-(1-naphthyl)-ethylenediamine (NED). Colorimetric techniques based on the Griess reaction basically indicate nitrite ions that, under produce an azo compound, which strongly absorbs in the visible region with a peak around 545 nm.

Table 2 : Griess Reagent Test Results

	Solution	Reaction Time	Homemade Griess Reagent	Commercial Griess Reagent
1.	1M $AgNO_3$ on Copper plate covered with Filter paper	15 min	**Positive**	**Positive**
2.	1M $AgNO_3$ on Copper plate covered with Filter paper	30 min	**Positive**	**Positive**
3.	0.1M $AgNO_3$ on Copper coated AAO membrane	5 min	**Negative**	**Negative**
4.	0.1M $AgNO_3$ on Copper coated AAO membrane	15 min	**Positive**	**Positive**
5.	0.1M $AgNO_3$ on Copper coated AAO membrane	30 min	**Positive**	**Positive**
6.	1M $AgNO_3$ on Copper coated AAO membrane	15 min	**Positive**	**Positive**
7.	1M $AgNO_3$ on Copper coated AAO membrane	30 min	**Positive**	**Positive**
8.	1M $AgNO_3$ on Copper plate covered with 2 kDa MWCO dialysis membrane	15 min	**Positive**	**Positive**
9.	1M $AgNO_3$ on Copper plate covered with 2 kDa MWCO dialysis membrane	30 min	**Positive**	**Positive**
10.	0.1M $AgNO_3$ on Copper plate covered with 2 kDa MWCO dialysis membrane	30 min	**Positive**	**Positive**

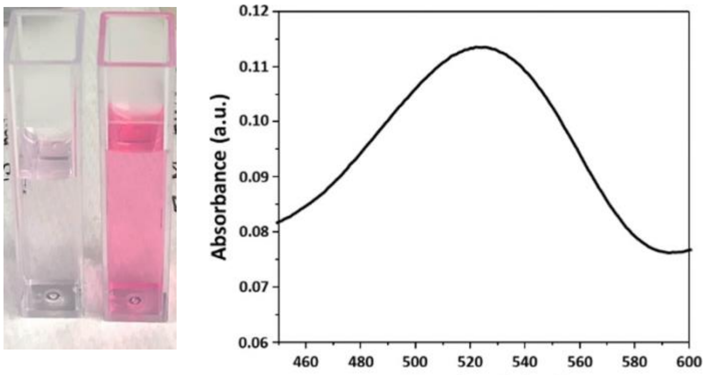

Figure . a. Griess Test result for Solution taken from top of AAO membrane after reaction with Copper coated under the Membrane, with 0.5M $AgNO_3$ for 15mins.

b. Griess Test result for Solution taken from top of Dialysis membrane after reaction with Copper coated under the Membrane, with 0.5M $AgNO_3$ for 15mins.

Figure 14 : Griess reagent test UV-VIS results

For this purpose, one drop of the solution and one drop of DI water were mixed, and the resultant mixture was analyzed using UV−vis spectroscopy. Fig. 14 demonstrates the result of a UV−vis test including a peak at ∼545 nm, which clearly indicates the existence of nitrite ions above the AAO membrane.

4.3.3 Reaction Mechanism of Silver Dendrite formation

We can conclude that the formation mechanism of Ag dendrites inside and above the AAO membrane is as follows (illustrated in Fig. 15): formation of the dendrites inside the nanochannels only happens at the lower part of AAO membrane near the Cu layer, and these dendrites form by the direct galvanic replacement reaction. At the same time, NO_3^- ions are reduced by Cu into NO_2^- ions. However, the direct galvanic replacement reaction is faster than the diffusion of Ag^+ ions from the bulk solution to the bottom volume close to the Cu layer, which quickly depletes the available Ag^+ ions. NO_2^- ions formed on the bottom diffuse into the bulk solution, where Ag^+ ions are reduced by NO_2^- ions to form dendrites on the top of the AAO membrane.

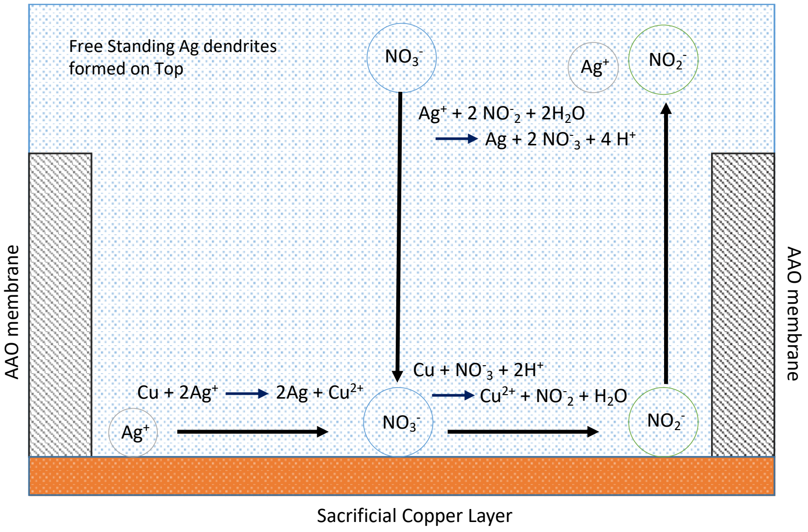

Figure 15 : Proposed reaction mechanism

4.3.4 Growth Mechanism of Silver Dendrites

To gain better insight into the growth mechanism of the Ag dendrites, their evolution process was investigated by a series of time-dependent electron microscopy experiments. These experiments were conducted with a fixed concentration of 0.06 M $AgNO_3$ solution for different reaction times of 10, 30, 60, and 120 s. Intermediate products were collected at each stage, and their morphology and structure were characterized by SEM and TEM, presented in Fig. 16. The SEM image of the Ag nanostructure obtained in an interval of 10 s (Fig. 16 a) demonstrates that it consisted of a jagged-shape particle with a core of ∼200 nm in diameter and protrusions of ∼50 nm. It can also be seen that the jagged particle is surrounded by several small nanoparticles. A high magnification TEM image of the same sample (Fig. 16 b) shows that the observed nanostructures are in fact a cluster of small irregular Ag nanoparticles that have been partially attached to each other. Some of the nanoparticles in the aggregations are as small as 5 nm. Increasing the experiment time to 30 s would provide sufficient time for some of the observed nanostructures formed in 10 s to grow and form an imperfect dendrite-like Ag structure of a main trunk with a length of ∼1 µm and small, first-generation branches in the range of 100−200 nm (Fig. 16 c, d). Note that the Ag nanostructures similar to what formed in 10 s still exist at 30 s, and the small dendrite-like structures are

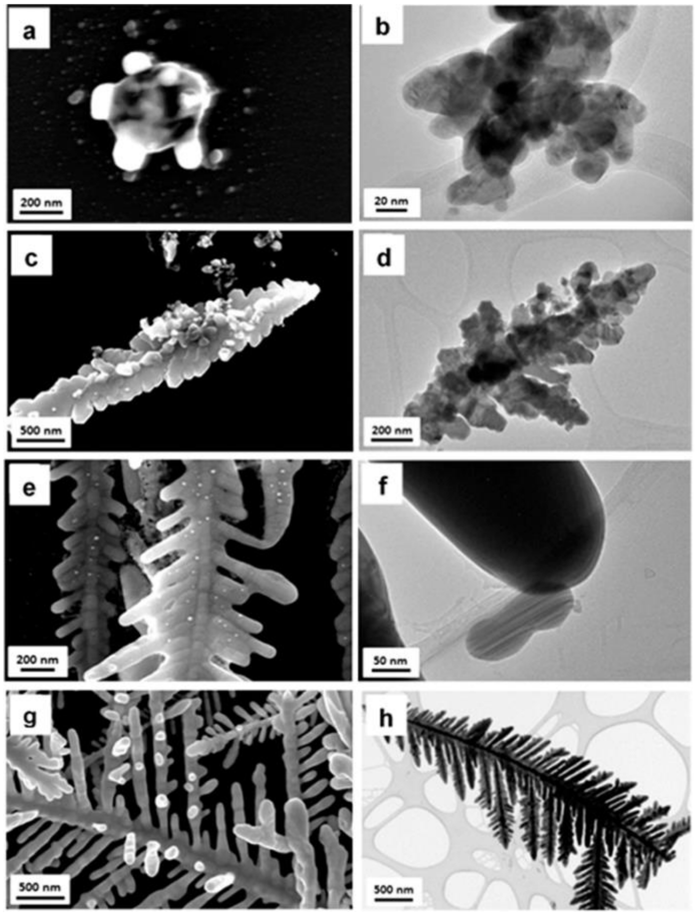

Figure 16 : Stepwise SEM micrographs silver dendrite growth mechanism

accompanied by individual and aggregates of nanoparticles. When the reaction proceeded for 60 s (Fig. 16 e, f), the branches grow more (a few hundreds of nm), creating more resemblance to a dendritic structure. As can be seen from the SEM image (Fig. 16 e), the cluster of nanoparticles does not exist anymore after 60 s, whereas the small individual nanoparticles are still present all around and on the dendrites. Fig. 16 f depicts a TEM image of one of those nanoparticles (~100 nm) at the tip of a branch. Extending the reaction time to 120 s would result in the formation of well-established Ag dendrites with up to four generations of branches closer to the root of the main trunk and one generation of branches at the vicinity of the tip (Fig. 16 h). Another discernible feature of the sample prepared with 120 s of reaction time is the absence of the previously observed nanoparticles (Fig. 16 g). Instead, a few new branches can be seen to have grown upward from the dendrite trunk, which implies the 3D growth path of the Ag dendrites. All the process over a 120 s time interval resulted in the development of 3D, highly branched Ag dendrites with a main trunk in the micrometer scale and branches from a few nanometers to a few micrometers. Increasing the reaction time from 120 to 180 s would not alter the morphology and structure of the Ag dendrites but would rather enlarge the average size and number of them. The achieved results at different time points can help to better understand the multiple steps that occurred during the growth of the Ag dendrites through the experimental procedure in this study. It has been stated that the formation of the anisotropic nanostructure with the intrinsic symmetric cubic crystals in solution is difficult when the synthesis is performed in a homogeneous solution without using any polymer or surfactant agent. In the case of dendritic structure, it is generally accepted that the nonequilibrium condition in which a kinetic factor dominates the thermodynamic one would cause the anisotropic crystal growth. Several models, including the deposition, diffusion, and aggregation (DDA), the diffusion limited aggregation (DLA), oriented attachment (OA), and the cluster−cluster aggregation (CCA), have been proposed for the formation of silver dendrites, where DLA and the oriented attachment or a combination of those two have been more popular than other mechanisms to interpret the growth process of silver dendrites in solution. On the one side, DLA refers to the formation of fractal structures through random aggregation and the asymmetric growth of nanoparticles when the growth rate is limited by the diffusion rate of solute atoms (also identified as random walkers) to the reaction interface. On the other side, oriented attachment is the process of the spontaneous self-assembly/alignment of adjacent particles so that they share a common crystallographic orientation, which leads to the joining of these particles at a planar interface. Generally speaking, considering only one of these mechanisms to explain the formation of Ag dendrites effectively oversimplifies the real phenomena. Hence, multiple mechanisms acting simultaneously have been commonly invoked to specify the growth process of Ag dendrites. In our study, at the very beginning, silver ions are reduced to atoms and come together to form nuclei. Nuclei rapidly grow to form stable nanocrystals. These nanocrystals would have facets, which minimizes the total surface energy. It has been calculated that a multiply twinned decahedron with (1 1 1) facets would have the lowest surface energy. We can expect, during the nucleation stage, that stable multiply twinned decahedron nanoparticles would be abundant in the solution. These nanoparticles can stack together by an oriented attachment to form an elongated structure with (1 1 1) facets at the end and with protrusions on the sides, generating a dendrite embryo. The subsequent growth of the branched aggregates of nanoparticles (dendrite embryo) could continue by a number of mechanisms, including diffusion-limited aggregation, oriented attachment, and Ostwald ripening. Accordingly, as the reaction proceeds, some of the small nanoparticles diminish by Ostwald ripening, and some of them might have sufficient time to relax and fuse to minimum energy positions, thus contributing to the formation of single-crystal Ag dendrites. The continuous heterogeneous nucleation and growth of ultrasmall Ag nanoparticles during the entire course of the formation of Ag dendrites can be better seen at later stages, where some dendrite branches established, as shown in Fig. 17. Therefore, while it has been proposed that the particle-mediated crystal growth is one of the determining mechanisms of the formation of Ag dendrites inside solutions, in the present experiment procedure, the continuous heterogeneous nucleation and growth have played a major role. This process is thermodynamically favorable, as it decreases the overall surface energy of the system. At later stages, the protrusions of the dendrite-like Ag structures will continue to their anisotropic growth as they progress into the region of high Ag ion concentration ahead of the growth interface, while a dendritic structure can physically adsorb the remaining small nanoparticles once they come in contact with each other. As the stems from the main trunk grow in length, new shorter branches are formed continuously at the tips, resulting in the formation of well-established, highly branched dendritic structures. The TEM image of a complete Ag dendrite synthesized after 180 s using 0.06 M $AgNO_3$ solution along with its corresponding HRTEM images and diffraction patterns are shown in Fig. 18.

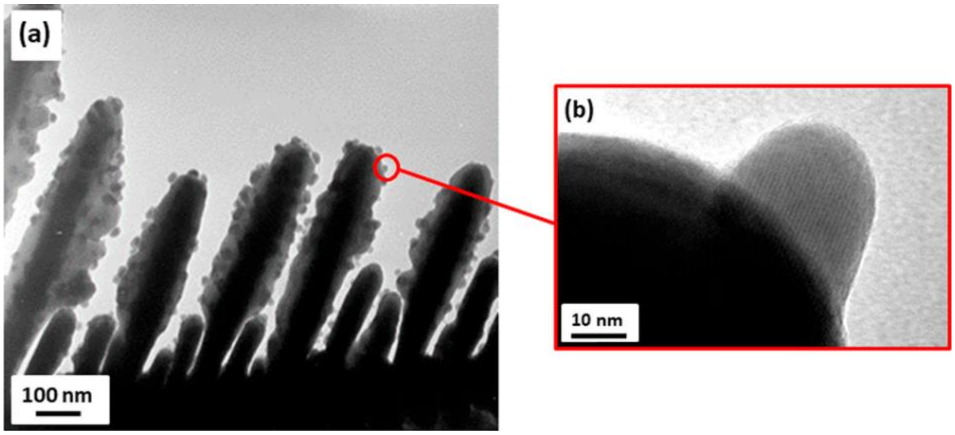

Figure 17 : Nucleation and growth of silver dendrites

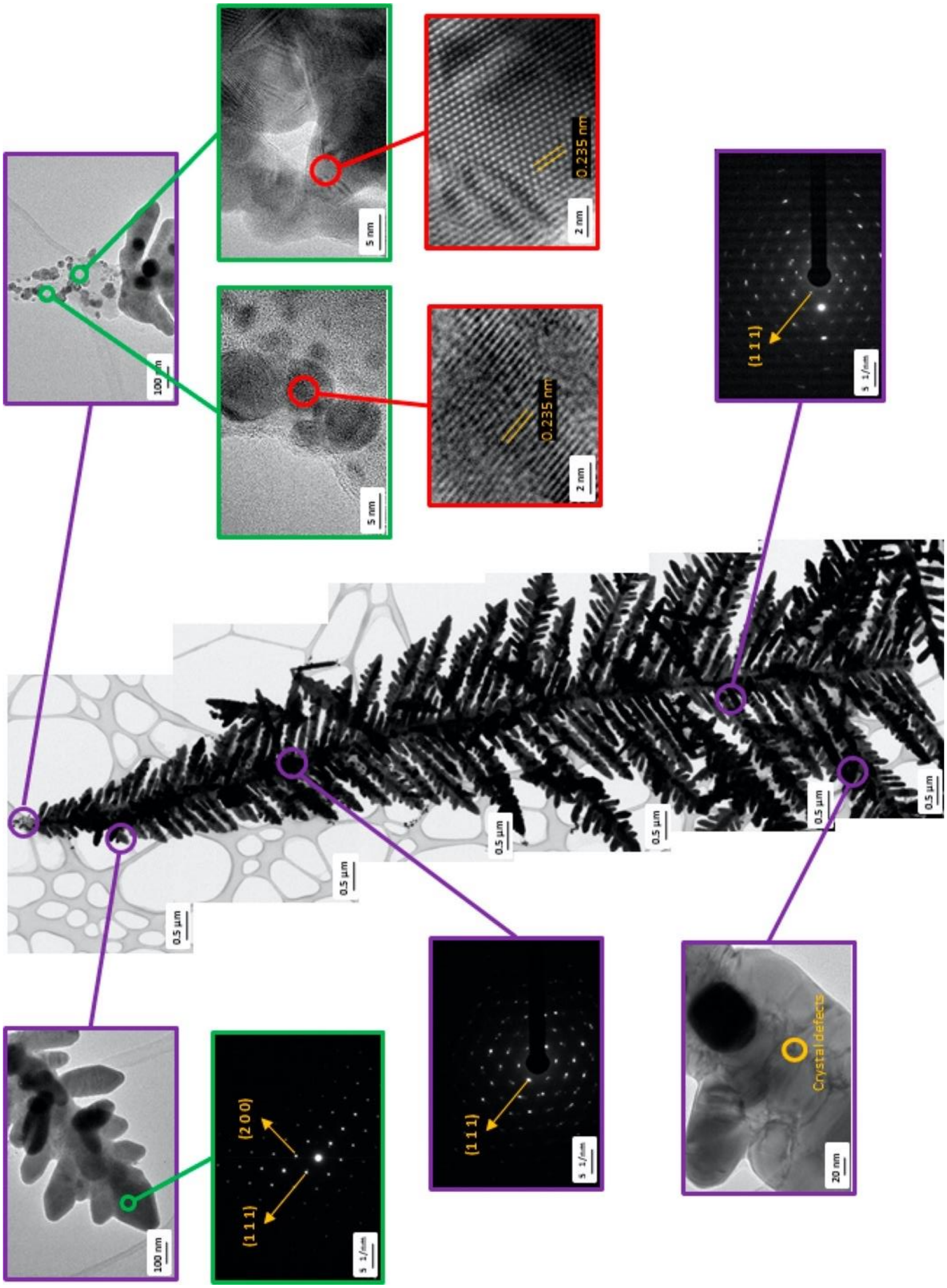

Figure 18 : HRTEM images and Diffraction patters for Silver Dendrites

The selected area electron diffraction (SAED) patterns from different locations of the Ag dendrites from its main trunk to the tip of its last branches demonstrate that the dendrite is a single crystal. It can clearly be observed that the dendrite at the very top was growing through the connection of small Ag nanoparticles, with the preferential growth direction of [1 1 1]. The synthesis process of the Ag dendrites, which starts by the formation very small Ag nanoparticles and grows through a particle-mediated process, is under the influence of different parameters including concentration gradient, reduction rate, and diffusion, which are all dependent on the initial concentration of the reactants. Hence, the relation between the morphology and structure of the Ag dendrites and reactants concentrations was also investigated. It is expected that the product morphology would be strongly determined by the reactant concentrations, as it can affect both the thermodynamic and kinetic characteristics of the reaction. The SEM images of the Ag structures fabricated at different silver ion concentrations for a fixed reaction time of 180 s are shown in Fig. 19. As can be observed from Fig. 19 a, $AgNO_3$ concentration as low as 0.01 M was not enough to produce Ag dendrites in a time frame of 180 s. Alternatively, some structures formed that are pretty similar to the nanoclusters observed after reaction for 10 s by 0.06 M of $AgNO_3$. Note that

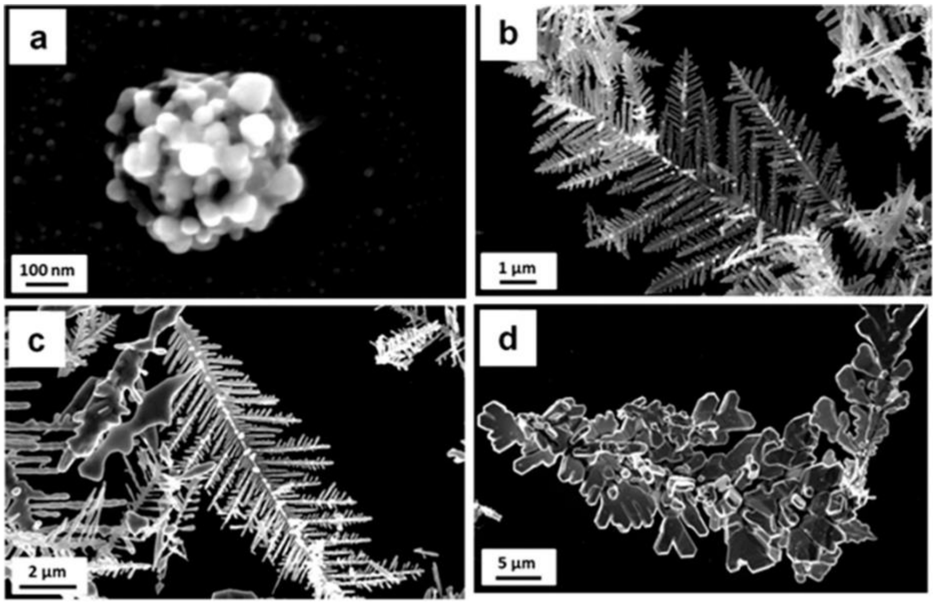

Figure 19 : Ag structures synthesized at different ion concentrations

lowering the concentration of $AgNO_3$ solution is in fact a decrease in both the concentration of Ag^+ ions and the amount of reducing agents.

Thus, lowering the reactant concentrations from 0.06 to 0.01 M dramatically changed the obtained Ag products within a reaction time of 180 s. Moreover, it can be inferred that reducing the concentration had similar effects as lessening the reaction time, without altering the growth mechanism. The samples obtained with ion concentrations of 0.06 and 0.12 M are demonstrated in Fig. 19 b, c, respectively. It appears that doubling the concentration up to 0.12 M will not have any noticeable changes to the morphology of the Ag dendrites as compared to those produced at 0.06 M, except minor coarsening of the branches and increasing the average size of the synthesized dendrites. However, when the concentration is increased to 1 M, the obtained Ag structures (Fig. 19 d) considerably differ from those observed at lower concentrations. Although the overall shape of the produced structure still resembles a dendrite, the ordered fine branches were replaced by coarse platelike stems with polygonal facets at their tips. When metal atoms are generated at a sufficiently high rate, the final product would have no option but to take the thermodynamically favored shapes of multiply twinned particles (MTPs). Thus, it is evident that the very high concentration of 1 M caused a significant increase in the reduction rate of Ag ions, enabling the growing Ag structures to become thermodynamically closer to the favorable shapes. It can also be considered that a higher concentration of Ag^+ ions allowed lateral growth to compete with linear growth, as the growth interface is spatially surrounded by a large number of Ag^+ ions without the obligation of a long-order diffusion to compensate their consumption.

5 3D Substrate : Glass Capillary Device

Considering the aforementioned results from our dendrites inside filter membranes experiments, it was evident that a bigger cross-section was required for developing similar substrates. We experimented with multiple shapes and sizes of capillaries and settled on square cross-sectional capillaries, commercially available and acquired from *Vitrocom Inc*. The IDs that we trialed were ranging from 0.1 mm to 1 mm. Best results were observed in 0.5 ID capillaries with 0.2 mm capillaries acting as blockades for the flowout of the dendrites. Using capillaries provides an easy way to flow liquid for synthesis as well as detection. Square capillaries also reduce the interference to incident laser caused due to curvature of the circular capillaries.

Fig. 20 demonstrates the schematic of the setup used for 3-D Ag dendrite fabrication. Two pieces of Cu wires with the length of 40 mm were cut and after ultrasound cleaning in acetone and deionized (DI) water, inserted into the bigger glass capillary. Then two pieces of 200 μm thick capillary were inserted into the 500 μm capillary halfway to create a tapered structure to prevent flowout of silver dendrites during the $AgNO_3$ injection. Consequently, the resultant capillary design was connected to syringe through a rubber connector. All the connections were sealed with the UV cured epoxy to prevent any leakage. $AgNO_3$ solution with the concentration of 0.1 M was injected through the setup with a rate of 0.5 ml/min. Special care was taken while pouring out $AgNO_3$ solution to maintain integrity of freshly formed Ag dendritic nanostructures.

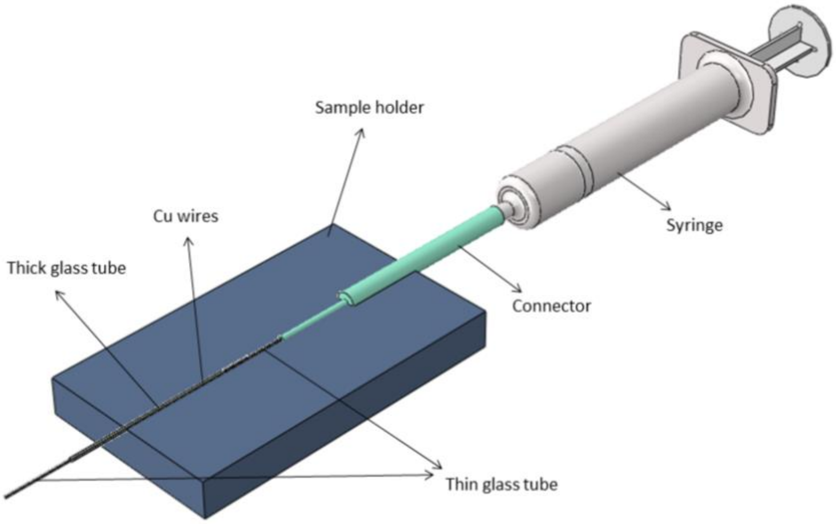

Figure 20 : Experimental Setup for 3D substrate synthesis

5.1 Characterization of Ag dendrites formed inside the glass tube

The Ag dendrites are too small to be observed under optical microscope. Scanning electron microscope (SEM) was used to characterize the dendrite structures, and therefore, the tube was broken to expose dendrites inside. From SEM micrographs, it can be seen that the structures formed inside glass tube can be divided into four separate regions according to the distance from the entrance of capillary, as shown Fig. 21.

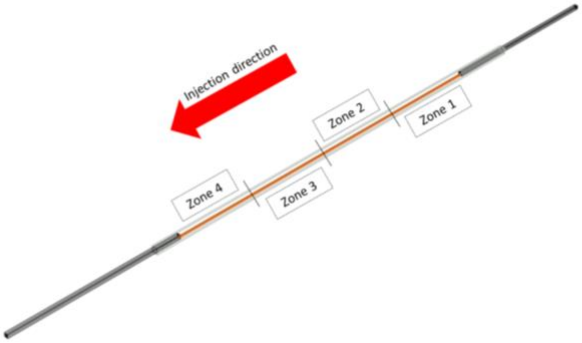

Figure 21 : Glass capillary and flow direction

SEM micrographs of Ag nanostructures formed in these 4 zones are shown in Fig. 22. In Zone 1 (Fig. 22(a)) the 3-D microstructure of Ag dendrites containing a high number of intersections and branches which are potential regions for SERS activity. The distribution of dendritic structure is almost homogenous, and all the dendrites have been developed completely. The average size of the main trunk and the secondary branches are about 5 µm and 500 nm, respectively. Moreover, some small nanoparticles with the average size of about 75 nm could be found on the main trunk of dendrites.

Similarly, zone 2 in Fig. 22 (b) contains the same combination of dendrites and nanoparticles but the size of particles increases to about 500 nm and some of them have been aggregated throughout the microstructure. The distribution of dendritic structure is not homogenous. That is, in some of them the secondary and tertiary branches have been grown more than that is found in zone 1, but also there are some dendrites with undeveloped branches. Fig. 22 (c) demonstrates that the number of dendrites in zone 3 decreases drastically and, instead, the microstructure includes aggregation of particles. Moving towards zone 4, the dendritic structure absolutely transformed to a particle-aggregated fractal pattern and there is no effect of Ag dendrites where the microstructure includes a combination of isolated Ag nanoparticles, nanoplates and hexagonal Ag nanoparticles. No dendrites formed. (see Fig. 22 (d)).

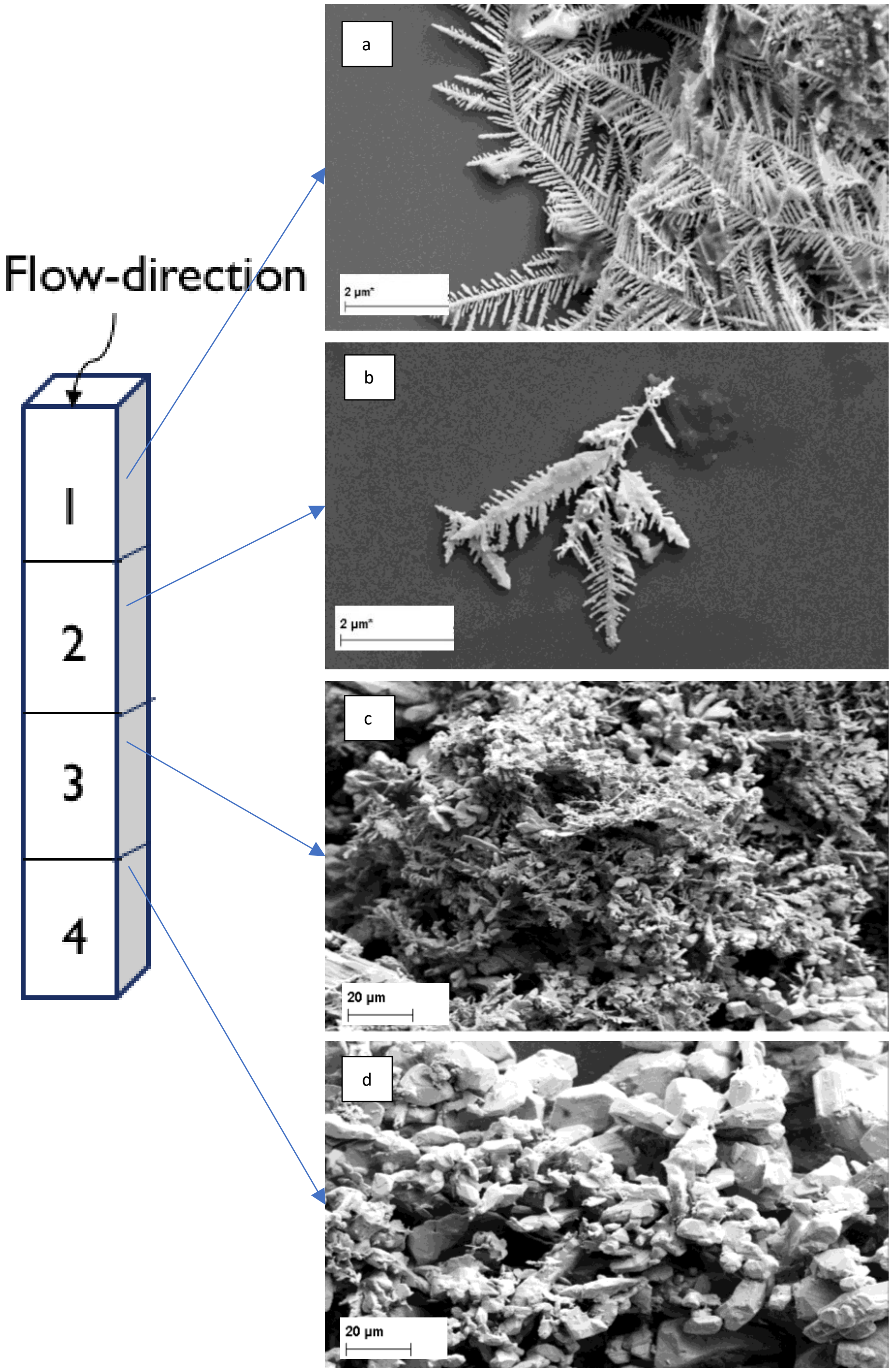

Figure 22 : SEM micrographs of changes in silver structure with different zone in the capillary dependent on the flow direction

5.2 SERS Results and Discussion

After preparing 3-D Ag dendrite setup, R6G was injected into the capillary by syringe to test the device for SERS activity. Aqueous solution of R6G was prepared with different concentration of 10^{-4} M, 10^{-6} M, 10^{-8} M, 10^{-10} M, 10^{-12} M, and 10^{-4} M. Fig. 23 demonstrates the SERS spectra for different concentration of R6G. For each definite concentration of R6G, spectra were obtained at four different zones. Spectra obtained for 10^{-4} M R6G showed characteristic Raman peaks 610 cm^{-1}, 767 cm^{-1}, 1184 cm^{-1}, 1360 cm^{-1}, 1510 cm^{-1}, 1570 cm^{-1}, and 1651 cm^{-1} which correspond to C-C-C ring in-plane, C-H out of plane bending, C-H in-plane bending vibrations, C-O-C stretching and C-C stretching of ring. However, as it was expected from microstructural observation for different zones, zones 1 and 2 give the sharpest peaks thanks to the dendritic structure, and consequently, existence of more hot spots. Accordingly, the peak height in spectra obtained from zones 3 and 4 are much smaller than in zone 1 and zone 2.

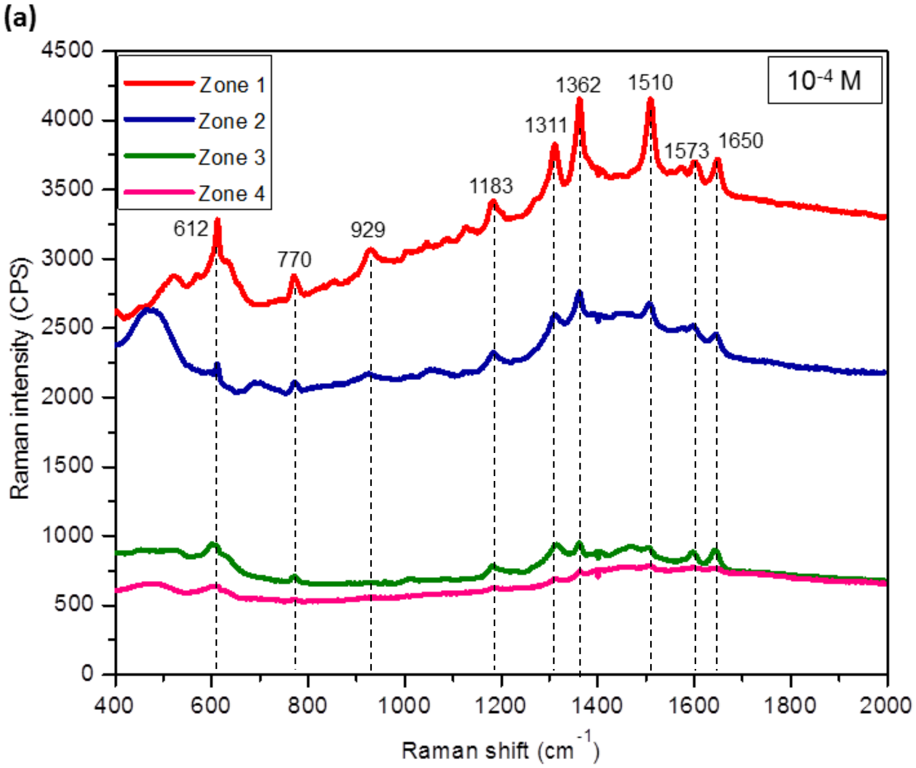

(b)

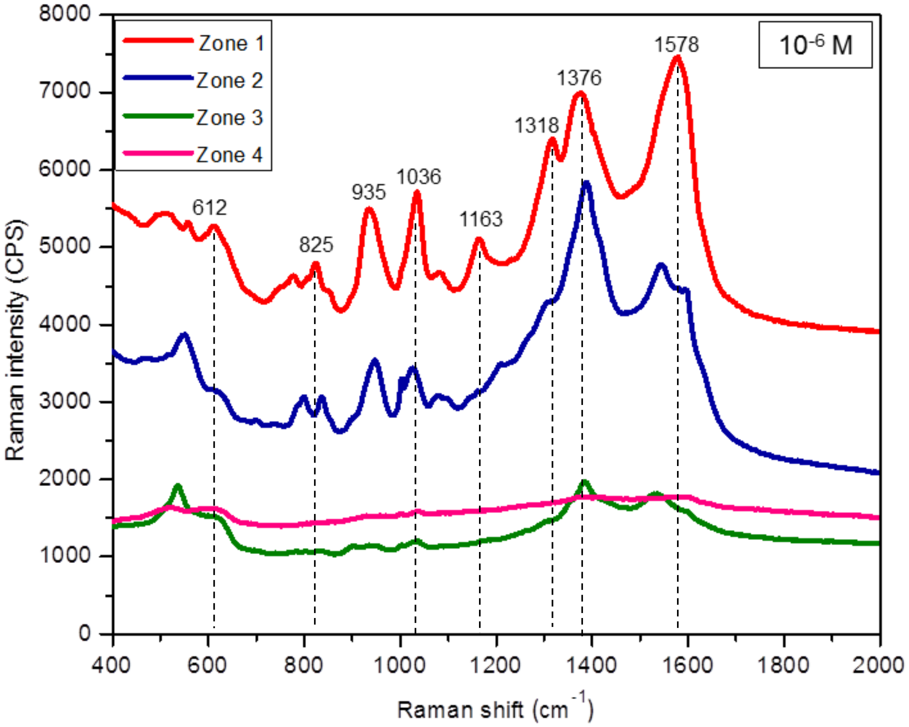

Zone 1
Zone 2
Zone 3
Zone 4
10^{-6} M
612
825
935
1036
1163
1318
1376
1578
Raman intensity (CPS)
0
1000
2000
3000
4000
5000
6000
7000
8000
400
600
800
1000
1200
1400
1600
1800
2000
Raman shift (cm^{-1})

(c)

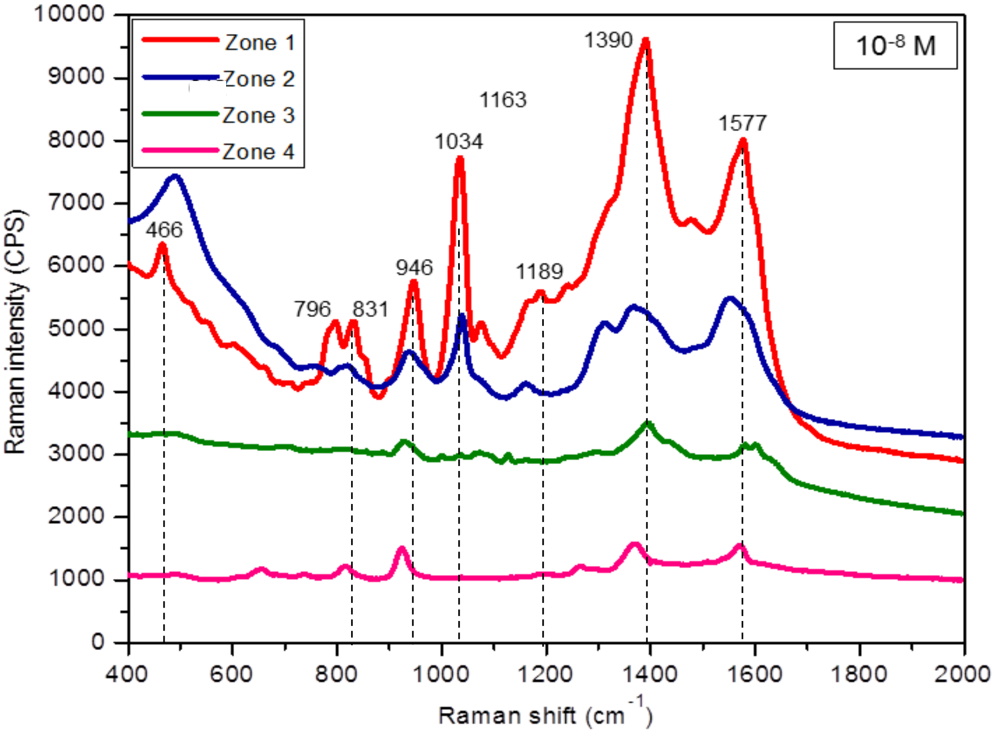

Zone 1
Zone 2
Zone 3
Zone 4
10^{-8} M
466
796
831
946
1034
1163
1189
1390
1577
Raman intensity (CPS)
0
1000
2000
3000
4000
5000
6000
7000
8000
9000
10000
400
600
800
1000
1200
1400
1600
1800
2000
Raman shift (cm^{-1})

(d)

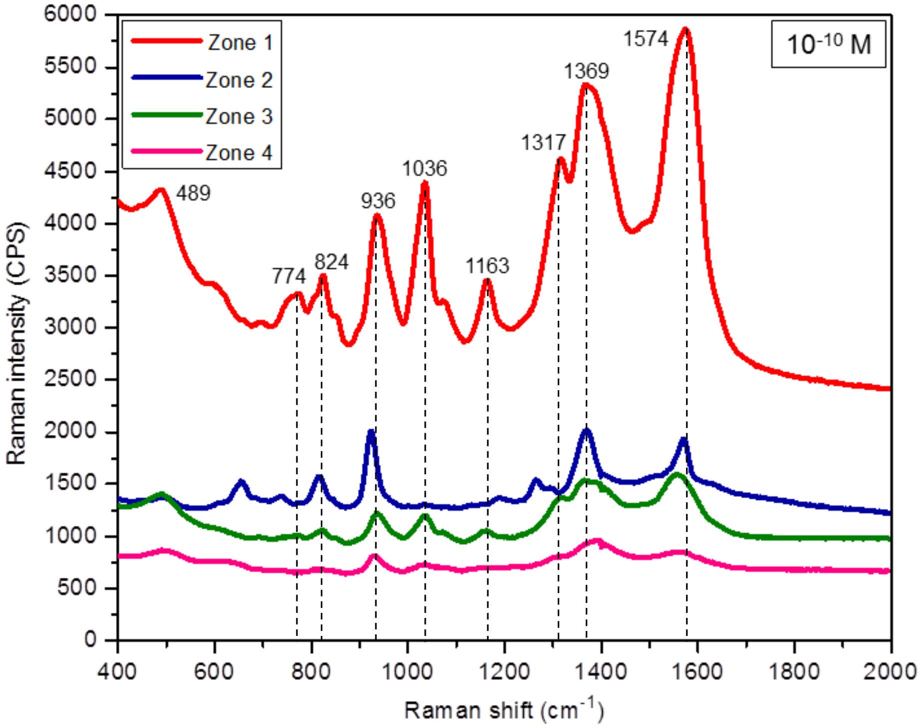
Zone 1
Zone 2
Zone 3
Zone 4
10^{-10} M
489
774
824
936
1036
1163
1317
1369
1574
Raman intensity (CPS)
Raman shift (cm^{-1})
0
500
1000
1500
2000
2500
3000
3500
4000
4500
5000
5500
6000
400
600
800
1000
1200
1400
1600
1800
2000

(e)

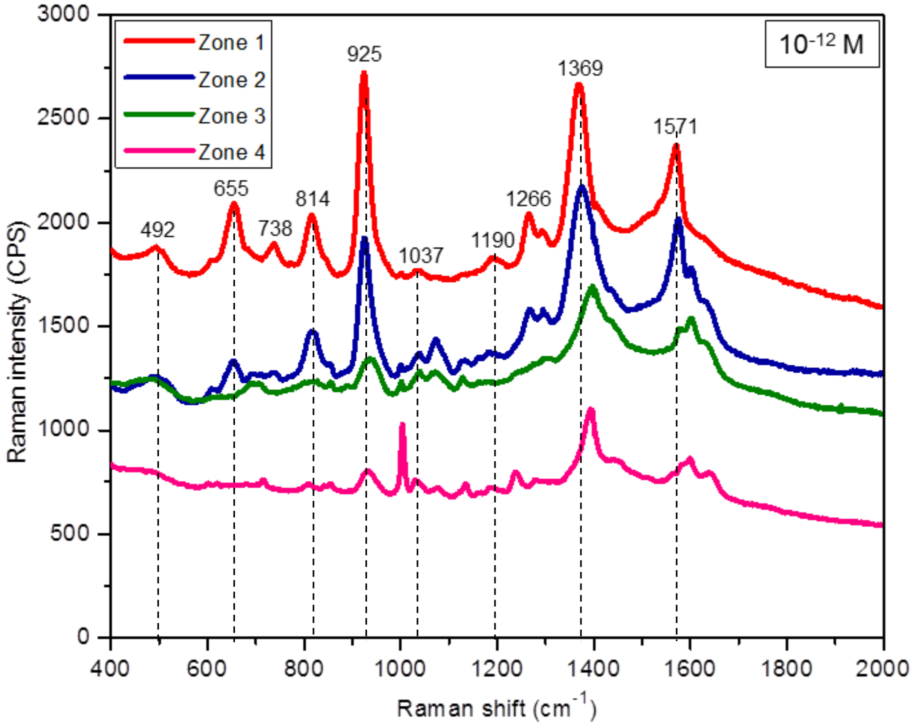
Zone 1
Zone 2
Zone 3
Zone 4
10^{-12} M
492
655
738
814
925
1037
1190
1266
1369
1571
Raman intensity (CPS)
Raman shift (cm^{-1})
0
500
1000
1500
2000
2500
3000
400
600
800
1000
1200
1400
1600
1800
2000

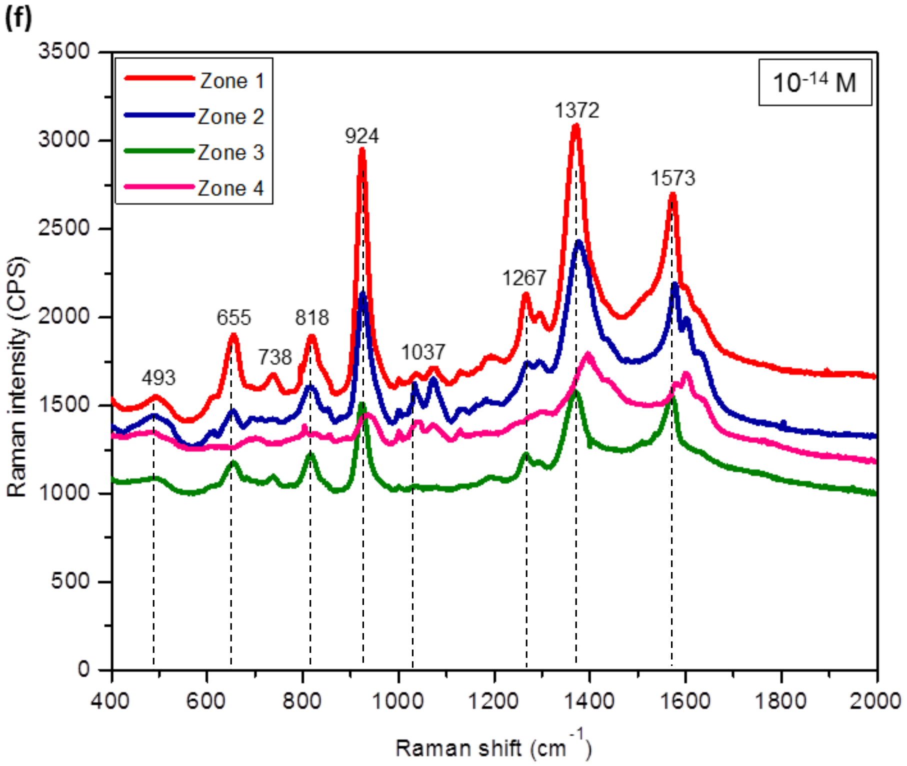

Figure 23 : (a-f) : R6G Spectra for different concentrations and different zones for the substrate

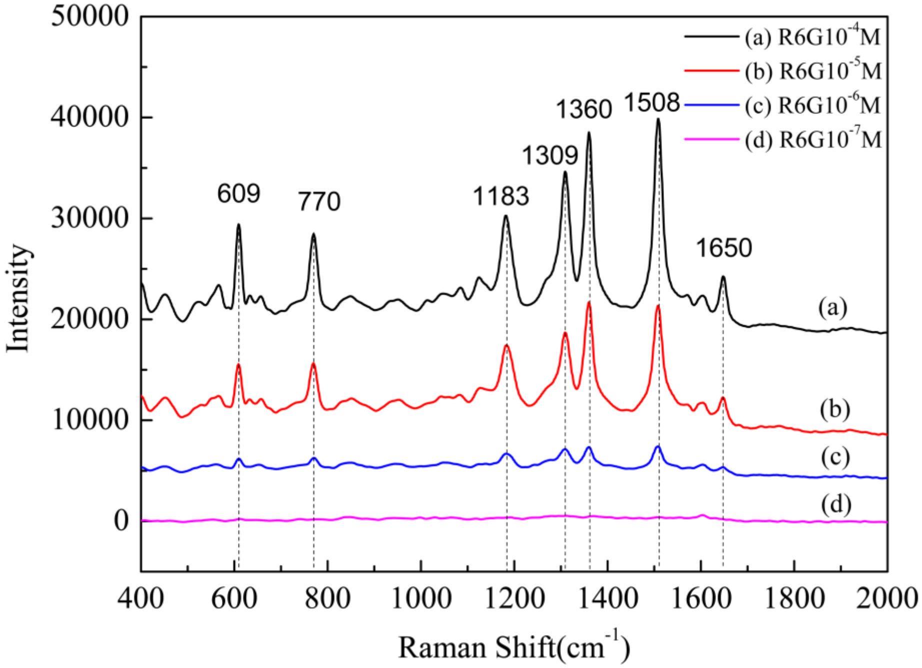

Figure 24 : SERS signal from different concentrations of R6G

Similarly, for further verification and possible application of this substrate, one of the most common over the counter drug Acetaminophen (main constituent of Tylenol) was used with concentrations raging between 0.1 g/L to 0.001 g/L. It can be seen in the Fig. 25 that the Raman Spectra for these concentrations was obtained. Each drug has unique peaks suitable for identification. For acetaminophen this includes the 1168, 1561, and 1648 cm^{-1} phenol, C=C ring, and amide stretches, respectively.

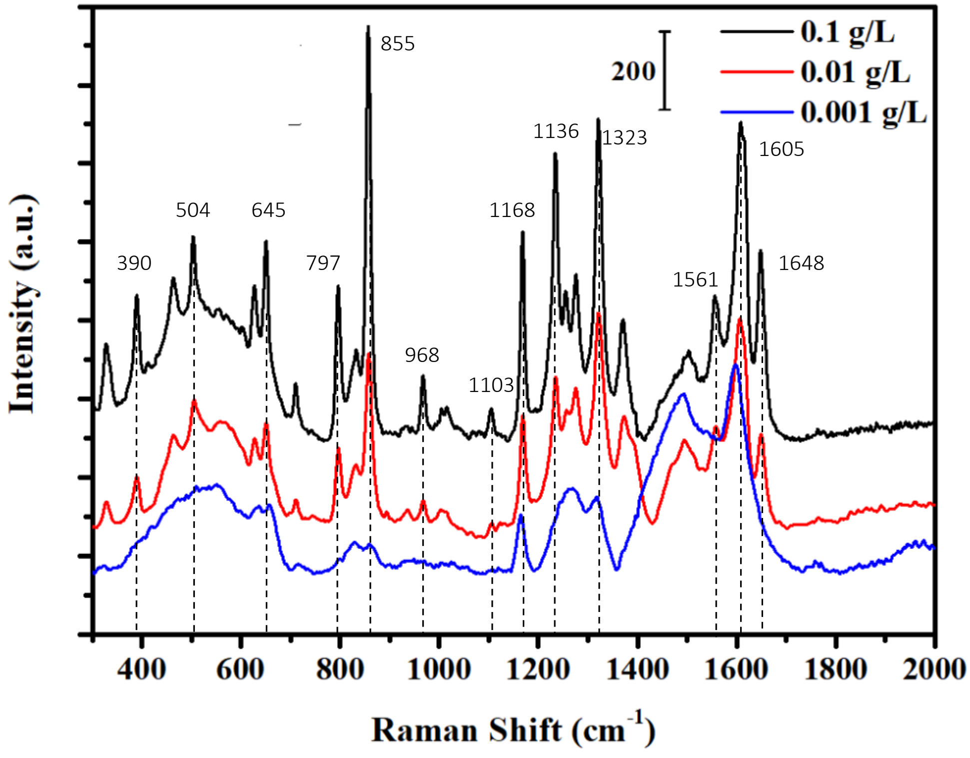

Figure 25 : SERS signal obtained from different concentrations of Acetaminophen

5.2.1 FDTD analysis

Further understanding of the ultra-sensitivity at very low concentration was required. To understand the enhancements and the SERS mechanism behind such high detectability (as low as a couple of hundred molecules), FDTD simulations were conducted on the substrates. FDTD simulation was carried out using the *Lumerical* FDTD software, we constructed 3D and 2D models of silver dendrites similar to the actual dendrites observed under SEM. The dimensions of the dendrites were averaged out to give a better approximation of the electric field enhancements. The simulation was done using a 633 nm LASER as the source and a mesh of 0.25 nm dimensions. The mesh size was chosen according to the computation capability limitation. The observed electrical fields were then processed using a simple MATLAB script that was developed by us to give a final calculated graphical representation of the enhancement factors of the specific case. Fig. 26 shows the different cases that were considered which were similar to the actual observed dendrites. 100 nm diameter dendrites branches were constructed and in study 1 the inter-branch distance or the gaps between the branches were varied from a.) 50nm, b.) 30nm, and c.) 10 nm. It was observed that though there wasn't a substantial difference between the first two cases, the enhancement factors increased with decrease in the gaps. At 10 nm distance the maximum enhancement factor of 6.06 x 10^7 was observed. This can be explained due to the highly localized nanostructure in close vicinity will greatly enhance the electric fields observed in that area. It was also observed that the secondary enhancement came from the tips of the dendrites, this enhancement was lower (10^3 – 10^4) compared to the enhancement observed in the gaps.

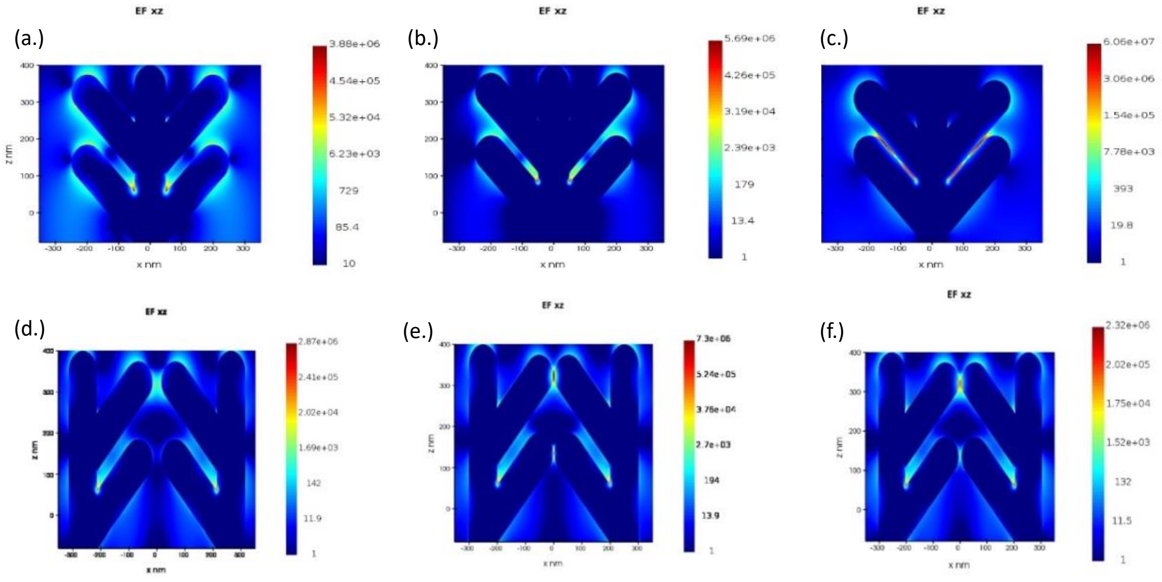

Figure 26 : FDTD simulation results

From the SEM images it was evident that there must also be an interaction between two or more dendrites in the close vicinity, considering this and the enhancement observed on the tips of the dendrites, we suspected that there might be high order of enhancement from these tip-tip interactions. To study and understand the effects of these interactions on the enhancement factors, we simulated another set of structures shown in Fig. 26, in this case the distance between the tips was also changed from d.) 50 nm f.) 30nm, and e.) 10 nm, the observed enhancement factors were of the order of 10^6.

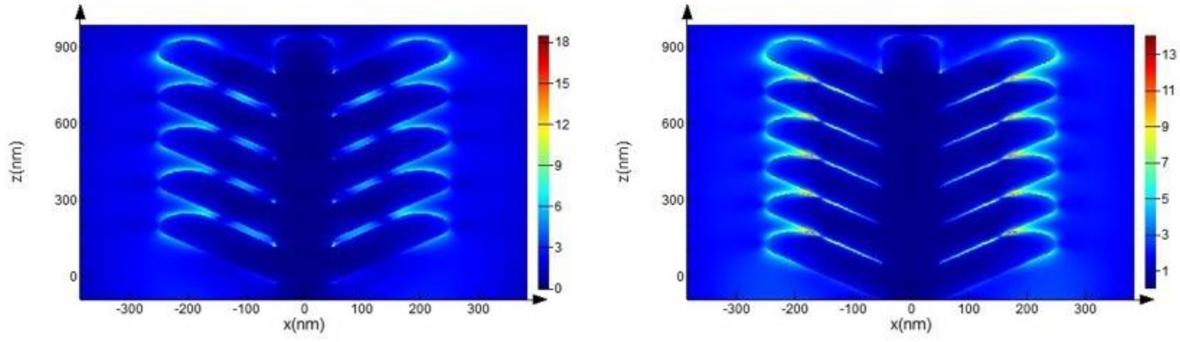

Figure 27 : FDTD simulation results

Fig. 27 shows the electric fields generated around the hotspots considering a full Ag dendrite.

From these studies, it can be seen that the highest EFs of Ag dendrites is in about 6 to7 order of magnitude. With such EFs alone, it is still difficult to explain observed such strong SERS activity from the R6G molecules. We hypothesize that there was some other phenomena at work aiding these results. We had earlier considered that these dendrite substrates with huge surface area should have an inherent filtering and concentration effects that may concentrate molecules between the gaps of the branches. This actually makes these substrates better suited for practical SERS analyzers. As many such in-situ 3D SERS substrates require an intermediate step of concentrating and filtering of the analyte intended for detection, these substrates have this property inherently and make them suitable devices for the in-situ and live monitoring of analytes in liquid medium.

6 Towards an in-situ practical SERS Analyzer : Ag Dendrites Embedded PDMS Channel Device

6.1 Introduction

The work on glass capillary SERS substrate gave us confidence that such substrates can be used as a 3D SERS device. However, the biggest limitation of this device is that no other characterization (particularly SEM) could be conducted on this device without breaking it. Also, the glass would create some photoluminescence which would results in non-uniform and non-reliable results. Thus, we developed a substrate that can accomplish nondestructive SEM characterization and achieve the same sensitivity.

Polydimethylsiloxane (PDMS) was selected to make channels because it has a very good chemical resistance and can be coated with metal very easily. Also, following the latest trend of using 3D printing which has been a very useful and easy technique to fabricate a variety of microstructures, we used 3D printed molds using ABS and PLA. The only limitation with 3D printers available to us was that the smallest feature that could be printed with precision was about 1-2 mm. Because our requirement was 0.5 mm, we attached a glass capillary that we used for previous experiments as the part of the mold. The fabrication and design of the mold is explained in the next section.

6.2 Design and Fabrication

The PDMS Device design was a simple channel of the width 0.5 mm and length 2-3 cm inside a PDMS cast. This was achieved by 3D printing a mold with the required dimensions and then casting commercially

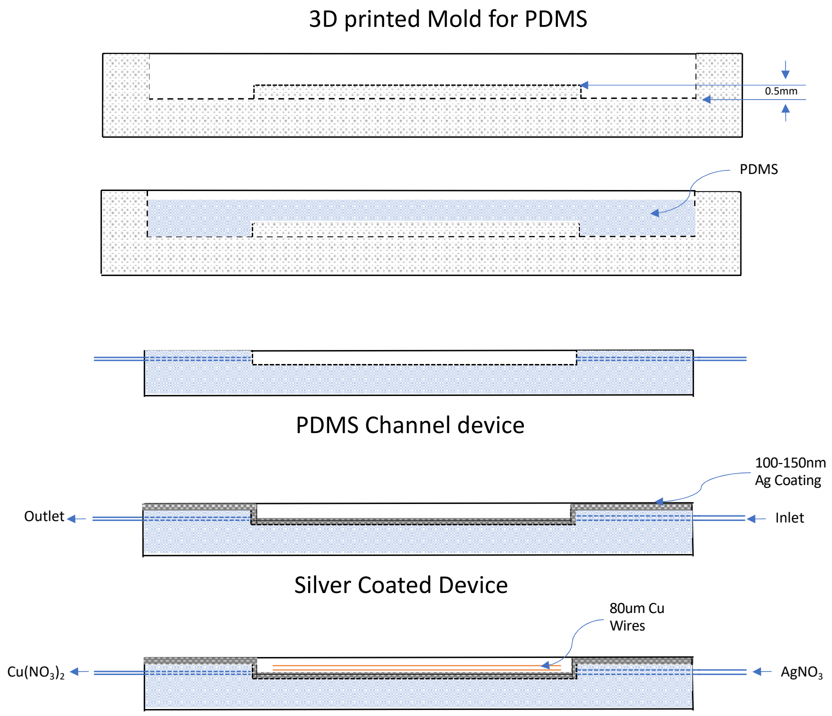

Figure 28 : Schematic of PDMS channeled SERS substrate synthesis

available PDMS inside this mold. As shown in Fig. 28, after the PDMS is cured two pinholes where punched on each side of the device for injecting and flowing the solutions through the device. The diameter of these pinholes was maintained as small as possible prevented the overflow of the solution as well as prevented the flow-out of the dendrites from the other end. Then, it was coated with 100-150nm of Silver, the silver coating was achieved by sputtering using a simple desk-top sputtering machine. Two Cu wires of 80μm diameter each were used as the sacrificial Cu for synthesizing Ag dendrites were placed inside these channels. A glass cover slip was then pressed to the top, 0.1 M $AgNO_3$ was injected in these channels with a flowrate of 0.3ml/min flow rate for 7-8 mins. The dendrites formed inside the channel can be seen in the Fig. 29. DI water was then passed through the channels three times to wash away the chemicals followed by blowing air to dry the device.

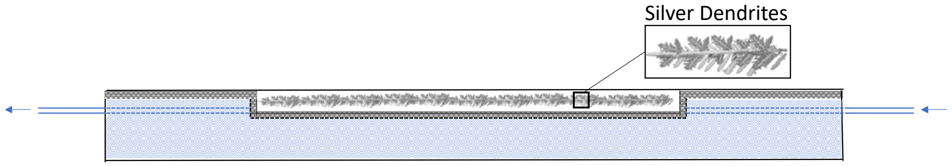

Figure 29 : PDMS Channel SERS substrate with silver dendrites

6.2.1 SEM Results

Fig. 30 and 31 show the SEM micrographs captured using FE-SEM. After removing the top cover slip, the devices were directly loaded into the SEM while connecting the silver on the device to the sample holder using carbon tape. The images show well defined hierarchical multi-branched Ag dendrites with average size of the main trunks between 500 nm to 2 microns. The secondary branches were observed to be around 150-50 nm in diameter. Fig. 30 and Fig. 31 are the two samples made with different flow rates and volumes to synthesize dendrites. In both the cases the average sizes of the dendrites are very similar confirming that that formation of the dendrites could be achieved with a range of flow rates and volumes. In both the cases there are multiple homogeneously distributed dendrites in the length of the channel. It was also observed that multiple dendrites intertangled and interacted closely with each other considerably increasing the hotspot density for excellent SERS enhancements.

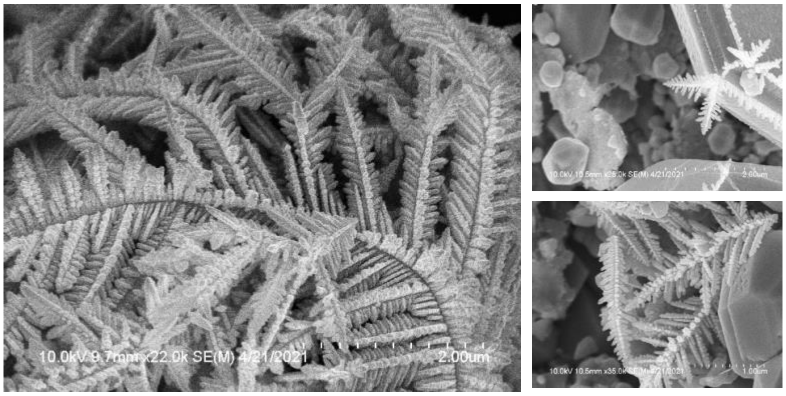

Figure 30 : SEM Micrographs for case 2 : One Cu wire (80 microns) $AgNO_3$ flow rate 0.5 ml/min and volume 3 ml

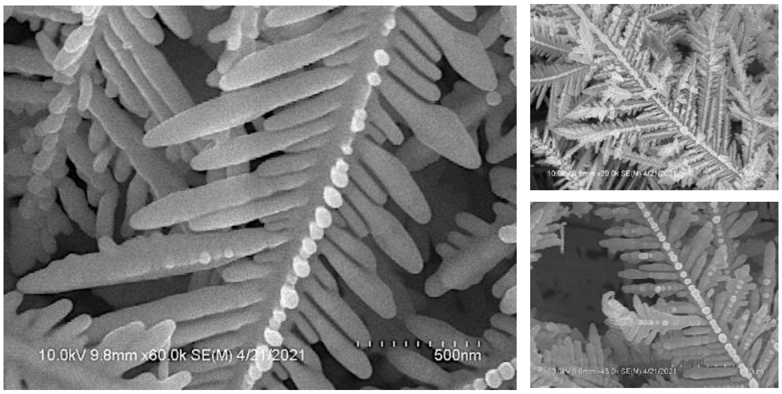

Figure 31 : SEM Micrographs for case 1 : One Cu wire (80 microns) $AgNO_3$ flow rate 0.3 ml/min and volume 1.5 ml

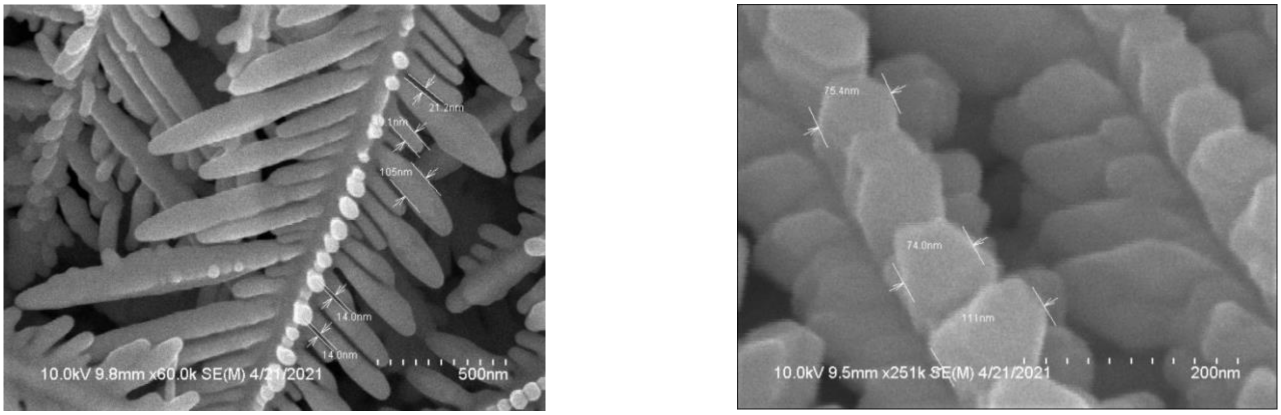

Figure 32 : SEM micrographs with dimensions of the dendrite inside PDMS channel device

Fig. 32 shows the dimension of the observed dendrites in a better labelled view, it can be clearly seen that at maximum the diameter of the secondary branches is around 160 nm and at minimum it is around 50 nm. The inter-branch gaps range from 10-20 nm, which according to the previous FDTD simulation results should have the highest enhancement factors. It can also be observed from the Fig. 32 (right) that there are some homogeneously distributed 75 nm particles attached to the z-direction of the dendrite flake, these small particles should also contribute to the increased roughness and are excellent spots for the enhanced electric fields that can be translated to an extremely efficient SERS enhancement.

These SEM images confirm that well defined Ag dendrites achieved in the glass capillaries can be repeated in the PDMS channel devices. With making the three walled devices, the quality, size and the morphology of Ag dendrites can be verified and confirmed without destroying the devices. This is very useful in establishing the quality of the analyzer before-hand; making it a possibility to quality check each and every device prior to SERS measurement.

6.2.2 SERS Results

SERS measurement was performed on the substrates by adding different molecules dissolved at different concentrations in solutions. To quantify the enhancement effect, the injected analyte volume was only enough to fill the channels, minimizing the number of molecules introduced into the substrate. We detected different concentration of R6G. The results were similar to the experiments with glass capillaries as discussed earlier. Experiments with R6G proved that it was possible to detect very low concentrations in liquid using this device. Also, other commonly used SERS molecules were tested, showing that the label free detection was not limited to R6G molecules; the enhancement in signal from multiple different molecules was indeed achieved. Other molecules detected include Methylene Blue, 4-Methoxy Benzoic Acid and Thiabendazole dissolved in suitable solvents.

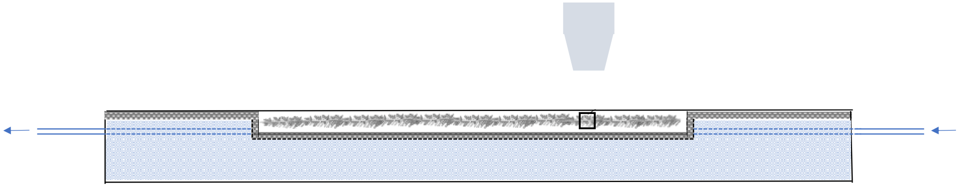

Figure 33 : Schematic diagram of SERS detection inside PDMS Substrate

6.2.2.1 Rhodamine 6G

The SERS results for R6G solutions at different concentrations inside the PDMS channels with dendrites is shown in Fig. 34. Spectra obtained for 10^{-8} – 10^{-14} M R6G showed characteristic Raman peaks 610 cm^{-1},

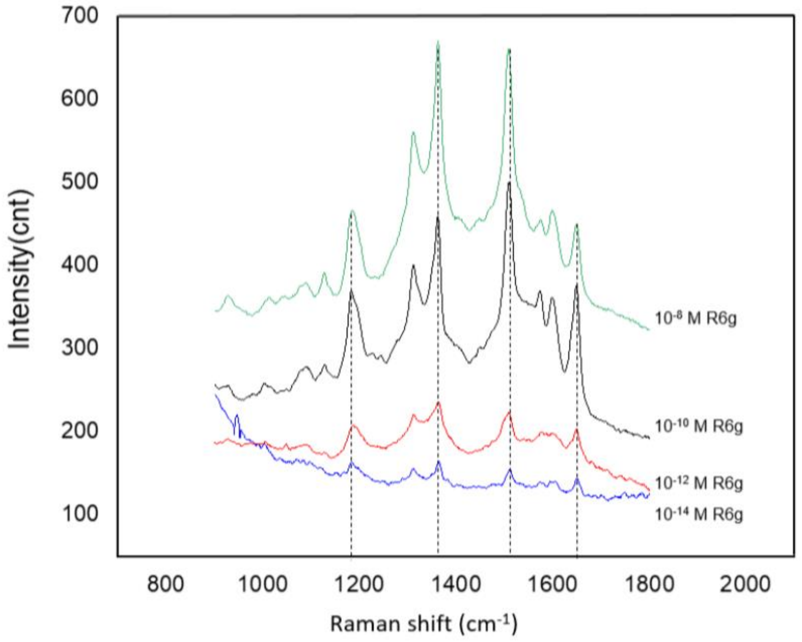

Figure 34 : SERS results for different concentrations of R6G inside PDMS channel device

767 cm^{-1}, 1184 cm^{-1}, 1360 cm^{-1}, 1510 cm^{-1}, 1570 cm^{-1}, and 1651 cm^{-1} which correspond to C-C-C ring in-plane, C-H out of plane bending, C-H in-plane bending vibrations, C-O-C stretching and C-C stretching of ring. It was observed that the intensity drops with decrease of concentration, but even at ultra-low concentrations of 10^{-14} M the peaks are clearly visible. This proves that without flowing and concentrating, the lower limit of detection for the substrates is at least 10^{-14} M. The permissible volume inside the channels, after subtracting the volume of the dendrites, is around 2.5 µl which translates to approximately 10,000 molecules inside the channel. Considering the small volume of the laser spot of the Raman microscope and spectrometer the number of molecules in the detection volume at any instance of detection comes to around 20-30 molecules.

6.2.2.2 Other Molecules in solution

Establishing the substrate as a versatile label free SERS device was one of the important goals of this study and for that, it was important to verify that the sensitive detectability of the substrate was not just limited to one molecule. For this study we tested some commonly used SERS molecules that have been used for proving the SERS activities of various substrates.

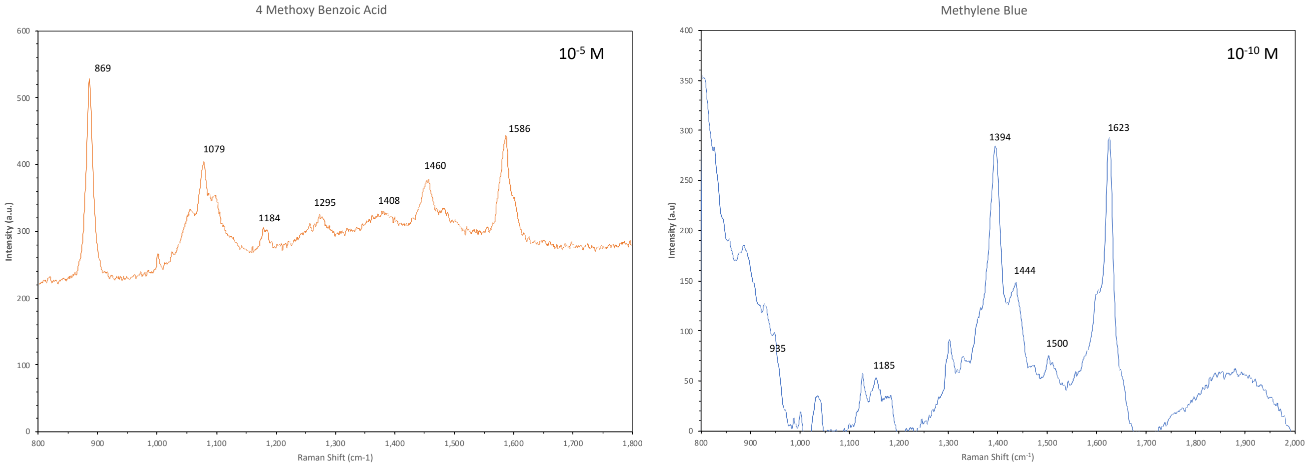

Figure 35 : SERS Results in PDMS device for a. 4-methoxy benzoic acid b. Methylene Blue

Two molecules with very different structures were considered, Methylene Blue dissolved in DI water and 4 Methoxy benzoic acid dissolved in methanol. The results for both are shown in Fig. 35, it can be seen that in both these cases we were able to detect considerably low concentrations of 10^{-10} M and 10^{-5} M respectively.

6.3 Calibration with R6G

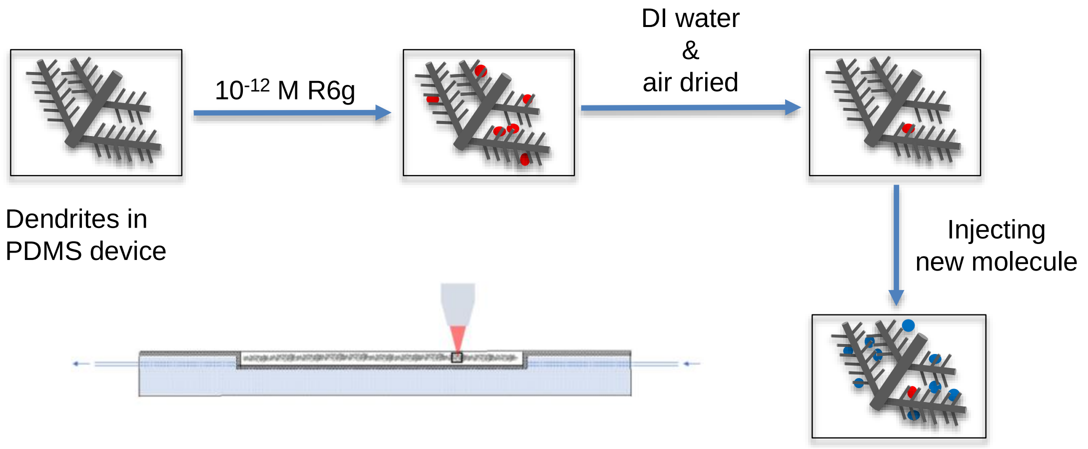

Figure 36 : Calibration of SERS device with Rhodamine 6G (R6G)

One of the biggest concerns with developing SERS substrates has been the possibility of calibrating and verifying the SERS activity of the substrates for further application as reliable analyzers for practical devices. This has been long standing issue that has limited the real-world use of SERS as a reliable detection technique, which it surely has a potential to be.

Here, since we were able to detect ultra-low concentrations of R6G with our device, we explored the possibility using R6G as a calibrating molecule to calibrate the device for the detection of other molecules. 10^{-12} M concentrations of R6G were used on each device to locate hotspots and to confirm the SERS activity of that specific device. As shown in Fig. 36, the as prepared Ag dendrites inside the device were introduced to 10^{-12} M R6G solution and then detection was done using a Raman spectrometer, typical results for this are shown in Fig. 37. Later the device was

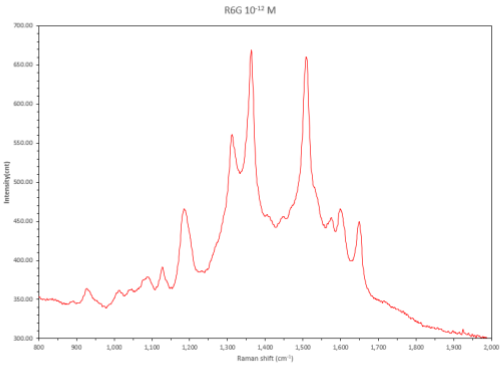

Figure 37 : Typical R6G signal for 10^{-12} M R6G for calibration of device

cleaned by flowing 5-10 ml of DI water inside the channels, and then the substrates are dried by passing air at a very low pressure as to not break the dendrites. After this the analyte solution can be injected inside the channels for detection.

The advantages of this method of calibration are extremely important to develop a label free reliable and reproducible practical SERS analyzer. R6G is a model molecule for SERS, it has many prominent and distinct peaks that can be confirmed and verified. Hotspots and their location can be found and confirmed using this technique . Also, defective devices can be marked and discarded or re-fabricated, which removes the possibility of unreliable results and false negatives or false positives due to non-conforming devices. A standard can be established for devices, that can aid into dependable and reproducible results.

We were able to confirm this calibration with R6G and the used the same devices to detect other molecules in the same channels. Also, no R6G signal was observed after cleaning of the substrates. The results for the detection of molecules in the calibrated device are discussed in section 6.5.

6.4 Multi-channel devices

In continuation to our efforts for making this device a practical device, we fabricated multi-channel devices. Multi-channel devices can be connected to the flow in any practical application and can be useful for detecting the same molecule multiple times giving out multiple results that can be processed for a more accurate measurement of analytes.

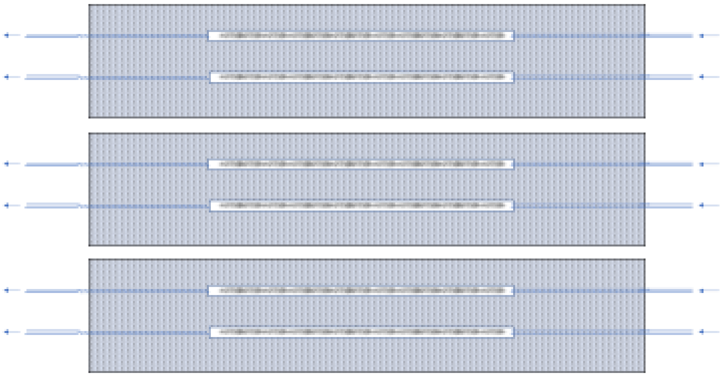

Figure 38 : Multichannel device

These multi-channels can also be used to detect different molecules in each channel, if needed different labels can also be added that can trap specific biological or chemical species that required certain labels for their precise capture and detection.

Figure 39 : Schematic for using device in in-situ detection and real time monitoring in a liquid flow

A schematic of these multi-channels connected in parallel is shown in Fig. 38, with a representation of how the devices in general can be connected to a liquid flow for in-situ detection and real-time monitoring of analytes of importance (Fig. 39).

6.5 Application as an in-situ SERS detection for Thiabendazole (TBZ)

The thiabendazole (TBZ) is a systemic fungicide that belongs to the benzimidazole compounds. It is commonly used in pre- and post-harvest in several crops, mainly to prevent mold caused during the transportation of the crop. Also, it has pharmacological properties as to control helminth in animal species[229]. Although TBZ is classified as low toxicity to humans, it is very toxic to aquatic environment. According to the United States Environmental Protection Agency (USEPA) [230], TBZ is the most found pesticide in apple in United States and the Maximum Residue Level (MRL) tolerated is 5 ppm[231]. According to European Union legislation, the MRL in raw fruits and vegetables has been established in the range of 0.05–15 ppm. TBZ is associated with a host of adverse effects including nephrotoxicity, hepatotoxicity, carcinogenicity, and teratogenicity, classified by U.S. Environmental Protection Agency (EPA) as likely to be carcinogenic at doses high enough to cause disturbance of the thyroid hormone balance.

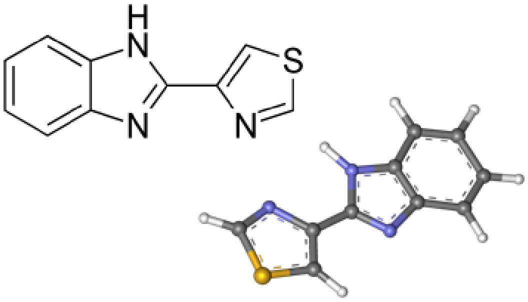

Figure 40 : Thiabendazole

SERS results for TBZ are shown in Fig. 41-43, the detection was carried out in R6G calibrated devices. It can be clearly seen that no residual signal from R6G is visible. Different concentrations of TBZ were prepared by dissolving Power TBZ in Methanol.

We started with a considerably high concentration of 5ppm and after detecting it with very good precision moved to lower concentration to check the lower limit of detection for TBZ. We were able to reach a 0.5 ppm detection limit (Fig. 43). From the obtained signals and results we think that even lower concentrations can be reached and detected, this can be a continued study. Pertaining to the time constraint and considering the range of allowed TBZ concentrations as mentioned in the above section it seems that these substrates can easily be applied for live detection and monitoring of TBZ in real-world applications. These substrates can provide a precise detection inside multiple sources of TBZ contamination in flowing liquid media and provide a real-time monitoring of a possible contamination as a part of quality checks and quality control.

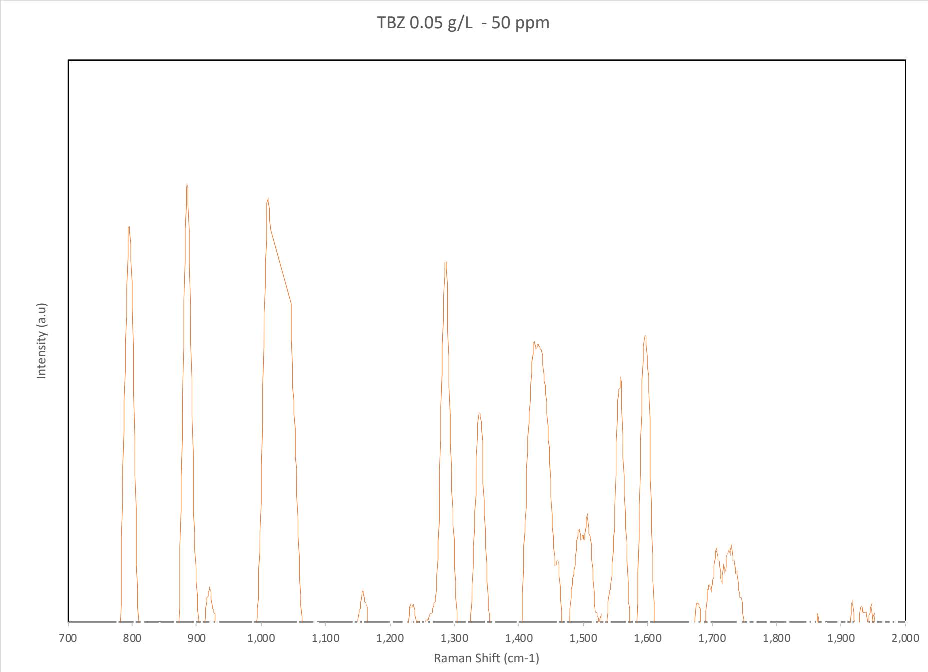

Figure 41 : SERS Results for Thiabendazole (TBZ) at 50 ppm concentration in methanol

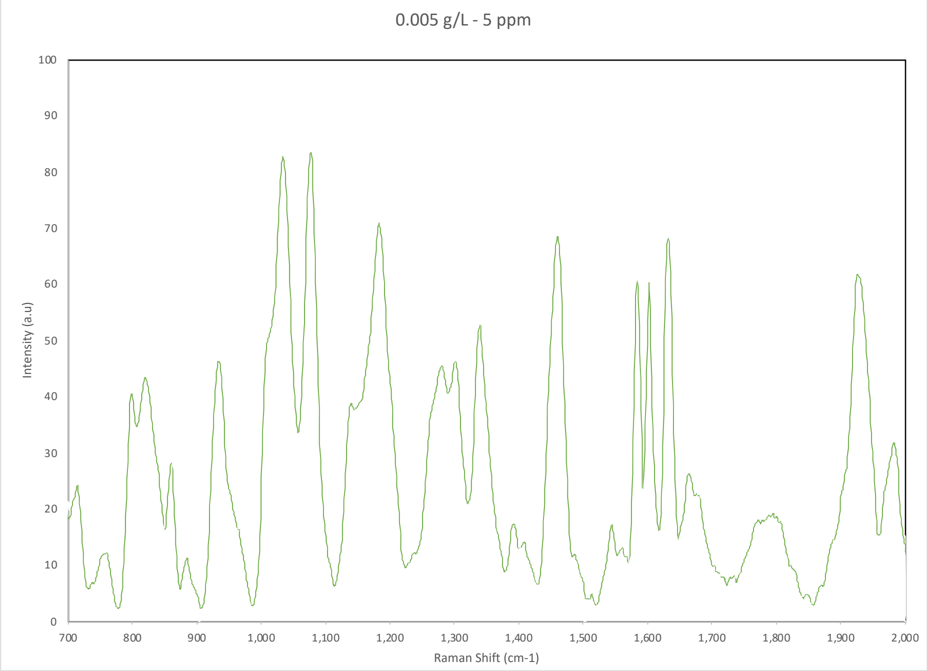

Figure 42 : SERS Results for Thiabendazole (TBZ) at 5 ppm concentration in methanol

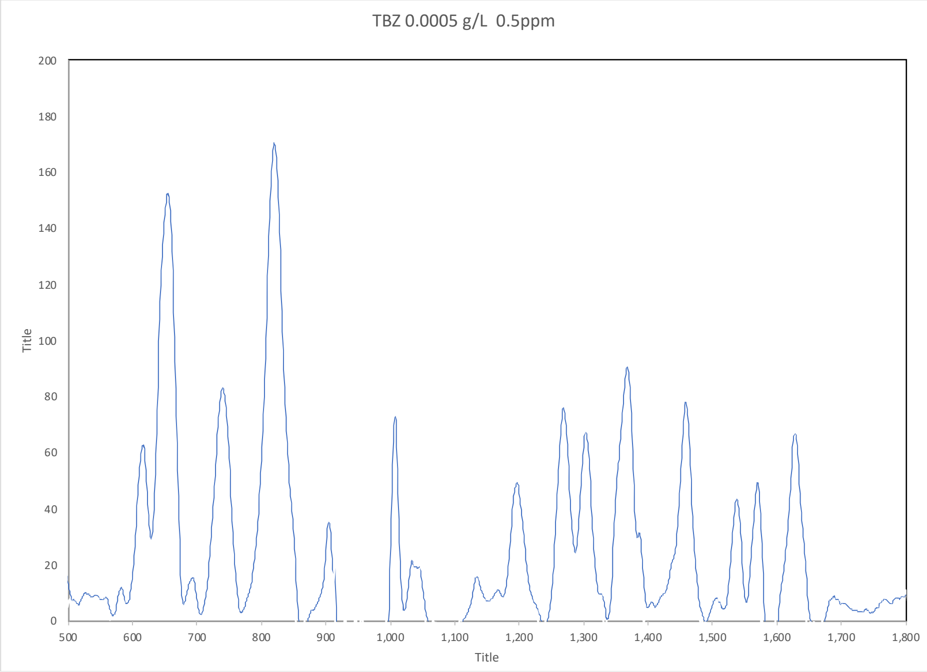

Figure 43 : SERS Results for Thiabendazole (TBZ) at 0.5 ppm concentration in methanol

Different peaks were observed clearly at 778, 882, 897, 983, 1006, 1276, 1456, 1573, 1593 and 1623 cm−1 on the SERS spectra of TBZ. The strong peaks at 778, 882, 897 and 1006 cm^{-1} were related to the bending of C-H out of the plane of TBZ molecule, the adjacent peaks at 1456, 1573, 1593 and 1623 cm^{-1} were resulted from the stretching of C=N, the peak at 983 cm^{-1} was caused by the stretching of C-S, and the stretching of the totally ring attributed to the peaks at 1276 and 1573 cm^{-1}. Very Strong 1030 cm^{-1} was observed due to the presence of methanol in the solution, this peak was subtracted for a better representation of comparatively weaker TBZ peaks.

7 Conclusion

Using the simple galvanic reaction between Cu and $AgNO_3$, a new synthesis process for the preparation of highly branched, single-crystal silver dendrites on the top surface and inside the nanochannels of Cu-coated AAO membranes was systematically studied. The AAO membranes separated the reactant Cu layer and the product metal Ag, generating completely free-standing, pure, and clean Ag dendrites at room temperature within a few minutes. It was concluded that Ag^+ ions in $AgNO_3$ solution were not directly reduced by Cu. Rather, nitrate (NO_3^-) ions first get reduced to nitrite ions (NO_2^-), and in turn NO_2^-ions reduce Ag^+ to Ag. This reaction mechanism allows Ag dendrites to grow freely on the surface of an AAO membrane, while in the interior of the membrane the growth of the Ag dendrites was retarded by the spatial restrictions. A series of time-dependent experiments revealed that the synthesis of Ag dendrites starts with the formation of very small nanoparticles, which subsequently get together to create nanoclusters. The growth of the nanoclusters proceeds by Ostwald ripening and oriented attachment.

Using this reaction, we fabricated a novel, low-cost, highly sensitive Ag nanostructure-based surface enhanced Raman scattering (SERS) substrate inside the glass capillaries. We found that the presence of dendrites is essential to obtain the enhancement of the Raman signal. Using this 3D SERS substrate, ultra-sensitive in-situ detection of molecules in liquid media was achieved. The detection limit for Rhodamine 6G dye molecules in liquid medium (DI water) reaches to 10^{-14}M. To our knowledge, this is the lowest concentration detected in liquid media without drying or concentrating the sample by continuous flow. FDTD simulations were preformed to illustrate the electric field enhancement in Ag dendrites when they are irradiated with a laser light. It shows a large number of hot spots present in the gaps and tips of the branches in Ag dendrites. The further detection of 0.001 g/L Acetaminophen proved that the ultra-low concentration detection is not limited only to R6G and thus showed the possible applicability of such substrate in different fields of study including drug detection.

Also, we were able to synthesize a practical SERS analyzer using Ag dendrite embedded PDMS channels that can be used for in-situ detection and monitoring of a wide range of molecules in flowing liquid media. More importantly, we established a calibrating method using R6G for such devices, ensuring a reliable detection. In addition, using this simple fabrication process, multi-channel configuration can be easily adopted, which makes it possible to conduct multiple measurements for better averaged-out SERS results. (Reducing noise and removal of non-conforming or external peaks caused due to some anomalies in detection). Practical application of this device was tested with detection of Thiabendazole molecules in R6G-calibrated devices, confirming the presence of high number of hotspots and prospect of detecting these spots beforehand with R6G for reliable and reproducible SERS signals.

8 References

[1] Coluccio, M. L.; Das, G.; Mecarini, F.; Gentile, F.; Pujia, A.; Bava, L.; Tallerico, R.; Candeloro, P.; Liberale, C.; De Angelis, F.; Di Fabrizio, E. Silver-based surface enhanced Raman scattering (SERS) substrate fabrication using nanolithography and site selective electroless deposition. Microelectron. Eng. 2009, 86, 1085-1088.

[2] Vendamani, V.S.; Nageswara Rao, S. V. S.; Venugopal Rao, S.; Kanjilal, D.; Pathak, A. P. Three-dimensional hybrid silicon nanostructures for surface enhanced Raman spectroscopy based molecular detection. J. Appl. Phys. 2018, 123 (014301), 1-8.

[3] Fleischmann, M.; Hendra,P. J.; McQuillan, A. J. Raman spectra of pyridine adsorbed at a silver electrode. Chem. Phys. Lett. 1974, 26, 163-166.

[4] Kneipp, K.; Kneipp, H.; Itzkan, I.; Dasari, R. R.; Feld, M. S. Surface-enhanced Raman scattering and biophysics. J. Phys-Condens. Mat. 2002, 14, R597-R624.

[5] Wang, X. T.; Shi, W. S.; She, G. W.; Mu, L. X.; Lee, S. T. High-performance surface enhanced Raman scattering sensors based on Ag nanoparticles-coated Si nanowire arrays for quantitative detection of pesticides. Appl. Phys. Lett. 2010, 96 (053104), 1-3.

[6] Metiu, H.; in: Chang, R. K.; Furtak, T. E.; (Eds.). Surface enhanced Raman scattering. Plenum Press, New York, USA, 1982.

[7] Aroca, R. Surface-enhanced vibrational spectroscopy. John Wiley & Sons, Ltd, Chichester, England, 2006.

[8] Tourrel, G.; Corset, J. Raman microscopy: developments and applications. Elsevier Academic Press, Cambridge, USA, 1996.

[9] De Angelis, F.; Patrini, M.; Das, G.; Maksymov, I.; Galli, M.; Businaro, L.; Andeani, L. C.; Di Fabrizio, E. A hybrid plasmonic-photonic nanodevice for label-free detection of a few molecules. Nano Lett. 2008, 8 (8), 2321–2327.

[10] Sharma, B.; Frontiera, R. R.; Henry, A. I.; Ringe, E.; Van Duyne, R. P. SERS: materials, applications, and the future. Mater. Today. 2012, 15, 16–25.

[11] Kleinman, S. L.; Frontiera, R. R.; Henry, A. I.; Dieringer, J. A.; Van Duyne, R. P. Creating, characterizing, and controlling chemistry with SERS hot spots. Phys. Chem. Chem. Phys. 2013, 15, 21–36.

[12] Yilmaz, M.; Erkartal, M.; Ozdemir, M.; Sen, U.; Usta, H.; Demirel, G. Three-dimensional Au-coated electrosprayed nanostructured BODIPY films on aluminum foil as surface-enhanced Raman scattering platforms and their catalytic applications. ACS Appl. Mater. Inter. 2017, 9, 18199−18206.

[13] Cai, W. F.; Pu, K. B.; Ma, Q.; Wang, Y. H. Insight into the fabrication and perspective of dendritic Ag nanostructures. J. Exp. Nanosci. 2017, 12 (1), 319-337.

[14] Yang, Y.; Matsubara, S.; Xiong, L.; Hayakawa, T.; Nogami, M. Solvothermal synthesis of multiple shapes of silver nanoparticles and their SERS properties. J. Phys. Chem. C. 2007, 111 (26), 9095-9104.

[15] Nekahi, A.; Marashi, S. P. H.; Fatmesari, D. H. High yield polyol synthesis of round-and sharpened silver nanowires with high aspect ratio. Mater. Chem. Phys. 2016, 184, 130–137.

[16] Wang, W.; Zhong, Y.; Li, D.; Wang, P.; Cai, Y.; Duan, Z. Thermal behavior of Ag micro/nano wires formed by low temperature sintering of Ag nanoparticles. J. Electron. Mater. 2015, 44, 4920–4927.

[17] Luo, M.; Huang, H.; Choi, S.; Zhang, C.; da Dilva, R. R.; Peng, H. C.; Li, Z. Y.; Liu, J.; He, Z.; Xia, Y. Facile synthesis of Ag nanorods with no plasmon resonance peak in the visible region by using Pd decahedra of 16 nm in size as seeds. ACS Nano. 2015, 9, 10523–10532.

[18] De, R.; Shin, Y. S.; Lee, C. L.; Oh, M. K. Long-standing stability of silver nanorod array substrates functionalized using a series of thiols for a SERS-based sensing application. Appl. Spectrosc. 2016, 70, 1137–1149.

[19] Chen, Z.; Zhang, C.; Wu, Q.; Li, K.; Tan, L. Application of triangular silver nanoplates for colorimetric detection of H_2O_2. Sensor. Actuat. B-Chem. 2015, 220, 314–317.

[20] Zhou, S.; Li, J.; Gilroy, K. D.; Tao, J.; Zhu, C.; Yang, X.; Sun, X.; Xia, Y. Facile synthesis of silver nanocubes with sharp corners and edges in an aqueous solution. ACS Nano. 2016, 10, 9861–9870.

[21] Personick, M. L.; Langille, M. R.; Zhang, J.; Wu, J.; Li, S.; Mirkin, C.A. Plasmon-mediated synthesis of silver cubes with unusual twinning structures using short wavelength excitation. Small. 2013, 9, 1947–1953.

[22] Tsai, K. W.; Sivashanmugan, K.; Lin, C. H.; Tsai, P. J.; Cheng, S. C.; Lan, Y. C.; Chen, T. Y.; Wen, T. C. The size effect of silver nanocubes on gap-mode surface enhanced Raman scattering substrate. J. Taiwan. Inst. Chem. E. 2016, 69, 146–150.

[23] Gu, C.; Zhang, T. Electrochemical synthesis of silver polyhedrons and dendritic films with superhydrophobic surfaces. Langmuir. 2008, 24, 12010–12016.

[24] Borges, J.; Rodrigues, M. S.; Lopes, C.; Costa, D.; Ferreira, A.; Pereira, R. M. S.; Costa, M. F.; Vasilevskiy, M. I.; Vaz, F. Ag fractals formed on top of a porous TiO_2 thin film. Phys. Status Solidi. 2016, 10, 530–534.

[25] O'Regan, C.; Zhu, X.; Zhong, J.; Anand, U.; Lu, J.; Su, H.; Mirsaidov, U. CTAB-influenced electrochemical dissolution of silver dendrites. Langmuir. 2016, 32, 3601–3607.

[26] Gu, C. D.; Cheng, C.; Huang, H.; Wong, T.; Wang, N.; Zhang, T. Y. Growth and photocatalytic activity of dendrite-like ZnO@Ag heterostructure nanocrystals. Cryst. Growth Des. 2009, 9 (7), 3278–3285.

[27] Lu, L. H.; Kobayashi, A.; Kikkawa, Y.; Tawa, K.; Ozaki, Y. Oriented attachment-based assembly of dendritic silver nanostructures at room temperature. J. Phys. Chem. B. 2006, 110, 23234–23241.

[28] Zhang, C. X.; Su, L.; Chan, Y. F.; Wu, Z. L.; Zhao, Y. M.; Xu, H. J.; Sun, X. M. Ag@SiO2 core-shell nanoparticles on silicon nanowire arrays as ultrasensitive and ultrastable substrates for surface-enhanced Raman scattering. Nanotechnology. 2013, 24 (33), 335501–335509.

[29] Bu, Y.; Lee, S. Influence of dopamine concentration and surface coverage of Au shell on the optical properties of Au, Ag, and Ag(core)Au(shell) nanoparticles. ACS. Appl. Mater. Inter. 2012, 4 (8), 3923–3931.

[30] Yin, H. J.; Chen, Z. Y.; Zhao, Y. M.; Lv, M. Y.; Shi, C. A.; Wu, Z. L.; Zhang, X.; Liu, L.; Wang, M. L.; Xu, H. J. Ag@Au core-shell dendrites: a stable, reusable and sensitive surface enhanced Raman scattering substrate. Sci. Rep. 2015, 5 (14502), 1-9.

[31] Gu, C.; Zhang, T. Y. Electrochemical synthesis of silver polyhedrons and dendritic films with superhydrophobic surfaces. Langmuir. 2008, 24, 12010-12016.

[32] Zhou, Q.; Wang, S.; Jia, N.; Liu, L.; Yang, J.; Jiang, Z. Synthesis of highly crystalline silver dendrites microscale nanostructures by electrodeposition. Mater. Lett. 2006, 60, 3789‑3792.

[33] Maksimovic, V. M.; Pavlovic, M. G.; Pavlovic, Lj. J.; Tomic, M. V.; Jovic, V. D. Morphology and growth of electrodeposited silver powder particle. Hydrometallurgy. 2007, 86, 22‑26.

[34] Qian, L.; Yang, X. Dendrimers as “controllers” for modulation of electrodeposited silver nanostructures. Colloid. Surface. A. 2008, 317, 528‑534.

[35] Agrawal, V. V.; Kulkarni, G. U.; Rao, C. N. R. Surfactant-promoted formation of fractal and dendritic nanostructures of gold and silver at the organic-aqueous interface. J. Colloid. Interf. Sci. 2008, 318, 501–506.

[36] Zheng, X. W.; Zhu, L. Y.; Wang, X. J.; Yan, A. H.; Xie, Y. A simple mixed surfactant route for the preparation of noble metal dendrites. J. Cryst. Growth. 2004, 260, 255–262.

[37] Wang, Z.; Tao, F.; Chen, D.; Yao, L.; Cai, W.; Li, X. Self-assembled silver dendritic nanostructure on the surface of AAO template. Chem. Lett. 2007, 36 (5), 672-673.

[38] Zhou, Y.; Yu, S. H.; Wang, C. Y.; Li, X. G.; Zhu, Y. R.; Chen, Z. Y. A novel ultraviolet irradiation photo-reduction technique for preparation of single crystal Ag nanorods and Ag dendrites. Adv. Mater. 1999, 11, 850–852.

[39] Xiao, J.; Xie, Y.; Tang, R.; Chen, M.; Tian, X. Novel ultrasonically assisted template synthesis of palladium and silver dendritic nanostructures. Adv. Mater. 2001, 13, 1887–1891.

[40] Wang, Z.; Zhao, Z.; Qiu, J. A general strategy for synthesis of silver dendrites by galvanic displacement under hydrothermal conditions. J. Phys. Chem. Solids. 2008, 69, 1296–1300.

[41] Shizhong, W.; Houwen, X. Fractal and dendritic growth of metallic Ag aggregated from different kinds of γ-Irradiated solutions. J. Phys. Chem. B. 2000, 104, 5681-5685.

[42] Socol, Y.; Abramson, O.; Gedanken, A.; Meshorer, Y.; Berenstein, L.; Zaban, A. Suspensive electrode formation in pulsed sonoelectrochemical synthesis of silver nanoparticles. Langmuir. 2002, 18, 4736-4740.

[43] Song, W.; Cheng, Y.; Jia, H.; Xu, W.; Zhao, B. Surface enhanced Raman scattering based on silver dendrites substrate. J. Colloid. Interf. Sci. 2006, 298, 765–768.

[44] Xie, S.; Zhang, X.; Xiao, D.; Paau, M. C.; Huang, J.; Choi, M. M. F. Fast growth synthesis of silver dendrite crystals assisted by sulfate ion and its application for surface-enhanced Raman scattering. J. Phys. Chem. C. 2011, 115, 9943-9951.

[45] Ye, W.; Chen, Y.; Zhou, F.; Wanga, C.; Li, Y. Fluoride-assisted galvanic replacement synthesis of Ag and Au dendrites on aluminum foil with enhanced SERS and catalytic activities. J. Mater. Chem. 2012, 22, 18327-18334.

[46] Fang, J.; Ding, B.; Song, X. Self-assembly ability of building units in mesocrystal, structural, and morphological transitions in Ag nanostructures growth. Crsyt. Growth Des. 2008, 8 (10), 3616-3622.

[47] Nersisyan, H. H.; Lee, Y. J.; Joo, S. H.; Han, S. K.; Lee, T. H.; Lee, J. S.; An, Y. S.; Lee, J. H. Iron-assisted electroless deposition reaction for synthesizing copper and silver dendritic structures. Cryst. Eng. Comm. 2015, 17, 7535-7542.

[48] Wang, X. In situ fabrication of novel Ag dendrites film by a simple replacement reaction on Zn foil substrate. Syn. React. Inorg. M. 2016, 46, 1579-1583

[49] Fang, J.; You, H.; Kong, P.; Yi, Y.; Song, X.; Ding, B. Dendritic silver nanostructure growth and evolution in replacement reaction. Cryst. Growth Des. 2007, 7 (5), 864-867.

[50] Gutes, A.; Carraro, C.; Maboudian, R. Silver dendrites from galvanic displacement on commercial aluminum foil as an effective SERS substrate. J. Am. Chem. Soc. 2010, 132 (5), 1476–1477.

[51] Ye, W.; Chen, Y.; Zhou, F.; Wanga, C.; Li, Y. Fluoride-assisted galvanic replacement synthesis of Ag and Au dendrites on aluminum foil with enhanced SERS and catalytic activities. J. Mater. Chem. 2012, 22, 18327-18334.

[52] Cheng, W. M.; Wang, C. C.; Chen, C. Y. The influence of Ni nanoparticles and Ni (II) on the growth of Ag dendrites immobilized on the chelating copolymer membrane. Mater. Chem. Phys. 2012, 137, 76-84.

[53] Cheng, W. M.; Wang, C. C.; Chen, C. Y. Preparing chelated copolymer membrane for fabrication of Ag dendrites. J. Colloid Interf. Sci. 2010, 348, 49-56.

[54] Zhang, G.; Sun, S.; Norouzi Banis, M.; Li, R.; Cai, M.; Sun, X. Morphology-controlled green synthesis of single crystalline silver dendrites, dendritic flowers, and rods, and their growth mechanism. Cryst. Growth Des. 2011, 11, 2493-2499.

[55] Xu, H.; Shao, M.; Chen, T.; Zhaoa, Y.; Leeb, S. T. Surface-enhanced Raman scattering on silver dendrite with different growth directions. J. Raman Spectrosc. 2012, 43, 396-404.

[56] Chen, L.; Zhang, Z.; Chen, G.; Lai, C.; Zhou, H. Synthesis of silver particles on copper substrates using ethanol-based solution for surface enhanced Raman spectroscopy. AIP Adv. 2014, 4 (31324), 1-8.

[57] Zhang, X.; Ji, R.; Wang, L.; Yu, L.; Wang, J.; Gengab, B.; Wang, G. Controllable synthesis of silver nanodendrites on copper rod and its application to hydrogen peroxide and glucose detection. Cryst. Eng. Comm. 2013, 15, 1173-1178.

[58] Avizienis, A. V.; Martin-Olmos, C.; Sillin, H. O.; Aono, M.; Gimzewski, J. K.; Stieg, A. Z. Morphological transitions from dendrites to nanowires in the electroless deposition of silver. Cryst. Growth Des. 2013, 13, 465-469.

[59] Dinga, H. P.; Xina, G. Q.; Chena, K.C.; Zhanga, M.; Liub, Q.; Haoa, J.; Liua, H. G. Silver dendritic nanostructures formed at the solid/liquid interface via electroless deposition. Colloid. Surface. A. 2010, 353, 166–171

[60] Huang, J.; Vongehr, S.; Tang, S.; Lu, H.; Shen, J.; Meng, X. Ag dendrite-based Au/Ag bimetallic nanostructures with strongly enhanced catalytic activity. Langmuir. 2009, 25 (19), 11890-11896.

[61] Jiang, Z.; Lin, Y.; Xie, Z. Structural investigations and growth mechanism of well-defined Ag dendrites prepared by conventional redox displacement. Mater. Chem. Phys. 2012, 134, 762-767.

[62] Kang, Y.; Chen, F. Preparation of Ag–Cu bimetallic dendritic nanostructures and their hydrogen peroxide electroreduction property. J. Appl. Electrochem. 2013, 43, 667–677.

[63] Song, W.; Cheng, Y.; Jia, H.; Xu, W.; Zhao, B. Surface enhanced Raman scattering based on silver dendrites substrate. J. Colloid Interf. Sci. 2006, 298, 765–768.

[64] Sulka, G. D.; Jaskuła, M. Temperature influence on the morphology and roughness of silver deposit formed by cementation. Helv. Chim. Acta. 2006, 89, 427-441.

[65] Yi, Z.; Chen, S.; Chen, Y.; Luo, J.; Wu, W.; Yi, Y.; Tang, Y. Preparation of dendritic Ag/Au bimetallic nanostructures and their application in surface-enhanced Raman scattering. Thin Solid Films. 2012, 520, 2701-2707.

[66] Bahadori, S. R., Mei, L., Athavale, A., Chiu, Y., Pickering, C. S., & Hao, Y. (2020). New Insight into Single-Crystal Silver Dendrite Formation and Growth Mechanisms. *Crystal Growth & Design*. https://doi.org/10.1021/acs.cgd.0c00953

[67] M. Fleischman, P. J. Hendra, A. J. McQuillian: Chem. Phys. Lett. 26, 123 (1974)

[68] D. L. Jeanmaire, R. P. Van Duyne: J Electroanal. Chem 84. 1 (1977)

[69] M.G .Albrecht, J. A. Creighton: J. Am. Chem. Soc. 99, 5215 (1977)

[70] M Moskovits: J. Chem. Phys. 69, 4159 (1978)

[71] Kneipp, Katrin, Harald Kneipp, Irving Itzkan, Ramachandra R. Dasari, and Michael S. Feld. 1999. "Surface-Enhanced Non-Linear Raman Scattering at the Single-Molecule Level." Chemical Physics 247(1):155–62.

[72] Kneipp K, Kneipp H, Manoharan R, et al. Extremely Large Enhancement Factors in Surface-Enhanced Raman Scattering for Molecules on Colloidal Gold Clusters. *Applied Spectroscopy*. 1998;52(12):1493-1497. doi:10.1366/0003702981943059

[73] Kneipp, Katrin, Yang Wang, Harald Kneipp, Lev T. Perelman, Irving Itzkan, Ramachandra R. Dasari, and Michael S. Feld. 1997. "Single Molecule Detection Using Surface-Enhanced Raman Scattering (SERS)." *Physical Review Letters* 78(9):1667–70.

[74] Kneipp, Katrin, Harald Kneipp, V. Bhaskaran Kartha, Ramasamy Manoharan, Geurt Deinum, Irving Itzkan, Ramachandra R. Dasari, and Michael S. Feld. 1998. "Detection and Identification of a Single DNA Base Molecule Using Surface-Enhanced Raman Scattering (SERS)." *Physical Review E* 57(6):R6281–84.

[75] Kneipp, Katrin, Yang Wang, Harald Kneipp, Irving Itzkan, Ramachandra R. Dasari, and Michael S. Feld. 1996. "Population Pumping of Excited Vibrational States by Spontaneous Surface-Enhanced Raman Scattering." *Physical Review Letters* 76(14):2444–47.

[76] Kneipp, K., Kneipp, H., Manoharan, R., Itzkan, I., Dasari, R.R. and Feld, M.S. (1998), Near-infrared surface-enhanced Raman scattering can detect single molecules and observe 'hot' vibrational transitions. J. Raman Spectrosc., 29: 743-747. https://doi.org/10.1002/(SICI)1097-4555(199808)29:8<743::AID-JRS294>3.0.CO;2-M

[77] Krug, John T., Geoffrey D. Wang, Steven R. Emory, and Shuming Nie. 1999. “Efficient Raman Enhancement and Intermittent Light Emission Observed in Single Gold Nanocrystals.” *Journal of the American Chemical Society* 121(39):9208–14.

[78] Emory, Steven R., William E. Haskins, and Shuming Nie. 1998. “Direct Observation of Size-Dependent Optical Enhancement in Single Metal Nanoparticles.” *Journal of the American Chemical Society* 120(31):8009–10.

[79] Lyon, William A. and Shuming Nie. 1997. “Confinement and Detection of Single Molecules in Submicrometer Channels.” *Analytical Chemistry* 69(16):3400–3405.

[80] Maxwell, Dustin J., Steven R. Emory, and Shuming Nie. 2001. “Nanostructured Thin-Film Materials with Surface-Enhanced Optical Properties.” Chemistry of Materials 13(3):1082–88.

[81] Yang, Wen-Hui, George C. Schatz, and Richard P. Van Duyne. 1995. “Discrete Dipole Approximation for Calculating Extinction and Raman Intensities for Small Particles with Arbitrary Shapes.” The Journal of Chemical Physics 103(3):869–75.

[82] Yin, L., V. K. Vlasko-Vlasov, A. Rydh, J. Pearson, U. Welp, S. H. Chang, S. K. Gray, G. C. Schatz, D. B. Brown, and C. W. Kimball. 2004. “Surface Plasmons at Single Nanoholes in Au Films.” *Applied Physics Letters* 85(3):467–69.

[83] Le Ru, E.C.; Etchegoin, P.G. Principles of Surface Enhanced Raman Spectroscopy; Elsevier: Amsterdam, The Netherlands, 2009.

[84] Qian, X. M. and S. M. Nie. 2008. “Single-Molecule and Single-Nanoparticle SERS: From Fundamental Mechanisms to Biomedical Applications.” Chemical Society Reviews 37(5):912–20.

[85] Guerrini, Luca and Duncan Graham. 2012. “Molecularly-Mediated Assemblies of Plasmonic Nanoparticles for Surface-Enhanced Raman Spectroscopy Applications.” Chemical Society Reviews 41(21):7085–7107.

[86] Micic, Miodrag, Nicholas Klymyshyn, Yung Doug Suh, and H. Peter Lu. 2003. “Finite Element Method Simulation of the Field Distribution for AFM Tip-Enhanced Surface-Enhanced Raman Scanning Microscopy.” The Journal of Physical Chemistry B 107(7):1574–84.

[87] Micic, Miodrag, Nicholas Klymyshyn, Yung Doug Suh, and H. Peter Lu. 2003. “Finite Element Method Simulation of the Field Distribution for AFM Tip-Enhanced Surface-Enhanced Raman Scanning Microscopy.” The Journal of Physical Chemistry B 107(7):1574–84.

[88] Mahmoud, M. A. and M. A. El-Sayed. 2009. “Aggregation of Gold Nanoframes Reduces, Rather Than Enhances, SERS Efficiency Due to the Trade-Off of the Inter- and Intraparticle Plasmonic Fields.” Nano Letters 9(8):3025–31.

[89] Kane Yee, "Numerical solution of initial boundary value problems involving maxwell's equations in isotropic media," in IEEE Transactions on Antennas and Propagation, vol. 14, no. 3, pp. 302-307, May 1966, doi: 10.1109/TAP.1966.1138693.

[90] Hsu, Chiajen, Chienwen Huang, Yaowu Hao, and Fuqiang Liu. 2012. “Au/Pd Core–Shell Nanoparticles for Enhanced Electrocatalytic Activity and Durability.” Electrochemistry Communications 23:133–36.

[91] Enhanced Raman spectroscopy: Principles,Substrates,and Applications.In Metal Nanoparticles and Clusters: Advances in Synthesis,Properties and Applications; Deepak,F.L., Ed.; Springer: Cham,Switzerland,2018; pp.89–164

[92] Gu, C., & Zhang, T. Y. (2008). Electrochemical synthesis of silver polyhedrons and dendritic films with superhydrophobic surfaces. *Langmuir*, *24*(20), 12010-12016.

[93] Qin, X., Miao, Z., Fang, Y., Zhang, D., Ma, J., Zhang, L., ... & Shao, X. (2012). Preparation of dendritic nanostructures of silver and their characterization for electroreduction. *Langmuir*, *28*(11), 5218-5226.

[94] Mandke, M. V., Han, S. H., & Pathan, H. M. (2012). Growth of silver dendritic nanostructures via electrochemical route. *CrystEngComm*, *14*(1), 86-89.

[95] Sivasubramanian, R., & Sangaranarayanan, M. V. (2015). A facile formation of silver dendrites on indium tin oxide surfaces using electrodeposition and amperometric sensing of hydrazine. *Sensors and Actuators B: Chemical*, *213*, 92-101.

[96] Sharma, D. K., Ott, A., O'Mullane, A. P., & Bhargava, S. K. (2011). The facile formation of silver dendritic structures in the absence of surfactants and their electrochemical and SERS properties. *Colloids and Surfaces A: Physicochemical and Engineering Aspects*, *386*(1-3), 98-106.

[97] Chu, J., Zhao, Y., Li, S. H., Li, W. W., Chen, X. Y., Huang, Y. X., ... & Liu, G. (2015). A highly-ordered and uniform sunflower-like dendritic silver nanocomplex array as reproducible SERS substrate. *Rsc Advances*, *5*(5), 3860-3867.

[98] Bian, J., Shu, S., Li, J., Huang, C., Li, Y. Y., & Zhang, R. Q. (2015). Reproducible and recyclable SERS substrates: Flower-like Ag structures with concave surfaces formed by electrodeposition. *Applied Surface Science*, *333*, 126-133.

[99] Sawangphruk, M., Sanguansak, Y., Krittayavathananon, A., Luanwuthi, S., Srimuk, P., Nilmoung, S., ... & Limtrakul, J. (2014). Silver nanodendrite modified graphene rotating disk electrode for nonenzymatic hydrogen peroxide detection. *Carbon*, *70*, 287-294.

[100] Fu, L., Lai, G., Mahon, P. J., Wang, J., Zhu, D., Jia, B., ... & Yu, A. (2014). Carbon nanotube and graphene oxide directed electrochemical synthesis of silver dendrites. *Rsc Advances*, *4*(75), 39645-39650.

[101] Yang, Z., Tjiu, W. W., Fan, W., & Liu, T. (2013). Electrodepositing Ag nanodendrites on layered double hydroxides modified glassy carbon electrode: Novel hierarchical structure for hydrogen peroxide detection. *Electrochimica Acta*, *90*, 400-407.

[102] Hu, J., Sun, J., Bian, C., Tong, J., & Shanhong, X. (2013). 3D Dendritic Nanostructure of Silver-Array: Preparation, Growth Mechanism and Application in Nitrate Sensor. *Electroanalysis*, *25*(2), 546-556.

[103] Guadagnini, L., Ballarin, B., & Tonelli, D. (2013). Dendritic silver nanostructures obtained via one-step electrosynthesis: effect of nonanesulfonic acid and polyvinylpyrrolidone as additives on the analytical performance for hydrogen peroxide sensing. *Journal of nanoparticle research*, *15*(10), 1971.

[104] Bian, J. C., Chen, Z. D., Li, Z., Yang, F., He, H. Y., Wang, J., ... & Han, G. R. (2012). Electrodeposition of hierarchical Ag nanostructures on ITO glass for reproducible and sensitive SERS application. *Applied Surface Science*, *258*(17), 6632-6636.

[105] Bian, J., Li, Z., Chen, Z., Zhang, X., Li, Q., Jiang, S., ... & Han, G. (2012). Double- potentiostatic electrodeposition of Ag nanoflowers on ITO glass for reproducible surface-enhanced (resonance) Raman scattering application. *Electrochimica Acta*, *67*, 12-17.

[106] Qin, X., Wang, H., Wang, X., Miao, Z., Fang, Y., Chen, Q., & Shao, X. (2011). Synthesis of dendritic silver nanostructures and their application in hydrogen peroxide electroreduction. *Electrochimica Acta*, *56*(9), 3170-3174.

[107] Rezaei, B., & Damiri, S. (2010). Electrodeposited silver nanodendrites electrode with strongly enhanced electrocatalytic activity. *Talanta*, *83*(1), 197-204.

[108] Zhang, J., Day, C. S., & Carroll, D. L. (2009). Controlled growth of novel hyper- branched nanostructures in nanoporous alumina membrane. *Chemical Communications*, (45), 6937-6939.

[109] Jiang, Z., Lin, Y., & Xie, Z. (2012). Structural investigations and growth mechanism of well-defined Ag dendrites prepared by conventional redox displacement. *Materials Chemistry and Physics*, *134*(2-3), 762-767.

[110] Ding, H. P., Xin, G. Q., Chen, K. C., Zhang, M., Liu, Q., Hao, J., & Liu, H. G. (2010). Silver dendritic nanostructures formed at the solid/liquid interface via electroless deposition.*Colloids and Surfaces A: Physicochemical and Engineering Aspects*, *353*(2-3), 166-171.

[111] Fang, J., You, H., Kong, P., Yi, Y., Song, X., & Ding, B. (2007). Dendritic silver nanostructure growth and evolution in replacement reaction.*Crystal growth & design*, *7*(5), 864-867.

[112] Feng, C., Zhao, Y., & Jiang, Y. (2015). Silver nano-dendritic crystal film: a rapid dehydration SERS substrate of totally new concept. *Rsc Advances*, *5*(6), 4578-4585.

[113] Gu, H. X., Xue, L., Zhang, Y. F., Li, D. W., & Long, Y. T. (2015). Facile fabrication of a silver dendrite-integrated chip for surface-enhanced Raman scattering. *ACS applied materials & interfaces*, *7*(4), 2931-2936.

[114] Zhang, Y., Sun, S., Zhang, X., Tang, L., Song, X., & Yang, Z. (2014). Sulfate-ion- assisted galvanic replacement tuning of silver dendrites to highly branched chains for effective SERS. *Physical Chemistry Chemical Physics*, *16*(35), 18918-18925.

[115] Zhang, Y., Sun, S., Zhang, X., Tang, L., Song, X., Ding, B., & Yang, Z. (2014). Magnetic field controlled particle-mediated growth inducing icker-like silver architectures. *Chemical Engineering Journal*, *240*, 494-502.

[116] Zhao, H., Wang, F., Ning, Y., Zhao, B., Yin, F., Lai, Y., ... & Zhang, D. (2013). Green "planting" nanostructured single crystal silver. *Scientific reports*, *3*, 1511.

[117] Wang, F., Lai, Y., Zhao, B., Hu, X., Zhang, D., & Hu, K. (2010). Tunable growth of nanodendritic silver by galvanic-cell mechanism on formed activated carbon. *Chemical Communications*, *46*(21), 3782-3784.

[118] Xu, J., Zhang, W., & Yang, Z. (2013). An optical humidity sensor based on Ag nanodendrites. *Applied Surface Science*, *280*, 920-925.

[119] Avizienis, A. V., Martin-Olmos, C., Sillin, H. O., Aono, M., Gimzewski, J. K., & Stieg, A. Z. (2013). Morphological transitions from dendrites to nanowires in the electroless deposition of silver. *Crystal Growth & Design*, *13*(2), 465-469.

[120] Cheng, W. M., Wang, C. C., & Chen, C. Y. (2012). The influence of Ni nanoparticles and Ni (II) on the growth of Ag dendrites immobilized on the chelating copolymer membrane. *Materials Chemistry and Physics*, *137*(1), 76-84.

[121] Liu, R., Li, S., Yu, X., Zhang, G., Ma, Y., Yao, J., ... & Nadjo, L. (2011). Polyoxometalate-assisted galvanic replacement synthesis of silver hierarchical dendritic structures. *Crystal Growth & Design*, *11*(8), 3424-3431.

[122] Hsiao, W. H., Chen, H. Y., Yang, Y. C., Chen, Y. L., Lee, C. Y., & Chiu, H. T. (2011). Surface-enhanced Raman scattering imaging of a single molecule on urchin-like silver nanowires. *ACS applied materials & interfaces*, *3*(9), 3280-3284.

[123] Yang, Y., & Meng, G. (2010). Ag dendritic nanostructures for rapid detection of polychlorinated biphenyls based on surface-enhanced Raman scattering effect. *Journal of Applied Physics*, *107*(4), 044315.

[124] Cheng, W. M., Wang, C. C., & Chen, C. Y. (2010). Preparing chelated copolymer membrane for fabrication of Ag dendrites.*Journal of colloid and interface science*, *348*(1), 49-56.

[125] Ye, W., Shen, C., Tian, J., Wang, C., Hui, C., & Gao, H. (2009). Controllable growth of silver nanostructures by a simple replacement reaction and their SERS studies. *Solid State Sciences*, *11*(6), 1088-1093.

[126] Ren, W., Guo, S., Dong, S., & Wang, E. (2011). A simple route for the synthesis of morphology-controlled and SERS-active Ag dendrites with near-infrared absorption. *The Journal of Physical Chemistry C*, *115*(21), 10315-10320.

[127] Wang, L., Li, H., Tian, J., & Sun, X. (2010). Monodisperse, micrometer-scale, highly crystalline, nanotextured Ag dendrites: rapid, large-scale, wet-chemical synthesis and their application as SERS substrates. *ACS applied materials & interfaces*, *2*(11), 2987- 2991.

[128] Song, J., Hou, J., Tian, L., Guan, Y., Zhang, Y., & Zhu, X. X. (2015). Growth of giant silver dendrites on layer-by-layer assembled films. *Polymer*, *63*, 237-243.

[129] Wang, Y., Camargo, P. H., Skrabalak, S. E., Gu, H., & Xia, Y. (2008). A facile, water- based synthesis of highly branched nanostructures of silver. *Langmuir*, *24*(20), 12042- 12046.

[130] Sun, X., & Hagner, M. (2007). Novel preparation of snowflake-like dendritic nanostructures of Ag or Au at room temperature via a wet-chemical route. *Langmuir*, *23*(18), 9147-9150.

[131] Forati-Nezhad, M., Sadeghi, G. M. M., Yaghmaie, F., & Alimohammadi, F. (2015). Affecting the morphology of silver deposition on carbon nanotube surface: From nanoparticles to dendritic (tree-like) nanostructures.*Materials Science and Engineering: C*, *46*, 232-238.

[132] Chen, Y. N., & Wang, H. (2015). Jellyfish mesoglea as a matrix for the synthesis of extremely high content silver dendrites. *Journal of colloid and interface science*, *454*, 14-19.

[133] Yang, J., Cao, B., Li, H., & Liu, B. (2014). Investigation of the catalysis and SERS properties of flower-like and hierarchical silver microcrystals. *Journal of nanoparticle research*, *16*(10), 2651.

[134] Sivakov, V., Kaniukov, E. Y., Petrov, A. V., Korolik, O. V., Mazanik, A. V., Bochmann, A., ... & Toimil-Molares, M. E. (2014). Silver nanostructures formation in porous Si/SiO2 matrix. *Journal of crystal growth*, *400*, 21-26.

[135] Ng, C. H. B., & Fan, W. Y. (2014). Preparation of Ag stellar dendrites: modeling the growth of stellar snowflakes. *Crystal Growth & Design*, *14*(11), 6067-6072.

[136] Alam, M. M., Ji, W., Luitel, H. N., Ozaki, Y., Watari, T., & Nakashima, K. (2014). Template free synthesis of dendritic silver nanostructures and their application in surface-enhanced Raman scattering. *Rsc Advances*, *4*(95), 52686-52689.

[137] Wei, Y., Chen, Y., Ye, L., & Chang, P. (2011). Preparation of dendritic-like Ag crystals using monocrystalline silicon as template. *Materials Research Bulletin*, *46*(6), 929-936.

[138] Keita, B., Brudna Holzle, L. R., Ngo Biboum, R., Nadjo, L., Mbomekalle, I. M., Franger, S., ... & Ekedi, G. A. (2011). Green wet chemical route for the synthesis of silver and palladium dendrites. *European Journal of Inorganic Chemistry*, *2011*(8), 1201-1204.

[139] Mdluli, P. S., & Revaprasadu, N. (2009). Time dependant evolution of silver nanodendrites. *Materials Letters*, *63*(3-4), 447-450.

[140] Laurier, K. G., Poets, M., Vermoortele, F., De Cremer, G., Martens, J. A., Uji-i, H., ... & Roeffaers, M. B. (2012). Photocatalytic growth of dendritic silver nanostructures as SERS substrates. *Chemical communications*, *48*(10), 1559-1561.

[141] Ahmed, I., Wang, X., Boualili, N., Xu, H., Farha, R., Goldmann, M., & Ruhlmann, L. (2012). Photocatalytic synthesis of silver dendrites using electrostatic hybrid films of porphyrin–polyoxometalate. *Applied Catalysis A: General*, *447*, 89-99.

[142] Wang, X., & Liu, X. (2011). Self-assembled synthesis of Ag nanodendrites and their applications to SERS. *Journal of Molecular Structure*, *997*(1-3), 64-69.

[143] Qiao, Y., Lin, Y., Wang, Y., Li, Z., & Huang, J. (2011). Metal-driven viscoelastic wormlike micelle in anionic/zwitterionic surfactant systems and template-directed synthesis of dendritic silver nanostructures. *Langmuir*, *27*(5), 1718-1723.

[144] Yang, C., Xie, Y. T., Yuen, M. M., Xiong, X., & Wong, C. P. (2010). A facile chemical approach for preparing a SERS active silver substrate. *Physical Chemistry Chemical Physics*, *12*(43), 14459-14461.

[145] Tang, S., Meng, X., Lu, H., & Zhu, S. (2009). PVP-assisted sonoelectrochemical growth of silver nanostructures with various shapes. *Materials Chemistry and Physics*, *116*(2-3), 464-468.

[146] Tang, S., Vongehr, S., & Meng, X. (2009). Two distinct branch–stem interfacial structures of silver dendrites with vertical and slanted branchings. *Chemical Physics Letters*, *477*(1-3), 179-183.

[147] Zhu, J., Liu, S., Palchik, O., Koltypin, Y., & Gedanken, A. (2000). Shape-controlled synthesis of silver nanoparticles by pulse sonoelectrochemical methods. *Langmuir*, *16*(16), 6396-6399.

[148] K. Kneipp, M. Moskovits and H. Kneipp, Surface-enhanced Raman Scattering-Physics and Applications, Top. Appl. Phys., 2006, 103

[149] Zhou, Y., Yu, S. H., Wang, C. Y., Li, X. G., Zhu, Y. R., & Chen, Z. Y. (1999). A Novel ultraviolet irradiation photoreduction technique for the preparation of single-crystal Ag nanorods and Ag dendrites. *Advanced Materials*, *11*(10), 850-852.

[150] Moeendarbari, S.; Mulgaonkar, A.; Hande, A. S.; Silvers, W.; Zhang, C.; Liu, Y.; Pillai, A. K.; Sun, X.; Hao, Y. Gold Nanoparticles in Current Biomedical Applications. Rev. Nanosci. Nanotechnol. 2016, 5, 28−78.

[151] Cai, W.; Tang, X.; Yang, L.; Wang, X. Facile fabrication of leafy spikes-like silver dendrite crystals for SERS substrate. Mater. Res. Bull. 2013, 48, 4125−4133. Xie, S.; Zhang, X.; Xiao, D.; Paau, M. C.; Huang, J.; Choi, M. M. Fast growth synthesis of silver dendrite crystals assisted by sulfate ion and its application for surface-enhanced Raman scattering. J. Phys. Chem. C 2011, 115, 9943−9951.

[152] Xie, S.; Zhang, X.; Xiao, D.; Paau, M. C.; Huang, J.; Choi, M. M. Fast growth synthesis of silver dendrite crystals assisted by sulfate ion and its application for surface-enhanced Raman scattering. J. Phys. Chem. C 2011, 115, 9943- 9951, DOI: 10.1021/jp201484r

[153] Cong, F.-Z.; Wei, H.; Tian, X.-R.; Xu, H.-X. A facile synthesis of branched silver nanowire structures and its applications in surface-enhanced Raman scattering. Front. Phys. 2012, 7, 521- 526, DOI: 10.1007/s11467-012-0255-y

[154] Chen, H.; Luo, J.; Zeng, T.; Jiang, L.; Sun, Y.; Jiao, Z.; Jin, Y.; Sun, X. Investigation of the synthesis, SERS performance and application in glucose sensing of hierarchical 3D silver nanostructures. New J. Chem. 2014, 38, 3907- 3916, DOI: 10.1039/C3NJ01603J

[155] Xia, Y.; Li, T.; Gao, C.; Ma, C.; Chen, J. Facile fabrication of hierarchically flowerlike Ag microstructure for SERS application. J. Mater. Sci. 2014, 49, 2781- 2786, DOI: 10.1007/s10853-013-7981-6

[156] Li, Y.; Driver, M.; Decker, E.; He, L. Lipid and lipid oxidation analysis using surface enhanced Raman spectroscopy (SERS) coupled with silver dendrites. Food Res. Int. 2014, 58, 1- 6, DOI: 10.1016/j.foodres.2014.01.056

[157] Xia, Y.; Wang, J. Hierarchical silver nanodendrites: One-step preparation and application for SERS. Mater. Chem. Phys. 2011, 125, 267- 270, DOI: 10.1016/j.matchemphys.2010.09.022

[158] Zhao, B.; Lu, Y.; Zhang, C.; Fu, Y.; Moeendarbari, S.; Shelke, S. R.; Liu, Y.; Hao, Y. Silver dendrites decorated filter membrane as highly sensitive and reproducible three dimensional surface enhanced Raman scattering substrates. Appl. Surf. Sci. 2016, 387, 431- 436, DOI: 10.1016/j.apsusc.2016.06.128

[159] Zhang, W.; Tan, F.; Wang, W.; Qiu, X.; Qiao, X.; Chen, J. Facile, template-free synthesis of silver nanodendrites with high catalytic activity for the reduction of p-nitrophenol. J. Hazard. Mater. 2012, 217, 36- 42, DOI: 10.1016/j.jhazmat.2012.01.056

[160] Gao, P.; Zhang, M.; Hou, H.; Xiao, Q. A simple template method for hierarchical dendrites of silver nanorods and their applications in catalysis. Mater. Res. Bull. 2008, 43, 531- 538, DOI: 10.1016/j.materresbull.2007.06.031

[161] Rashid, M. H.; Mandal, T. K. Synthesis and catalytic application of nanostructured silver dendrites. J. Phys. Chem. C 2007, 111, 16750- 16760, DOI: 10.1021/jp074963x

[162] Han, S. H.; Park, L. S.; Lee, J.-S. Hierarchically branched silver nanostructures (HBAgNSs) as surface plasmon regulating platforms for multiplexed colorimetric DNA detection. J. Mater. Chem. 2012, 22, 20223- 20231, DOI: 10.1039/c2jm33632d

[163] Fu, J.; Ye, W.; Wang, C. Facile synthesis of Ag dendrites on Al foil via galvanic replacement reaction with [Ag (NH3) 2] Cl for ultrasensitive SERS detecting of biomolecules. Mater. Chem. Phys. 2013, 141, 107- 113, DOI: 10.1016/j.matchemphys.2013.04.031

[164] Hu, Y.; Liu, S.; Huang, S.; Pan, W. Superhydrophobicity and surface enhanced Raman scattering activity of dendritic silver layers. Thin Solid Films 2010, 519, 1314- 1318, DOI: 10.1016/j.tsf.2010.09.033

[165] Gu, C.; Zhang, T.-Y. Electrochemical synthesis of silver polyhedrons and dendritic films with superhydrophobic surfaces. Langmuir 2008, 24, 12010- 12016, DOI: 10.1021/la802354n

[166] Qin, X.; Miao, Z.; Fang, Y.; Zhang, D.; Ma, J.; Zhang, L.; Chen, Q.; Shao, X. Preparation of dendritic nanostructures of silver and their characterization for electroreduction. Langmuir2012, 28, 5218- 5226, DOI: 10.1021/la300311v

[167] Mandke, M. V.; Han, S.-H.; Pathan, H. M. Growth of silver dendritic nanostructures via electrochemical route. CrystEngComm 2012, 14, 86- 89, DOI: 10.1039/C1CE05791J

[168] Sivasubramanian, R.; Sangaranarayanan, M. A facile formation of silver dendrites on indium tin oxide surfaces using electrodeposition and amperometric sensing of hydrazine. Sens. Actuators, B 2015, 213, 92- 101, DOI: 10.1016/j.snb.2015.02.065

[169] Sharma, D. K.; Ott, A.; O'Mullane, A. P.; Bhargava, S. K. The facile formation of silver dendritic structures in the absence of surfactants and their electrochemical and SERS properties. Colloids Surf., A 2011, 386, 98- 106, DOI: 10.1016/j.colsurfa.2011.07.001

[170] Chu, J.; Zhao, Y.; Li, S.-H.; Li, W.-W.; Chen, X.-Y.; Huang, Y.-X.; Chen, Y.-P.; Qu, W.-G.; Yu, H.-Q.; Xu, A.-W.A highly-ordered and uniform sunflower-like dendritic silver nanocomplex array as reproducible SERS substrate. RSC Adv. 2015, 5, 3860- 3867, DOI: 10.1039/C4RA11151F

[171] Bian, J.; Shu, S.; Li, J.; Huang, C.; Li, Y. Y.; Zhang, R.-Q. Reproducible and recyclable SERS substrates: Flower-like Ag structures with concave surfaces formed by electrodeposition. Appl. Surf. Sci. 2015, 333, 126- 133, DOI: 10.1016/j.apsusc.2015.02.007

[172] Sawangphruk, M.; Sanguansak, Y.; Krittayavathananon, A.; Luanwuthi, S.; Srimuk, P.; Nilmoung, S.; Maensiri, S.; Meevasana, W.; Limtrakul, J. Silver nanodendrite modified graphene rotating disk electrode for nonenzymatic hydrogen peroxide detection. Carbon 2014, 70, 287- 294, DOI: 10.1016/j.carbon.2014.01.010

[173] Fu, L.; Lai, G.; Mahon, P. J.; Wang, J.; Zhu, D.; Jia, B.; Malherbe, F.; Yu, A. Carbon nanotube and graphene oxide directed electrochemical synthesis of silver dendrites. RSC Adv. 2014, 4, 39645-39650, DOI: 10.1039/C4RA06156J

[174] Yang, Z.; Tjiu, W. W.; Fan, W.; Liu, T. Electrodepositing Ag nanodendrites on layered double hydroxides modified glassy carbon electrode: Novel hierarchical structure for hydrogen peroxide detection. Electrochim. Acta 2013, 90, 400- 407, DOI: 10.1016/j.electacta.2012.12.038

[175] Hu, J.; Sun, J.; Bian, C.; Tong, J.; Shanhong, X. 3D Dendritic Nanostructure of Silver-Array: Preparation, Growth Mechanism and Application in Nitrate Sensor. Electroanalysis 2013, 25, 546-556, DOI: 10.1002/elan.201200465

[176] Guadagnini, L.; Ballarin, B.; Tonelli, D. Dendritic silver nanostructures obtained via one-step electrosynthesis: effect of nonanesulfonic acid and polyvinylpyrrolidone as additives on the analytical performance for hydrogen peroxide sensing. J. Nanopart. Res. 2013, 15, 1971, DOI: 10.1007/s11051-013-1971-0

[177] Bian, J.-C.; Chen, Z.-D.; Li, Z.; Yang, F.; He, H.-Y.; Wang, J.; Tan, J. Z. Y.; Zeng, J.-L.; Peng, R.-Q.; Zhang, X.-W.Electrodeposition of hierarchical Ag nanostructures on ITO glass for reproducible and sensitive SERS application. Appl. Surf. Sci. 2012, 258, 6632- 6636, DOI: 10.1016/j.apsusc.2012.03.093

[178] Bian, J.; Li, Z.; Chen, Z.; Zhang, X.; Li, Q.; Jiang, S.; He, J.; Han, G. Double-potentiostatic electrodeposition of Ag nanoflowers on ITO glass for reproducible surface-enhanced (resonance) Raman scattering application. Electrochim. Acta 2012, 67, 12- 17, DOI: 10.1016/j.electacta.2012.01.073

[179] Qin, X.; Wang, H.; Wang, X.; Miao, Z.; Fang, Y.; Chen, Q.; Shao, X. Synthesis of dendritic silver nanostructures and their application in hydrogen peroxide electroreduction. Electrochim. Acta2011, 56, 3170- 3174, DOI: 10.1016/j.electacta.2011.01.058

[180] Rezaei, B.; Damiri, S. Electrodeposited silver nanodendrites electrode with strongly enhanced electrocatalytic activity. Talanta 2010, 83, 197- 204, DOI: 10.1016/j.talanta.2010.09.006

[181] Zhang, J.; Day, C. S.; Carroll, D. L. Controlled growth of novel hyper-branched nanostructures in nanoporous alumina membrane. Chem. Commun. 2009, 6937- 6939, DOI: 10.1039/b913917f

[182] Jiang, Z.; Lin, Y.; Xie, Z. Structural investigations and growth mechanism of well-defined Ag dendrites prepared by conventional redox displacement. Mater. Chem. Phys. 2012, 134, 762- 767, DOI: 10.1016/j.matchemphys.2012.03.065

[183] Ding, H.-P.; Xin, G.-Q.; Chen, K.-C.; Zhang, M.; Liu, Q.; Hao, J.; Liu, H.-G. Silver dendritic nanostructures formed at the solid/liquid interface via electroless deposition. Colloids Surf., A2010, 353, 166- 171, DOI: 10.1016/j.colsurfa.2009.11.008

[184] Fang, J.; You, H.; Kong, P.; Yi, Y.; Song, X.; Ding, B. Dendritic silver nanostructure growth and evolution in replacement reaction. Cryst. Growth Des. 2007, 7, 864- 867, DOI: 10.1021/cg0604879

[185] Feng, C.; Zhao, Y.; Jiang, Y. Silver nano-dendritic crystal film: a rapid dehydration SERS substrate of totally new concept. RSC Adv. 2015, 5, 4578- 4585, DOI: 10.1039/C4RA11376D

[186] Gu, H.-X.; Xue, L.; Zhang, Y.-F.; Li, D.-W.; Long, Y.-T. Facile fabrication of a silver dendrite-integrated chip for surface-enhanced Raman scattering. ACS Appl. Mater. Interfaces 2015, 7, 2931-2936, DOI: 10.1021/am508403k

[187] Zhang, Y.; Sun, S.; Zhang, X.; Tang, L.; Song, X.; Yang, Z. Sulfate-ion-assisted galvanic replacement tuning of silver dendrites to highly branched chains for effective SERS. Phys. Chem. Chem. Phys. 2014, 16, 18918- 18925, DOI: 10.1039/C4CP02525C

[188] Zhang, Y.; Sun, S.; Zhang, X.; Tang, L.; Song, X.; Ding, B.; Yang, Z. Magnetic field controlled particle-mediated growth inducing icker-like silver architectures. Chem. Eng. J. 2014, 240, 494- 502, DOI: 10.1016/j.cej.2013.10.097

[189] Zhao, H.; Wang, F.; Ning, Y.; Zhao, B.; Yin, F.; Lai, Y.; Zheng, J.; Hu, X.; Fan, T.; Tang, J.Green "planting" nanostructured single crystal silver. Sci. Rep. 2013, 3, 1- 7, DOI: 10.1038/srep01511

[190] Wang, F.; Lai, Y.; Zhao, B.; Hu, X.; Zhang, D.; Hu, K. Tunable growth of nanodendritic silver by galvanic-cell mechanism on formed activated carbon. Chem. Commun. 2010, 46, 3782- 3784, DOI: 10.1039/c001517b

[191] Xu, J.; Zhang, W.; Yang, Z. An optical humidity sensor based on Ag nanodendrites. Appl. Surf. Sci. 2013, 280, 920- 925, DOI: 10.1016/j.apsusc.2013.05.097

[192] Avizienis, A. V.; Martin-Olmos, C.; Sillin, H. O.; Aono, M.; Gimzewski, J. K.; Stieg, A. Z.Morphological transitions from dendrites to nanowires in the electroless deposition of silver. Cryst. Growth Des. 2013, 13, 465- 469, DOI: 10.1021/cg301692n

[193] Cheng, W.-M.; Wang, C.-C.; Chen, C.-Y. The influence of Ni nanoparticles and Ni (II) on the growth of Ag dendrites immobilized on the chelating copolymer membrane. Mater. Chem. Phys. 2012, 137, 76- 84, DOI: 10.1016/j.matchemphys.2012.08.029

[194] Liu, R.; Li, S.; Yu, X.; Zhang, G.; Ma, Y.; Yao, J.; Keita, B.; Nadjo, L. Polyoxometalate-assisted galvanic replacement synthesis of silver hierarchical dendritic structures. Cryst. Growth Des.2011, 11, 3424-3431, DOI: 10.1021/cg2001333

[195] Hsiao, W.-H.; Chen, H.-Y.; Yang, Y.-C.; Chen, Y.-L.; Lee, C.-Y.; Chiu, H.-T. Surface-enhanced Raman scattering imaging of a single molecule on urchin-like silver nanowires. ACS Appl. Mater. Interfaces 2011, 3, 3280- 3284, DOI: 10.1021/am2007239

[196] Yang, Y.; Meng, G. Ag dendritic nanostructures for rapid detection of polychlorinated biphenyls based on surface-enhanced Raman scattering effect. J. Appl. Phys. 2010, 107, 044315, DOI: 10.1063/1.3298473

[197] Cheng, W.-M.; Wang, C.-C.; Chen, C.-Y. Preparing chelated copolymer membrane for fabrication of Ag dendrites. J. Colloid Interface Sci. 2010, 348, 49- 56, DOI: 10.1016/j.jcis.2010.04.040

[198] [Crossref], [PubMed], [CAS], Google Scholaropen URL

[199] Ye, W.; Shen, C.; Tian, J.; Wang, C.; Hui, C.; Gao, H. Controllable growth of silver nanostructures by a simple replacement reaction and their SERS studies. *Solid State Sci.* **2009**, *11*, 1088– 1093, DOI: 10.1016/j.solidstatesciences.2009.03.001

[200] Ren, W.; Guo, S.; Dong, S.; Wang, E. A simple route for the synthesis of morphology-controlled and SERS-active Ag dendrites with near-infrared absorption. *J. Phys. Chem. C* **2011**, *115*, 10315– 10320, DOI: 10.1021/jp110532c

[201] Wang, L.; Li, H.; Tian, J.; Sun, X. Monodisperse, micrometer-scale, highly crystalline, nanotextured Ag dendrites: rapid, large-scale, wet-chemical synthesis and their application as SERS substrates. *ACS Appl. Mater. Interfaces* **2010**, *2*, 2987– 2991, DOI: 10.1021/am100968j

[202] Song, J.; Hou, J.; Tian, L.; Guan, Y.; Zhang, Y.; Zhu, X. Growth of giant silver dendrites on layer-by-layer assembled films. *Polymer* **2015**, *63*, 237– 243, DOI: 10.1016/j.polymer.2015.03.009

[203] Wang, Y.; Camargo, P. H.; Skrabalak, S. E.; Gu, H.; Xia, Y. A facile, water-based synthesis of highly branched nanostructures of silver. *Langmuir* **2008**, *24*, 12042– 12046, DOI: 10.1021/la8020904

[204] Sun, X.; Hagner, M. Novel preparation of snowflake-like dendritic nanostructures of Ag or Au at room temperature via a wet-chemical route. *Langmuir* **2007**, *23*, 9147– 9150, DOI: 10.1021/la701519x

[205] Forati-Nezhad, M.; Mir Mohamad Sadeghi, G.; Yaghmaie, F.; Alimohammadi, F. Affecting the morphology of silver deposition on carbon nanotube surface: From nanoparticles to dendritic (tree-like) nanostructures. *Mater. Sci. Eng., C* **2015**, *46*, 232– 238, DOI: 10.1016/j.msec.2014.10.039

[206] Chen, Y.-N.; Wang, H. Jellyfish mesoglea as a matrix for the synthesis of extremely high content silver dendrites. *J. Colloid Interface Sci.* **2015**, *454*, 14– 19, DOI: 10.1016/j.jcis.2015.04.052

[207] Yang, J.; Cao, B.; Li, H.; Liu, B. Investigation of the catalysis and SERS properties of flower-like and hierarchical silver microcrystals. *J. Nanopart. Res.* **2014**, *16*, 2651, DOI: 10.1007/s11051-014-2651-4

[208] Sivakov, V.; Kaniukov, E. Y.; Petrov, A. V.; Korolik, O. V.; Mazanik, A. V.; Bochmann, A.; Teichert, S.; Hidi, I. J.; Schleusener, A.; Cialla, D.Silver nanostructures formation in porous Si/SiO2 matrix. *J. Cryst. Growth* **2014**, *400*, 21– 26, DOI: 10.1016/j.jcrysgro.2014.04.024

[209] Ng, C. H. B.; Fan, W. Y. Preparation of Ag stellar dendrites: modeling the growth of stellar snowflakes. *Cryst. Growth Des.* **2014**, *14*, 6067– 6072, DOI: 10.1021/cg5012204

[210] Alam, M. M.; Ji, W.; Luitel, H. N.; Ozaki, Y.; Watari, T.; Nakashima, K. Template free synthesis of dendritic silver nanostructures and their application in surface-enhanced Raman scattering. *RSC Adv.* **2014**, *4*, 52686– 52689, DOI: 10.1039/C4RA10113H

[211] Wei, Y.; Chen, Y.; Ye, L.; Chang, P. Preparation of dendritic-like Ag crystals using monocrystalline silicon as template. *Mater. Res. Bull.* **2011**, *46*, 929– 936, DOI: 10.1016/j.materresbull.2011.02.025

[212] Keita, B.; Brudna Holzle, L.; Ngo Biboum, R.; Nadjo, L.; Mbomekalle, I. M.; Franger, S.; Berthet, P.; Brisset, F.; Miserque, F.; Ekedi, G. A. Green wet chemical route for the synthesis of silver and palladium dendrites. *Eur. J. Inorg. Chem.* **2011**, *2011*, 1201– 1204, DOI: 10.1002/ejic.201001259

[213] Mdluli, P.; Revaprasadu, N. Time dependant evolution of silver nanodendrites. *Mater. Lett.***2009**, *63*, 447– 450, DOI: 10.1016/j.matlet.2008.11.024

[214] Laurier, K. G.; Poets, M.; Vermoortele, F.; De Cremer, G.; Martens, J. A.; Uji-I, H.; De Vos, D. E.; Hofkens, J.; Roeffaers, M. B. Photocatalytic growth of dendritic silver nanostructures as SERS substrates. *Chem. Commun.* **2012**, *48*, 1559– 1561, DOI: 10.1039/C1CC14727G

[215] Ahmed, I.; Wang, X.; Boualili, N.; Xu, H.; Farha, R.; Goldmann, M.; Ruhlmann, L.Photocatalytic synthesis of silver dendrites using electrostatic hybrid films of porphyrin–polyoxometalate. *Appl. Catal., A* **2012**, *447*, 89– 99, DOI: 10.1016/j.apcata.2012.09.022

[216] Tang, S.; Meng, X.; Lu, H.; Zhu, S. PVP-assisted sonoelectrochemical growth of silver nanostructures with various shapes. *Mater. Chem. Phys.* **2009**, *116*, 464– 468, DOI: 10.1016/j.matchemphys.2009.04.004

[217] Tang, S.; Vongehr, S.; Meng, X. Two distinct branch–stem interfacial structures of silver dendrites with vertical and slanted branchings. *Chem. Phys. Lett.* **2009**, *477*, 179– 183, DOI: 10.1016/j.cplett.2009.06.087

[218] Zhu, J.; Liu, S.; Palchik, O.; Koltypin, Y.; Gedanken, A. Shape-controlled synthesis of silver nanoparticles by pulse sonoelectrochemical methods. *Langmuir* **2000**, *16*, 6396– 6399, DOI: 10.1021/la991507u

[219] Zhou, Y.; Yu, S. H.; Wang, C. Y.; Li, X. G.; Zhu, Y. R.; Chen, Z. Y. A novel ultraviolet irradiation photoreduction technique for the preparation of single-crystal Ag nanorods and Ag dendrites. *Adv. Mater.* **1999**, *11*, 850– 852, DOI: 10.1002/(SICI)1521-4095(199907)11:10<850::AID-ADMA850>3.0.CO;2-Z

[220] Xu, H.; Shao, M.; Chen, T.; Zhao, Y.; Lee, S. T. Surface-enhanced Raman scattering on silver dendrite with different growth directions. *J. Raman Spectrosc.* **2012**, *43*, 396– 404, DOI: 10.1002/jrs.3042

[221] Zhang, G.; Sun, S.; Banis, M. N.; Li, R.; Cai, M.; Sun, X. Morphology-controlled green synthesis of single crystalline silver dendrites, dendritic flowers, and rods, and their growth mechanism. *Cryst. Growth Des.* **2011**, *11*, 2493– 2499, DOI: 10.1021/cg200256j

[222] Gutés, A.; Carraro, C.; Maboudian, R. Silver dendrites from galvanic displacement on commercial aluminum foil as an effective SERS substrate. *J. Am. Chem. Soc.* **2010**, *132*, 1476– 1477, DOI: 10.1021/ja909806t

[223] Lv, S.; Suo, H.; Zhou, T.; Wang, C.; Jing, S.; Fu, Q.; Xu, Y.; Zhao, C. Effect of synthesis route on the morphologies of silver nanostructures by galvanic displacement reaction. *Solid State Commun.* **2009**, *149*, 227– 230, DOI: 10.1016/j.ssc.2008.11.021

[224] Fang, J.; Ding, B.; Song, X.; Han, Y. How a silver dendritic mesocrystal converts to a single crystal. *Appl. Phys. Lett.* **2008**, *92*, 173120, DOI: 10.1063/1.2888770

[225] Giustarini, D.; Rossi, R.; Milzani, A.; Dalle-Donne, I. Nitrite and nitrate measurement by Griess reagent in human plasma: evaluation of interferences and standardization. *Methods Enzymol.* **2008**, *440*, 361– 380, DOI: 10.1016/S0076-6879(07)00823-3

[226] Han, Y.; Liu, S.; Han, M.; Bao, J.; Dai, Z. Fabrication of hierarchical nanostructure of silver via a surfactant-free mixed solvents route. *Cryst. Growth Des.* **2009**, *9*, 3941– 3947, DOI: 10.1021/cg900066z

[227] Penn, R. L.; Banfield, J. F. Imperfect oriented attachment: dislocation generation in defect-free nanocrystals. *Science* **1998**, *281*, 969– 971, DOI: 10.1126/science.281.5379.969

[228] Washio, I.; Xiong, Y.; Yin, Y.; Xia, Y. Reduction by the end groups of poly (vinyl pyrrolidone): a new and versatile route to the kinetically controlled synthesis of Ag triangular nanoplates. *Adv. Mater.* **2006**, *18*, 1745– 1749, DOI: 10.1002/adma.200600675

[229] Walton, K., R. Walker, J. J. M. van de Sandt, J. V Castell, A. G. A. .. Knapp, G. Kozianowski, M. Roberfroid, and B. Schilter. 1999. "The Application of in Vitro Data in the Derivation of the Acceptable Daily Intake of Food Additives." Food and Chemical Toxicology 37(12):1175–97.

[230] Mohammadi Nilash, M, Mirzaei, F, Fakhari, AR. Development and application of SBA-15 assisted electromembrane extraction followed by corona discharge ion mobility spectrometry for the determination of Thiabendazole in fruit juice samples. J Sep Sci 2019; 42: 1786– 1793. https://doi.org/10.1002/jssc.201800676

[231] U.S. Environmental Protection agency, No Title, 2002.